Mapping of Ice Sheet Deep Layers and Fast Outlet Glaciers with Multi-Channel-High-Sensitivity Radar

by

Jilu Li

Submitted to the graduate degree program in Electrical Engineering and Computer Science and the Graduate Faculty of the University of Kansas School of Engineering in partial fulfillment of the requirements for the degree of Doctor of Philosophy

Dissertation Committee:

_____
Chairperson: Sivaprasad Gogineni

_____
Carl Leuschen

_____
Fernando Rodriguez-Morales

_____
Sarah Seguin

_____
David Braaten

Date of Defense: November 6, 2009

The Dissertation Committee for Jilu Li Certifies that this is the approved version of the following Dissertation:

Mapping of Ice Sheet Deep Layers and Fast Outlet Glaciers
with Multi-Channel-High-Sensitivity Radar

Dissertation Committee:

_____
Chairperson: Sivaprasad Gogineni

_____
Carl Leuschen

_____
Fernando Rodriguez-Morales

_____
Sarah Seguin

_____
David Braaten

Date approved: _____

Dedication

In memory of my father, 1929-2009

Acknowledgements

As always, my first debt is to my wife Suyun for her love and support during my long pursuit of a PhD degree in Electrical Engineering. I cannot imagine that I would have been able to finish the dissertation had she not been taking care of my sons. I am especially grateful for her support after I left KU for a job, which was when I had the hardest time writing the dissertation. I also owe a lot to my parents, as I only went back once to see them during the last nine years.

I would like to thank my advisor Dr. Gogineni for his invaluable guidance and support throughout my research. I would also like to thank him for the motivation he always gives me by iterating the important scientific and social value of CReSIS research. Dr. Gogineni's insights and expertise in ice radar technology provided the inspiration for many of the ideas from which I carried out my dissertation. At the start I did not know much about SAR, so he spent a lot time with me on details during the development and implementation of the SAR algorithm. I also thank him for the recommendation he granted for me to obtain the NASA fellowship and for the precious opportunity he provided for me to travel to Australia to attend the SCAR conference and sea ice workshop.

I take this opportunity to express my appreciation to Dr. Leuschen for the help he provided with his hands-on experience in processing radar data. I always

got the right answer when I brought questions to him. I would like to thank Dr. Braaten, Dr. Rodriguez-Morales, and Dr. Seguin for serving on my dissertation committee. I also would like to thank Dr. Allen and Dr. Prescott for once serving on the committee. I enjoyed their classes on radars and digital signal processing.

I am grateful to Ms. Jenna Collins for her careful proofreading. I acknowledge Dr. Laird, graduate students Anthony, William, Joel, Victor and Logan for our discussions together and their help. I will remember CReSIS in my life not only because it is a nice NSF Science and Technology Center but also because of the people there who are devoted to ice-sheet research.

Finally, I would like to thank Thorbjorn Axelsson, Dan Hellebust and Kyle Begole for their computer support in processing ice data in Terabytes and for their help with remote access to the CReSIS computation network.

Table of Contents

List of Figures

List of Tables

Abstract

The airborne multi-channel radar depth sounder systems (MCRDS) are developed at the Center for Remote Sensing of Ice Sheets (CReSIS) to map the ice-sheet bed, deep internal layers, and fast-flowing outlet glaciers with their high sensitivity for weak echoes and the beamforming ability of the receive antenna array for clutter reduction. The objective of mapping ice-sheet deep layers is to retrieve ice-flow history for ice-dynamics modeling and help glaciologists select optimum ice-core site for studies of the past climate. The objective of mapping fast-flowing outlet glaciers is to understand ice-sheet responses to current global warming and estimate ice-sheet contribution to sea level rise. The work of this dissertation is part of the efforts CReSIS put in to obtain the best results in processing the data MCRDS radars have collected in Greenland. This dissertation includes the waveforms design, the development and implementation of SAR processing, and clutter reduction algorithms for MCRDS radars.

To detect weak echoes of deep layers close to the ice bed, the sidelobes of the strong echoes of the ice-bed have to be suppressed to a required low level, as they might mask or be misinterpreted as those of the deep layers. Two kinds of low-sidelobe waveforms are simulated, designed, and tested in the laboratory and applied by MCRDS radars in field survey. The first kind is tapered linear-chirp and the second one is complementary-coded waveforms. The tapered waveforms are verified to have achieved a low sidelobe of -64 dB using real survey data in Greenland that

have high-SNR specular echoes from ocean surface, smooth ice surface and bed. On the other hand, the complementary-coded waveforms only suppress the sidelobes to -48 dB because of their higher sensitivity to system distortions.

Big ice attenuation is the greatest challenge in sounding fast outlet glaciers using airborne radars. Besides the elaborate hardware design, MCRDS radars maximize the sensitivity to overcome the signal loss by system calibration, channel mismatch compensation, RFI suppression and SAR (synthetic aperture radar) processing with aircraft motion compensations in data processing. In this dissertation, the SNR gains from the calibration of reference functions for pulse compression and the compensation of constant channel mismatches are verified with echoes from the ice bed. Some deep ice layers of the Greenland ice sheet that are masked by RFI (radio frequency interference) in MCRDS data are revealed by applying adaptive array processing. A SAR algorithm based on wavefront reconstruction theory is developed and implemented in frequency and wave-number domains with narrow beamwidth motion compensation. The SNR gains by SAR processing with motion compensation are carefully verified by using simulation data and sea-ice data. With the verified SAR processing algorithms, very weak echoes from the deepest parts of Jakobshavn channel are detected for the first time using large synthetic aperture length in radar soundings and the depths match with seismic measurements.

While SAR processing effectively reduces along-track clutter, across-track clutter is another challenge encountered in sounding fast-flowing outlet glaciers. MCRDS radars facilitate rejection of across-track surface clutter with small arrays of four, five or six elements. In this dissertation, three clutter-reduction algorithms are either developed or implemented: 1) the data-dependent FMV algorithm, 2) the data-independent null-steering algorithm, and 3) the clutter-power estimation algorithm. The first two algorithms reduce clutter signals by 34.30 dB and 28.57 dB respectively when applied to sea-ice data. But neither is very effective when applied to ice data with distributed clutter. The third algorithm developed is a beam-spaced method. It is more robust to channel the mismatches and clutter angle estimate errors that are the limiting factors of the first two methods. There are two stages of the beam-spaced method. The first stage is to form a main beam and a clutter beam. The main beam is formed by choosing weights to enhance the nadir signals and with clutter signals partly reduced. The clutter beam is formed by choosing weights to put a null at nadir and to have maximum gains in the direction of clutter. The second stage is to subtract the weighted clutter beam from the main beam to properly compensate the gain difference between the two beams based on power profiles estimation. Two clutter scenarios are used to illustrate the effectiveness of the beam-spaced algorithm. In the first scenario, the aircraft's altitude is high and the ice bed masked by clutter is deep, while in the second case the aircraft's altitude is low and the ice bed masked by clutter is shallow. In both scenarios the beam-spaced algorithm reduces clutter further beyond the reduction by Hanning weighting. The further clutter reduction is around

10.3 dB in the first case and 9.6 dB in the second one. This dissertation also presents the results of applying the beam-spaced method in two cases over Jakobshavn channel. In the first case, the across-track ice clutter is cleared but the channel ice bed is still invisible because of the huge ice attenuation in the channel. In the second case that needs to be further studied, the method fails to reduce the clutter-like signals near the channel's calving front.

Chapter 1: Introduction

1.1 Backgound

Climate change has a great impact on humans and is currently being addressed as a serious issue that humanity must face over this century. Atmosphere, oceans, and polar ice sheets and their outlet glaciers are important components that closely interact in the complex climate system. In the latest report of IPCC [1], it is stated that "Warming of the climate is unequivocal, as is now evident from observations of increases in global average air and ocean temperatures, widespread melting of snow and ice, and rising global average sea level." Recent satellite observations show that polar ice sheets are undergoing rapid changes. For example, a total area of about 3,250 km^2 of the Larsen B ice shelf in Antarctica disintegrated in a 35-day period beginning on 31 January 2002, as shown in Figure 1.1. The ice discharge from Greenland outlet glaciers has doubled in the last decade: 51±28Gt yr^{-1} in 1996, 83±27Gt yr^{-1} in 2000, and150±36Gt yr^{-1} in 2005 [2].

The mass loss of polar ice sheets contributes to sea level rise. Typically, a 50-centimeter sea level rise would cause a coastline retreat of 50 meters in flat coastal areas. Therefore, a direct and devastating consequence of sea level rise is the flooding of the coastal regions, which results in the migration of people from these regions and huge losses of land and property. Worldwide about 100 million people live within

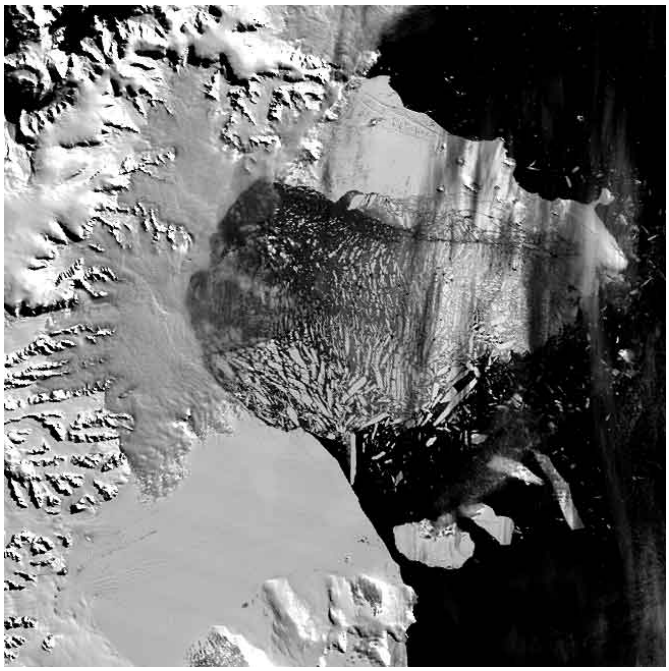

Figure 1.1: Collapse of Larsen B Ice Shelf in Antarctica
http://nsidc.org/iceshelves/larsenb2002/

*Table 1.1: Observed rate of sea level rise and estimated contributions from different sources

Source of sea level rise	Rate of sea level rise(mm per year)	
	1961-2003	1993-2003
Thermal expansion	0.42 ± 0.12	1.6 ± 0.5
Glaciers and ice caps	0.50 ± 0.18	0.77 ± 0.22
Greenland Ice Sheet	0.05 ± 0.12	0.21 ± 0.07
Antarctic Ice Sheet	0.14 ± 0.41	0.21 ± 0.35
Sum of individual climate contributions to sea level rise	1.1 ± 0.5	2.8 ± 0.7
Observed total sea level rise	1.8 ± 0.5	3.1 ± 0.7

* Alley and Berntsen etc. 2007

one meter of sea level. Table 1.1 is a summary of the observed rate of sea level rise and estimated contributions from different sources from 1961 to 2003 and 1993 to 2003. Although the contributions to present sea level rise from ice sheets are smaller

compared to thermal expansion, glaciers, and ice caps, their future potential contributions are very critical in a warming climate. This is because the Antarctic Ice Sheet holds a volume of water approximately equivalent to a global sea level rise of 65 meters, and the Greenland Ice Sheet holds a volume of water equivalent to a global sea level rise of about 7 meters.

Ice sheet contribution to sea level rise is determined by the ice sheet's mass balance, which is the net gain or loss of ice. There are three main approaches for measuring and estimating ice sheet mass balance: 1) the integrated approach, by measuring the ice sheet elevation change and equating this change to ice volume change; 2) the ice flux approach, by comparing the mass input of snow accumulation at the ice sheet top with the mass output from ice flow and melt water runoff at the ice sheet margin; and 3) Earth's gravity field approach, by correlating the satellite observation of the field changes to ice volume change [3]. The ice flux approach is straightforward and relates the ice thickness history to ice mass balance and flow by the continuity equation of mass conservation:

$$\frac{\partial H}{\partial t} = Q_a - Q_L - \nabla \cdot (H < \bar{u} >) \tag{1.1}$$

where H is the ice thickness, Q_a the net accumulation rate, Q_L the net mass loss rate and $\bar{u}$ is the depth-averaged flow velocity. Therefore, in order to accurately estimate ice sheet mass balance, geologists need to understand ice flow dynamics from which surface elevation and topography, ice thickness, basal conditions, inter-annual layers, and ice velocity are important parameters. Ice sheet deep layers reveal accumulation

and ice flow history. Basal conditions can be understood or inferred from the deformation of ice layers close to the bed. For instance, ice layers tend to conform to the bed topography if it is frozen and to dip down if there is melt at the bed. Present understanding and future prediction of ice flow dynamics require knowledge of past ice flow dynamics, since the response time of ice sheets is very slow. For example, the response time of the Greenland ice sheet is about 3000 years [4]. Ice core scientists are also very interested in deep layers, as they need to recover the climate history as far back as possible. Mapping of deep layers also helps glaciologists to select ice core sites and date ice layers [3]. Compared to slow-moving ice, the recently observed fast discharge from outlet glaciers of ice sheets is not well understood or modeled. Mapping of these fast outlet glaciers is required not only to estimate the ice sheet mass loss but also to understand and model their dynamics in response to climate change.

Radar remote sensing is an important technique in the study of large ice sheets. It has advantages in terms of cost and coverage compared to ice core and seismic methods. Space-borne radars have been very successful in mapping ice surface elevation and velocity with global coverage. On the other hand, airborne and ground-based radars are capable of measuring ice thickness, internal annual layers, and basal conditions over a smaller scale with good resolution. The University of Kansas and the Center for Remote Sensing of Ice Sheets have made contributions in polar ice measurement through many years of effort in developing ground-based and airborne

radar systems and in collecting and providing high quality data [6, 7, 8, 9 and 10]. Recent efforts at CReSIS include the development of a surface-based wideband bistatic synthetic aperture radar for mapping ice basal conditions [11,12] and multi-channel and dual band airborne systems with beam steering capability for mapping fast outlet glaciers [13,14].

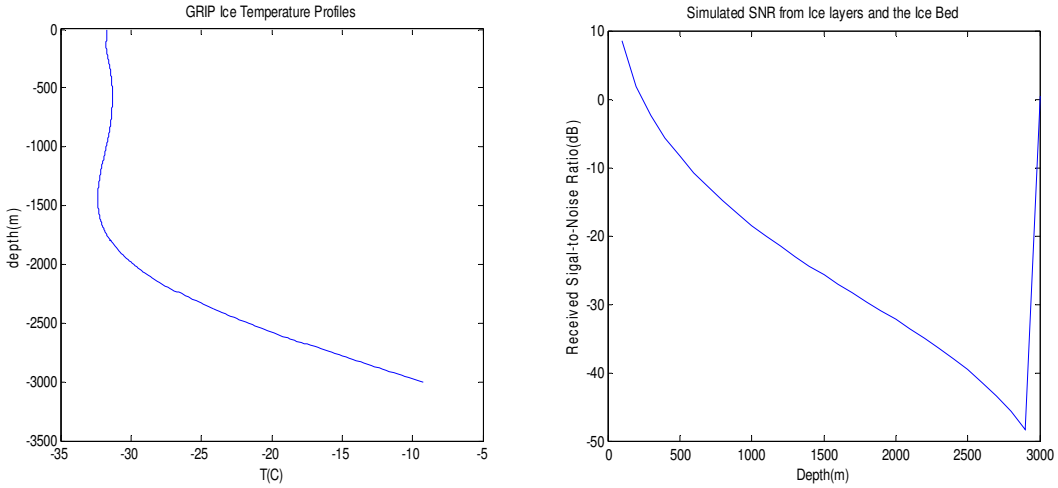

Figure 1.2: GRIP Ice Model (left) and Simulated SNR from Ice Layers and the Bed (right)

1.2 Objectives

Mapping the ice sheets' deep layers close to the bed and fast outlet glaciers presents significant challenges in radar remote sensing. The reflected signal from deep layers is usually very weak and may be masked by the sidelobes of much stronger ice bed echoes. As a result, most ice depth sounding fails to gather information about the deep layers close to the bed. In order to map internal ice layers near the ice bed, the sidelobes of the bed echoes have to be suppressed below the level of the echoes from

ice layers near the ice bed so that the deep ice layers would not be masked. Figure 1.2 presents the simulated results of signal-to-noise ratio as a function of ice depth using a GRIP ice model. According to the left chart, the signal level difference between the echoes from the ice bed and ice layers near it is around 50_dB. This means the sidelobes of the bed echoes have to be suppressed 60_dB lower, relative to the main lobes for reliable deep layer detection.

For fast-flowing outlet glaciers, the ice temperature is higher compared to inland ice, and radar signals experience higher loss in propagating through the warm ice. The surface of outlet glaciers is usually heavily crevassed, as shown in the picture in Figure 1.3. Strong surface clutter from a rough surface will mask weak reflected signals from the layers and the ice bed. Figure 1.4 is a real radar image we obtained in 2006 over the Jakobshavn calving front in which the clutter masks the bottom. Therefore, clutter is another problem that has to be reduced for an airborne system. In order to address the above-mentioned challenges, a specially designed and configured radar system with high sensitivity, waveform coding, and shaping and beam steering capability has to be used together with corresponding data processing algorithms. High sensitivity is required for detecting weak reflected signals, waveform coding and shaping techniques are used to reduce sidelobes, and beam steering capability is for surface clutter cancellation. The detailed approaches are explored and described in this dissertation.

Figure 1.3: Crevassed Surface of Jakobshavn (www.sethwhite.org/.../jakobshavn%20glacier.jpg)

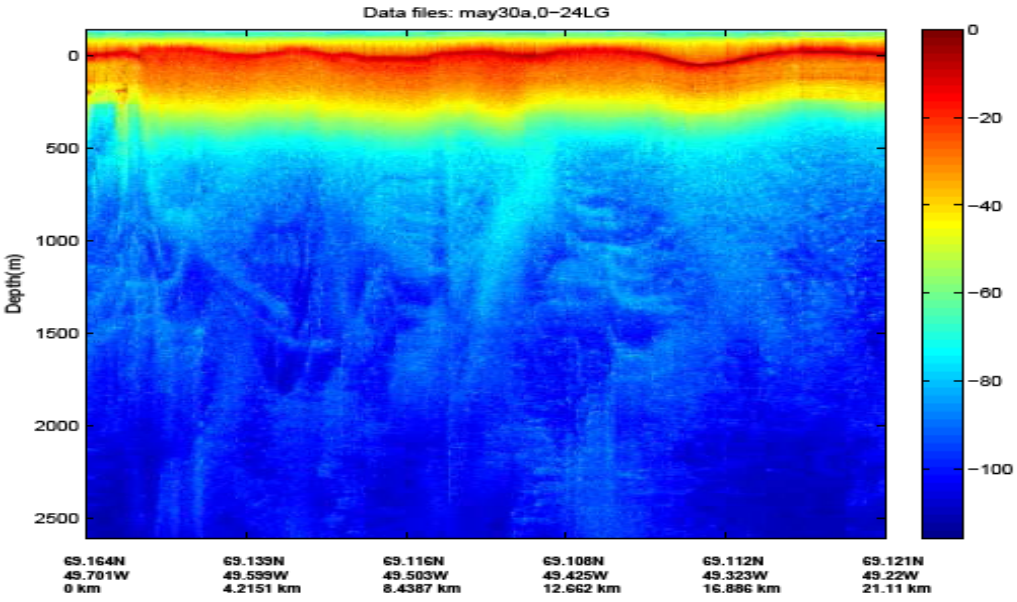

Figure 1.4: Radar Image over Jakobshavn Calving Front

1.3 Dissertation Organization

There are seven chapters in this dissertation. Chapter 1 reviews the research background and objectives. Chapter 2 describes the airborne radar systems used to collect data in 2006 and 2007 over Greenland ice sheet. Chapter 3 discusses the design of tapered linear chirp waveform and binary complementary-coded waveform to reduce sidelobes of pulse compression and presents data processing results to show the low sidelobe levels achieved. Chapter 4 explains the data preconditioning steps including reference function calibration, channel equalization, and radio frequency interference (RFI) reduction. These steps are essential to obtain the best outcomes from the data processing procedures of pulse compression, synthetic aperture radar (SAR) processing, and array processing. Chapter 5 describes in detail the wavefront reconstruction theory and the implementation and verification of SAR processing algorithm with motion compensation. This chapter also presents the data processing results with very weak bottom echoes along and across Jakobshavn channel. Chapter 6 briefly reviews linear array and beamforming theories, discusses three clutter reduction methods including the data-dependent minimum variance distortionless response (MVDR) algorithm, data-independent null steering algorithm and beam-spaced clutter power estimation algorithm, and presents the data processing results. Chapter 7 summarizes the main work of the dissertation and recommends further studies.

Chapter 2: MCRDS Radar Systems

This chapter describes in detail the two radar systems of the multi-channel radar depth sounder (MCRDS). Throughout this dissertation, the two radar systems will be referenced as MCRDS Twin Otter system and MCRDS P-3 system according to their different configurations on the Twin Otter and P-3 aircraft. All the proposed algorithms and data processing in this dissertation are directly related to the two radar systems with the purpose of improving their performance and obtaining the best results from the collected data. The detail system designs can be found in reference [13, 15].

2.1 MCRDS Twin Otter System

In 2006, CReSIS finished the design of the Multi-Channel Radar Depth Sounder (MCRDS), which is an airborne system with high sensitivity. The system's operation band is from 140Hz to 160MHz and the overall loop sensitivity is 217 dB. The system has five separate receiving channels with an antenna array of five elements to provide beamforming capability in post data processing. This system was installed on Twin-Otter aircraft and used to collect data over the Greenland ice sheet in May and June 2006. As shown in Figure 2.1, the MCRDS Twin Otter consists of an arbitrary waveform generator (AWG), a transmitter, a five-element transmitting array, a five-element receiving array, five receivers and five data-acquisition cards (DAQ).

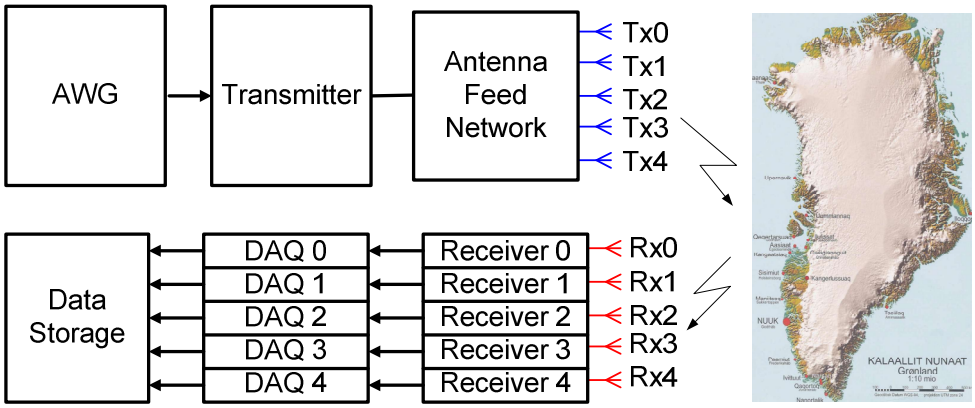

Figure 2.1: MCRDS Twin Otter System Block Diagram

The AWG is a programmable waveform generator that provides the flexibility to generate any desired waveforms and the means to control range sidelobes. The sampled and digitized desired waveforms are loaded into the AWG, which sequentially reads the waveforms and coverts them into analog signals with a digital-to-analog (D/A) converter. The detailed description of the original AWG design is given by Tammana [16]. In the operation of the MCRDS Twin Otter, the AWG generates linear chirps of 3us and 10us from 20 to 40 MHz with in-phase and quadrature components. The short pulses of 3-μsec are used to detect the air-ice interface and shallower ice depths, and the long pulses of 10-μsec are used to detect the deeper ice depths. The power level of AWG output is 4dBm.

The transmitter accepts the in-phase and quadrature signals from the AWG and employs an IQ modulator and a 120Hz LO to produce the desired signals in the band from 140 to 160 MHz. The up-converted signals are bandpass filtered, amplified

to a level of 800 Watts (59dBm) across the five transmit channels, and sent to the antenna feed network to be transmitted into the air and ice sheet by the antenna array. The short and long pulses are alternatively transmitted by each transmitter channel at a total repetition frequency (PRF) of 10 KHz, with an effective PRF of 5 KHz either for short or long pulses, as illustrated in the timing diagram of the radar in Figure 2.2.

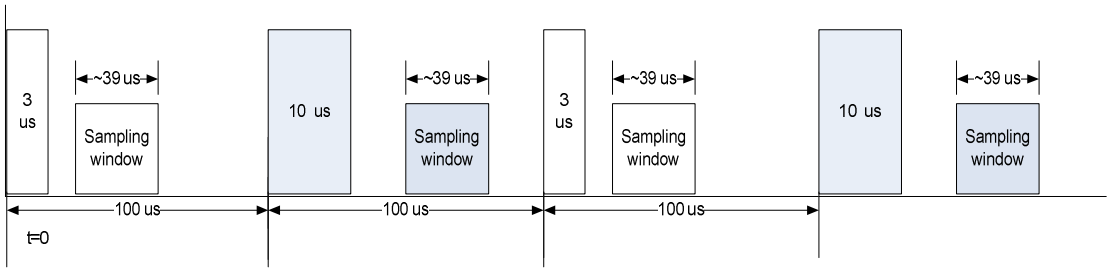

Figure 2.2: Time Diagram of MCRDS Systerms

The function of the antenna feed network is to implement a Hanning window across the transmit array using different attenuators to control the transmit power of each element so that the sidelobes of the transmit signals can be reduced.

The transmitting array provides the ability to reduce the sidelobes of transmit signals, and the receiving array provides the ability to perform digital beam forming in post data processing. Each element of the array is a quarter wavelength (0.5m) folded dipole with a gain of about 4.8dB. In the 2006 field survey, the transmitting array was installed under the left wing of the Twin Otter aircraft and the receiving array was installed under the right wing of the Twin Otter aircraft, as illustrated by

Figure 2.3. Each element is a quarter wavelength (0.5m) away from the underside of the wings. The positions of the transmitter elements and the receiver elements are symmetric about the aircraft's centerline. The lateral distances between the elements from inside to outside are 1.25m, 1.25m, 0.98m, and 0.95m. They are not uniformly spaced because of the physical limitations of the aircraft wings. The aircraft wings have a tilt of about 3 degrees above the horizontal. The wing angle effect on the transmitter was compensated for by properly adjusting the feed cable length for each transmitter element. The detail description of the antenna arrays' calibration is given in reference [17].

Figure 2.3: MCRDS Receiver Array on Twin Otter

The receiver bandpass filters and amplifies the echoed signals from ice sheets to the level required by the A/D converter of the DAQ. The noise floor of the receiver is 97dBm. Each receiver has low gain channels and high gain channels, which deal with the short pulse and long pulse respectively. The gain control is realized with two

digital attenuators. A total attenuation of about 43dB is set for the low gain channels in order to avoid the receiver saturation from the strong surface returns. A total attenuation of about 20dB is set for the high gain channels for the detection of weak signals from the deep layers and the ice bed.

The RF signals from the receiver are digitized by the analog-to-digital (A/D) converter of the DAQ at a sampling frequency of 120Hz. Every 64 adjacent records of the short pulse and long pulse are respectively averaged. This operation is referenced as pre-sums. Pre-sums is performed because of the hardware memory and speed limitation. The original design of the DAQ is given in [18].

Table 2.1: MCRDS Twin Otter System Parameters

Parameter	**Value**	**Units**
Frequency band	140 to 160	MHz
Pulse Duration	3 or 10	μs
Pulse Repetition Frequency	10	kHz
Output Power	800	W
Receiver Noise Figure	3.9	dB
Loop Sensitivity	217	dB
Minimum Detectable Signal	-161	dBm
Range Resolution	4.2	M01
Coherent Averages	64	
Antenna Element	$\lambda/2$ dipole	
Antenna Gain	4.8	dB
A/D Converter	12	bit
Sampling Rate	120	MHz

Finally, the decimated data from pre-sums are sent to storage for post processing. The stored records are time stamped by a radar computer. MCRDS systems are operated together with differential GPS receivers, which provide the

geographic information for radar data. Table 2.1 is a summary of the MCRDS Twin Otter system's parameters.

2.2 MCRDS P-3 System

In 2007, the MCRDS Twin Otter system was modified to add another band from 435MHz to 465MHz for the Global Ice Sheet Mapping Orbiter (GISMO) project (http://bprc.osu.edu/rsl/gismo/). The modified version of the system radar was installed on the P-3 aircraft and used to collect data over the Greenland ice sheet in September 2007.

The major modifications of the MCRDS P-3 system include:

1) An interferometric mode with an operation band from 435MHz to 465MHz is added in addition to the normal depth sounder mode with operation band from 140MHz to 160MHz.
2) The antenna array element is changed from a quarter wavelength folded dipole to a half wavelength dipole. The element number of antenna arrays is reduced from five to four. The spacing between elements is uniform (0.85m). The detail design is given in [19].
3) The transmit power is increased to1600W for interferometric mode.
4) In depth sounder mode, the left array is transmitting and the right array is receiving. In interferometric mode, the inboard element on either

side transmits alternatively in ping-pong mode, and the six outboard elements all receive.

5) The number of onboard coherent integrations is reduced to 32 to increase sampling frequency in the Doppler domain.

6) The transmitted chirp was tapered to reduce sidelobes from Fresnel ripples.

Chapter 3: Pulse Compression Waveform Design

First, this chapter introduces the basic concept of pulse compression which is an important technique employed in radars to detect distant targets with high resolution. Second, it discusses in detail the design of tapered-linear chirp and binary complementary-coded waveforms used by MCRDS radars to reduce range sidelobes. Finally, it presents the verification and analysis of the sidelobe performance of both types of waveforms with simulation, laboratory measurements and field-survey data.

3.1 Pulse Compression Technique

A brute-force method to obtain higher radar sensitivity is to increase the transmit power, transmit- and receive-antenna gain and reduce receiver noise. However this method is limited by hardware design and considerations of cost, safety and radar size and weight. An efficient way is to increase the signal-to-noise ratio using pulse compression and other signal processing techniques. By pulse compression, frequency- or phase-coded long pulses are transmitted and received pulses are decoded to obtain short and high-peak pulses. A short-pulse gives high range resolution required by many applications and the high peak power gives the energy required for detection of distant targets. There are limitations to directly transmitting a very short pulse with a high-peak power. The generation of high-peak power pulses requires very high voltages that may result in breakdown of transmission lines used to connect the transmitter to the antenna. On the other hand, pulse-

compression allows a system to simultaneously achieve the energy of a long pulse and the resolution of a short pulse without high peak power. Therefore pulse compression is a common and important technique that has been utilized not only in radar applications, but also in a wide range of other applications like sonar and ultrasonic imaging [20-25].

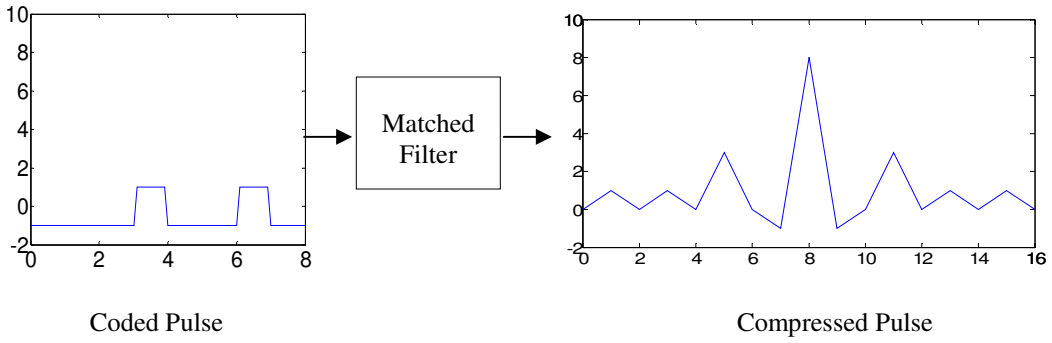

Figure 3.1: Illustration of Pulse Compression

Pulse compression is usually implemented by a matched filter that correlates the received signal with the transmit signal, which is equivalent to convolving the received signal with the reversed transmit signal. Matched filtering is linear and optimal as it maximizes the signal-to-noise ratio for additive white noise. As illustrated in Figure 3.1, a pulse with magnitude of 1 is phase-coded with an 8-bit binary code (0 0 0 1 0 0 1 0), and at the output of the matched filter, the waveform is compressed into a main lobe with symmetric sidelobes extending on both sides. The magnitude of the main lobe is increased from 1 to 8, and its width is 1/8 of the original pulse length. Pulse-compression ratio and sidelobe are two parameters used to

describe the performance of pulse-compression radar. Pulse-compression ratio is defined as the ratio of the original long pulse width to the short duration of the main lobe of the compressed pulse. This parameter defines the gain obtained in resolution and signal-to-noise ratio because of pulse compression. Sidelobes are undesired artifacts from pulse compression as they may mask adjacent weak signals. The following parameters are defined to describe the sidelobe properties of pulse compression [26]:

$$PSL = 10\log[Max(x_i^2)/x_0^2] \tag{3.1}$$

$$ISL = 10\log[\sum_{i=0}^{N} x_i^2 / x_0^2] \tag{3.2}$$

where x_i represents the magnitude of all sidelobes and x_0 is the magnitude of the main lobe. PSL, the peak sidelobe level, is a measure of the largest sidelobe as compared with the main lobe. ISL, the integrated sidelobe level, is a measure of the total power in the sidelobes as compared with the main lobe power.

A number of frequency-modulated and phase-modulated waveforms have been widely studied to get the best pulse-compression performance in terms of compression gain and sidelobe level. Linear chirp, nonlinear chirp and Costas codes are examples of frequency-modulated waveforms [21, 26, 27]. Barker codes, binary complementary codes and polyphase codes are examples of phase-modulated waveforms [28-30].

3.2 Tapered Linear Chirp Design

3.2.1 Theoretical Analysis

The general linear chirp signal in complex notation is

$$s(t) = A(t)\exp([\, j2\pi(f_0 t \pm \frac{B}{2T}t^2)] \ , \quad -\frac{T}{2} \le t \le \frac{T}{2} \tag{3.3}$$

where t is the time, $A(t)$ is the amplitude, f_0 is the center frequency, B is the bandwidth over which the chirp is swept in the duration of T. The phase of the chirp is a quadratic function according to equation (3.3):

$$\varphi(t) = 2\pi(f_0 t \pm \frac{B}{2T}t^2) \tag{3.4}$$

The instantaneous frequency is given by

$$f(t) = \frac{1}{2\pi}\frac{d\varphi(t)}{dt} = f_0 \pm \frac{B}{T}t \tag{3.5}$$

where f(t) is a linear function of time. So the linear chirp is often called linear-frequency modulation (LFM) signal. The parameter B/T is the frequency change rate and referred to as the chirp rate. The signal is called up-chirp when the frequency is swept from $f_0 - B/2$ to $f_0 + B/2$ corresponding to the plus sign in equations (3.3) ~ (3.5). The signal is called down-chirp when the frequency is swept from $f_0 + B/2$ to $f_0 - B/2$ corresponding to the negative sign in equations (3.3) ~ (3.5). Only the up-chirp will be used in the following discussion without losing the generality.

For a linear-chirp with a rectangular real envelope ($A(t) = 1$), the signal described by equation (3.3) can be written as

$$s(t) = u(t)\exp(j2\pi f_0 t) \tag{3.6}$$

where $u(t)$ is the signal's complex envelope and can be written as

$$u(t) = rect(\frac{t}{T})\exp(j\pi \frac{B}{T} t^2) \tag{3.7}$$

The matched filter output of this signal is its autocorrelation

$$R_{ss}(\tau) = \int_{-\infty}^{\infty} s(t)s^*(t-\tau)dt = \exp(2\pi f_0 \tau)\int_{-\infty}^{\infty} u(t)u^*(t-\tau)dt \tag{3.8}$$

Substituting equation (3.7) into (3.8), the matched filter response for the linear-chirp signal can be derived as

$$R_{ss}(\tau) = T(1-\frac{|\tau|}{T})\frac{\sin[\pi B\tau(1-\frac{|\tau|}{T})]}{\pi B\tau(1-\frac{|\tau|}{T})}\exp(2\pi f_0\tau), \qquad |\tau| < T \tag{3.9}$$

where $R_{ss}(\tau)$ is the well-known sinc function. For a chirp with large time-bandwidth product $TB >> 4$, the first null of $R_{ss}(\tau)$ occurs at $\tau_{1'st\ null} \approx \frac{1}{B}$ [31]. Therefore the pulse compression ratio is approximately $\frac{T}{\tau_{1'st\ null}} = TB$. However, as shown in Figure 3.2, the sidelobes level from pulse compression for the linear-chirp is relatively high. The first sidelobe is only 13.2 dB below the main lobe. The far sidelobes fall off at approximately 6 dB per octave and the first sidelobe nulls are spaced approximately 2/B apart.

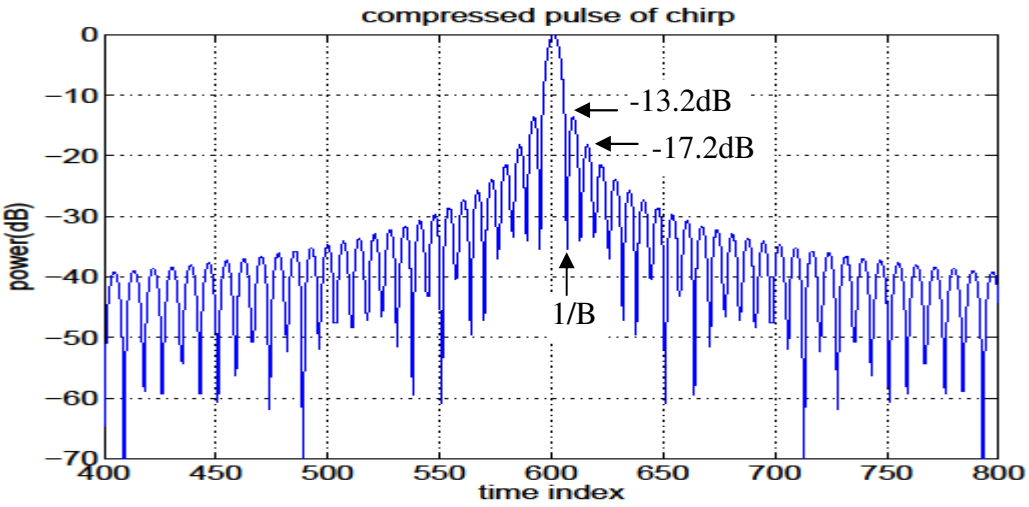

Figure 3.2: Matched Filter Output of Linear Chirp

The high-level sidelobes in time domain are caused by the approximate rectangular shape of the linear-chirp's spectrum. This is similar to the spectrum of a rectangular function in time domain. With this in mind, it is intuitive to understand the high-level sidelobes can be reduced by shaping the spectrum. Many window functions such as Hamming, Blackman and Dolph-Chebyshev are available for this purpose. The cost of applying windows is a broadening of the compressed pulse width and a small loss in signal-to-noise ratio. As the frequency is linearly changing with time, if the amplitude of the transmit signal is higher at any given time, the power spectral density at the corresponding frequency is also higher. Therefore the spectrum shaping can also be achieved by weighting the signal amplitude in time domain with suitable weighting functions. Theoretically, the spectrum should be shaped with the square root of the desired window weights both at the transmitter and receiver to maintain matched filtering. Applying window at the transmitter will

complicate the transmitter design and reduce transmit power as well. The alternative is to implement the entire weighting at the receiver. This is called mismatched filtering, which is used by our systems as well as by most other radar systems.

The solid-blue plot in Figure 3.3 shows the compressed pulse after a Chebyshev window is applied to the matched filter. It is observed that the near sidelobes are reduced below -80 dB but the sidelobe level at $\pm T/2$ rises to -40dB. According to the analysis performed by Misaridis and Jensen[32] and Cook and Bernfel[33], the distant sidelobes are caused by the Fresnel ripples in the transmit signal spectrum, as shown in the solid-blue plot in Figure 3.4 that corresponds to the linear chirp waveform at the top in Figure 3.5.

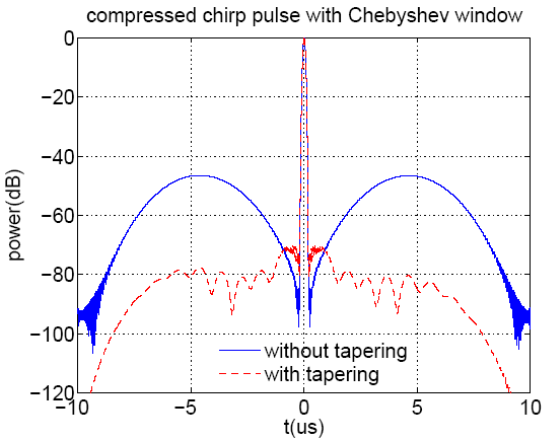

Figure 3.3: Mismatched Filter Outputs

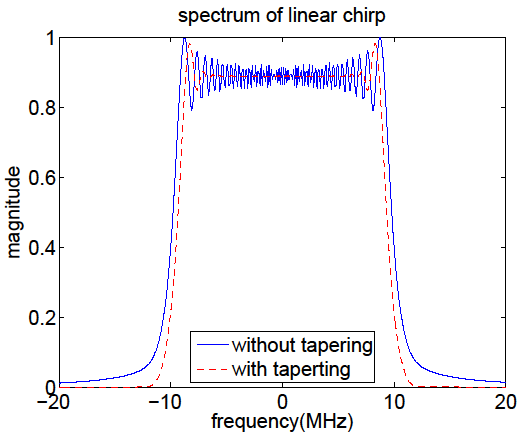

Figure 3.4: Spectra of Linear Chirps

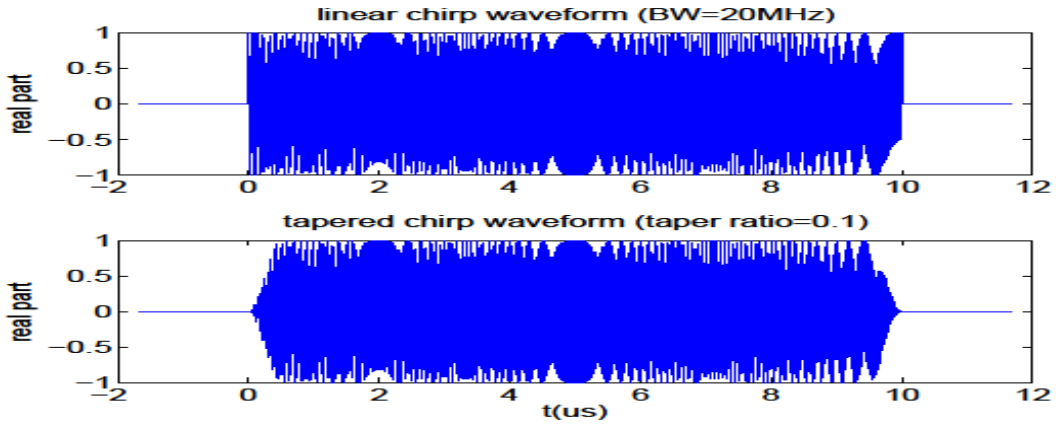

Figure 3.5: Waveforms of Chirp

The spectrum of the linear chirp is

$$S(f) = \int_{-\infty}^{\infty} s(t) e^{-j2\pi ft} dt \tag{3.10}$$

Substituting equations (3.6) and (3.7) into (3.10), the spectrum turns out to be

$$S(f) = \frac{1}{\sqrt{2B/T}} e^{-j\pi(f-f_0)^2/(B/T)} \{F_r(y_1) + F_r(y_2) + j[F_i(y_1) + F_i(y_2)]\} \tag{3.11}$$

where $F_r(y)$ and $F_i(y)$ are the real and imaginary components of the following complex Fresnel integral

$$F(y) = \int_0^y e^{j\pi\alpha^2/2} d\alpha = \int_0^y \cos\frac{\pi\alpha^2}{2} d\alpha + j\int_0^y \sin\frac{\pi\alpha^2}{2} d\alpha \tag{3.12}$$

and

$$y_1 = \sqrt{\frac{TB}{2}}(1 + 2\frac{f - f_0}{B}) \tag{3.13}$$

$$y_2 = \sqrt{\frac{TB}{2}}(1 - 2\frac{f - f_0}{B}) \tag{3.14}$$

The detailed derivation from (3.10) to (3.11) can be found in [32].

Figure 3.6 shows the Fresnel integrals $F_r(y)$ and $F_i(y)$ for y from 0 to 10. Misaridis and Jensen [32] studied several techniques to suppress the Fresnel ripples and concluded that amplitude tapering is the most efficient method. This technique is based on the observation that the Fresnel ripples are attributed to the sharp rise and fall of the waveform envelope at the start and the end as shown in the top plot of Figure 3.5. Therefore, if the abrupt rising and falling waveform edges are modified with smooth transitions as shown in the bottom plot in Figure 3.5, the Fresnel ripples in the spectrum will be reduced as shown by the dashed-red plot in Figure 3.4 and all the sidelobes would be reduced below -70dB as shown by the dashed-red plot in Figure 3.3.

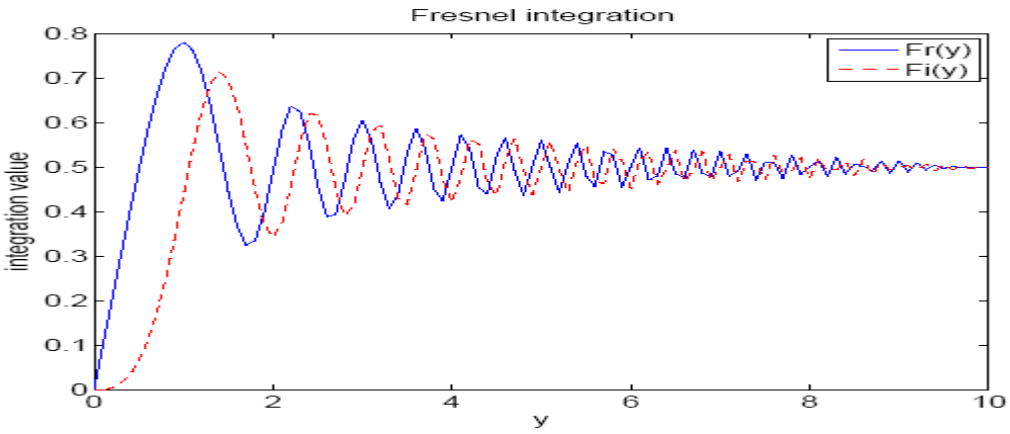

Figure 3.6: Fresnel Integrations

3.2.2 Simulation and Laboratory Measurements

With the above-described amplitude tapering technique, the sidelobe level is a function of the time-bandwidth product, weighting of the mismatched filter and the taper ratio. The bandwidth and waveform duration have been determined in system design and the time-bandwidth product is 60 and 200 for low-gain and high-gain mode, respectively. Chebyshev window is chosen for mismatched filter as it has the minimum mainlobe width for a specified constant sidelobe level. Thus the taper ratio is the only parameter that needs to be determined. The taper ratio is defined as the ratio of the tapered duration to the un-tapered one of the waveform, which is 0.1 in Figure 3.5. The signal energy loss is minimal for a small taper ratio of 0.1. The sidelobe parameters PSL and ISL defined by equations (3.1) and (3.2) are determined with simulations for different taper ratios from 0.05 to 0.3. The amplitude tapering is implemented with Tukey windows, which are cosine-tapers. A Tukey-window becomes a rectangular-window with zero taper ratios and a Hanning window with a taper ratio of 1. The simulation results are plotted in Figure 3.7 and Figure 3.8 for the 3us and 10us chirps respectively. According to Figure 3.7, the minimum PSL is about -50 dB at the taper ratio of 0.2. The ISL approaches -34.5dB at the taper ratio of 0.25 and does not reduce much beyond that. According to Figure 3.8, the minimum PSL is about -70 dB at the taper ratio of 0.1. The minimum ISL is about -50 dB at the taper ratio of 0.15 and increase slightly beyond that. It is found the compressed pulse width at -3dB does not change much over the swept taper ratio range.

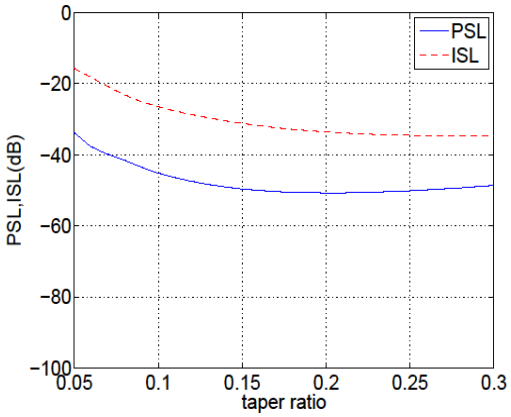

Figure 3.7: PSL and ISL for 3us Chirp

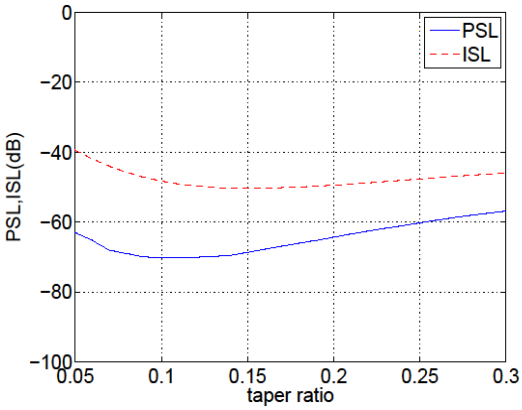

Figure 3.8: PSL and ISL for 10us Chirp

The actual taper ratios used by MCRDS P-3 radar were determined from laboratory measurements. The transmitter outputs were recorded first with an oscilloscope to make sure the sidelobe level is low for transmit signals. And then data were recorded using the radar DAQ with the radar configured in a loop-back delay-line mode to include the overall system effects [34]. The actual taper-ratio was determined to be 0.25 for 3 us chirp and 0.2 for 10 us chirp based on the actual system measurements. The top plot in Figure 3.9 shows the tapered-linear transmit chirp of 10-us with a taper ratio of 0.2. The bottom plot shows the compressed pulse with the PSL close to -70 dB. The top plot in Figure 3.10 shows the recorded tapered-linear chirp of 3-us with a taper-ratio of 0.25. The bottom plot shows the compressed pulse with the left PSL is -60 dB, the right PSL is -50 dB and the distant sidelobes are at -70 dB. The asymmetry is the result of the waveform distortions by system effects. The delay-line measurements used to generate Figure 3.10 were recorded on September 12, 2007, right prior to the real survey data collection.

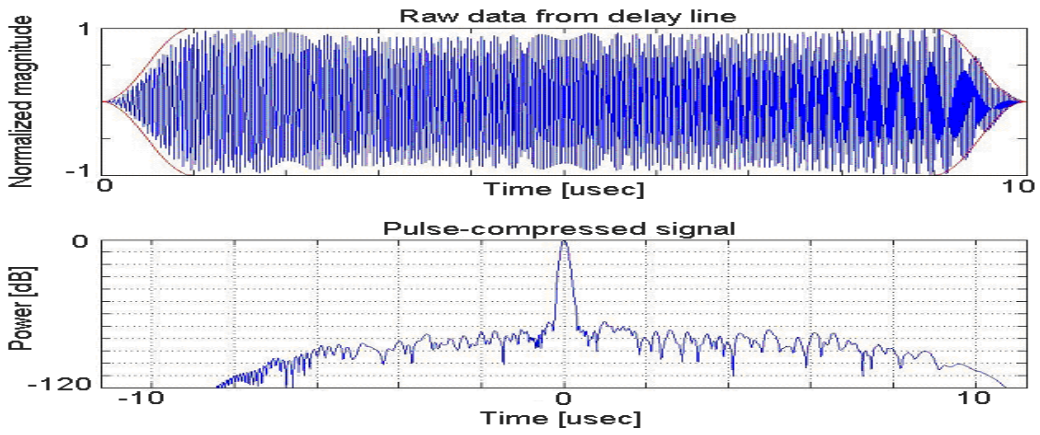

Figure 3.9: 10us-Tapered Chirp Used by MCRDS P-3

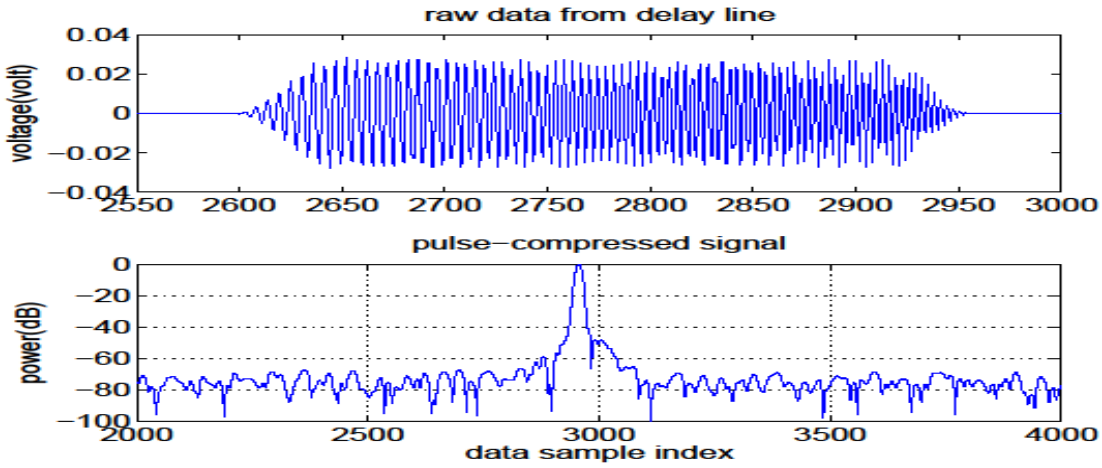

Figure 3.10: 3us-Tapered Chirp used by MCRDS P-3

For some applications where further sidelobe suppression is required, it can be achieved by applying two-way windowing (the same window function applies to both the reference function and the received data) in frequency domain with a loss in SNR

and resolution. By simulation, Figure 3.11 illustrates the sidelobes from pulse compressions with two-way windowing compared with that of mismatched compression in Figure 3.3. It is observed that without amplitude tapering the distant sidelobes at $\pm T/2$ are still around -40dB although the close sidelobes are suppressed from -83dB to -123dB, and with amplitude tapering, the distant sidelobes at $\pm T/2$ are suppressed to near -80dB and the close sidelobes are suppressed from -70dB to -90dB. Because the sidelobes fall rapidly beyond $\pm T/2$, the compressed pulses are plotted only within the duration of $\pm T/2$ instead of $\pm T$ in Figure 3.11, the following Figure 3.13(b) and Figure 3.14(a) so that more sidelobe details can be seen.

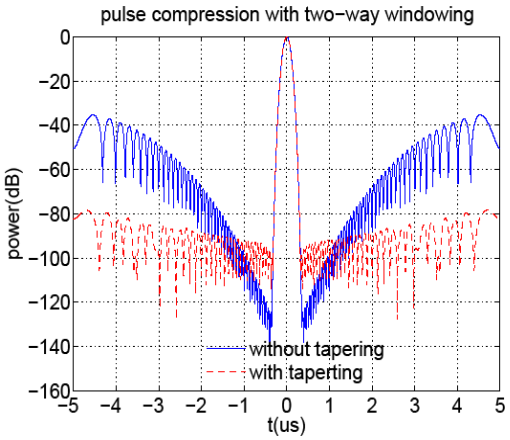

Figure 3.11: Pulse Compression (Two-way Windowing)

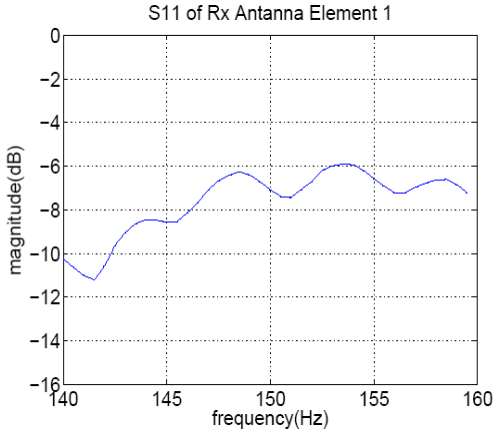

Figure 3.12: S11 of Antenna

However, it should be pointed out such low sidelobe levels are obtained by simulation with ideal waveforms. In the real world, waveform distortions in terms of amplitude modulation and phase noise are unavoidable because of the system imperfections and the changes in operation environment. Therefore, the effects of

waveform amplitude modulation and phase noise are simulated to assess their limitation on sidelobe suppression. The following amplitude modulation model is used in the simulation:

$$s_{am}(t) = s(t)(1 + A\sin 2\pi f_{am} t) \tag{3.15}$$

where $s_{am}(t)$ is the waveform with amplitude modulation, A is the modulation index and f_{am} is the modulation frequency. In Figure 3.13(a), the blue plot is the real part of the baseband ideal tapered-chirp of 10 us, and the red-dashed plot is the real part of the waveform with amplitude modulation. The amplitude modulation index is 0.1 and the modulation frequency is 4 cycles in 10 us based on actual measurements of the antenna element's scattering parameter S11(see Figure 3.12) using network analyzer. Figure 3.13(b) is the corresponding compressed pulses. According to Figure 3.13(b), the main effect from amplitude modulation is the broadening of the compressed pulse with two secondary peaks on both sides. The modulation frequency determines how much the main pulse will widen and the modulation index determines the level of the secondary peaks. The phase noise in the simulation is assumed to be normal random. Figure 3.14(a) shows the compressed pulse with phase noises with a standard deviation $\sigma_n = 0.2^\circ$ compared to that from the ideal waveform. It is observed that the phase noise effect is to increase sidelobe levels. Figure 3.14(b) plots PSL and ISL versus phase noise level σ_n from 0° to 5° at a step of 0.1°. According to Figure 14(b), the phase noise cannot exceed 2° and 0.5° respectively for -60 dB and -70 dB sidelobe levels even with two-way windowing.

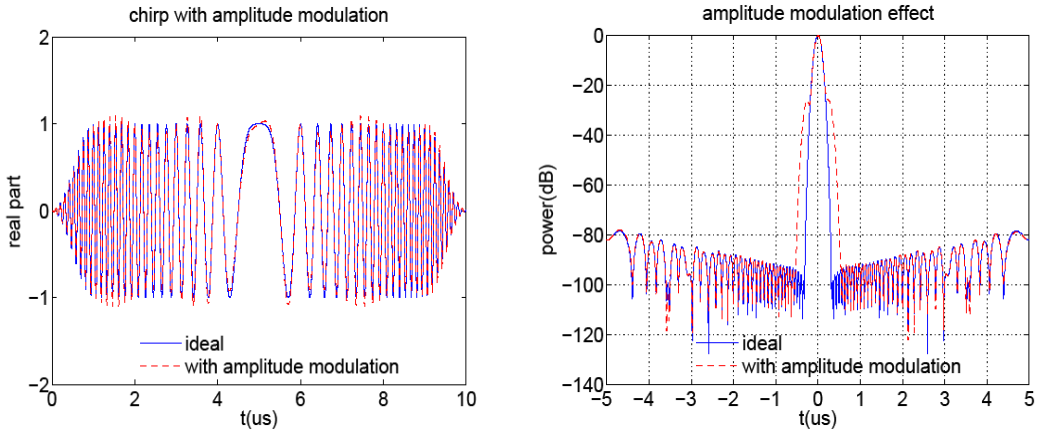

(a) (b)

Figure 3.13: Amplitude Modulation Effects (a) Waveforms (b) Compressed Pulses

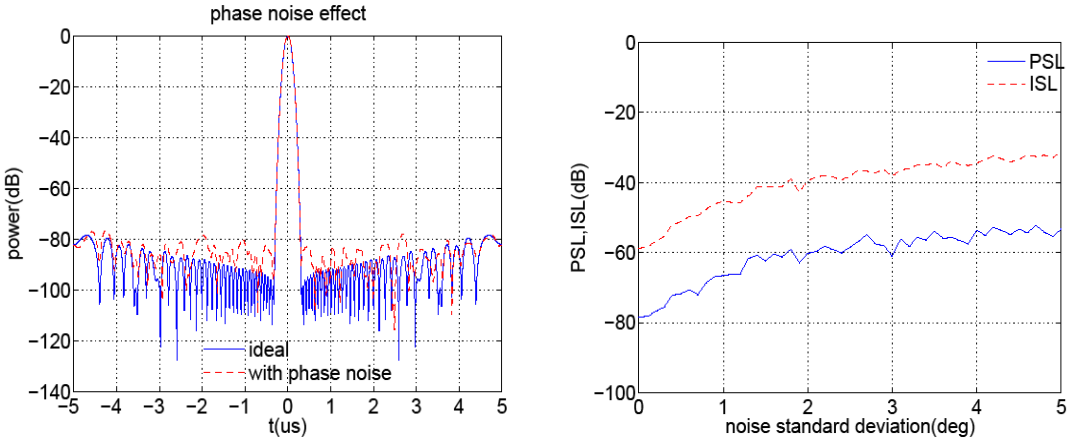

(a) (b)

Figure 3.14: Phase Noise Effects (a) Compressed Pulses (b) PSL, ISL ~ σ_n

3.2.3 Sidelobe Level Validation with Field Survey Data

The actual effectiveness of the amplitude-tapering technique for sidelobe suppression has to be verified with radar data collected during a survey flight so that we have confidence that the sidelobe will not be an issue in data interpretation. Very clean and strong echoes have to be used for this purpose. For example, in order to verify the sidelobe is -50 dB lower for 3-us linear-chirp signal, the SINR (signal-to-interference-plus-noise ratio) has to be higher than 50 dB. Usually only the echoes from ocean surface, smooth ice surface, flat ice bed with melting at shallow depth can have such high SINRs.

As the first evidence, we compare the sidelobes of compressed ocean-surface echoes from data collected by MCRDS in 2006 and in 2007. In field surveys of 2006, we did not taper the transmit linear chirp. In field surveys of 2007, we tapered the transmit linear-chirp with the taper ratios determined from the laboratory measurements. Figure 3.15(a) shows a radar echogram from the data collected by MCRDS with 3-us chirp over the ocean on May 20, 2006 when the Twin-Otter was flying from Axel Heiberg Island to Meighan Island in Northeast Canada. The echogram is normalized to its maximum value and the color bar on the right gives the power levels relative to the maximum. The straight line around range bin index of 500 in the echogram is the ocean surface response. It is observed that sidelobes on both sides of the ocean surface are obvious in yellow color corresponding to a sidelobe range from -30 dB to -35 dB. The light blue straight line around range bin

index of 1100 is the multiple of the ocean-surface response. Figure 3.15(b) shows a radar echogram from the data collected with the 3-us tapered- chirp on September 13, 2007 when the P-3 aircraft was flying over the ocean along the Greenland coast. The first straight line is the transmitter feedthrough and the second straight line is the ocean surface response. It is observed that the sidelobes on the upper side of the ocean surface are around -60 dB. The third straight line in light blue is the multiple of the surface response. Figure 3.16(a) is a SAR image from the data collected with the 3-us tapered-chirp on September 13, 2007 over smooth-ice surface in Greenland. The red straight line around range bin index of 140 is the ocean surface response. It is observed from the upper side of the surface that most sidelobes are as low as -70 dB and the PSL is close to -60 dB as shown by the A-scope in Figure 3.16(b). Since the sidelobes have been suppressed to a very low level, they are usually below backscatterings on the trailing side of the ice surface. It is also observed from the A-scope that the SNR of the ice-surface is as high as 80 dB after SAR processing. Figure 3.17 (a) is a SAR image from the data collected with the 3-us tapered-chirp on September 17, 2007 in Greenland. A few strong ice-bed echoes of 50-dB SNR are observed in this image. No sidelobes are observed above the noise floor on the leading side of the bed echo from the A-scope shown in Figure 3.17 (b).

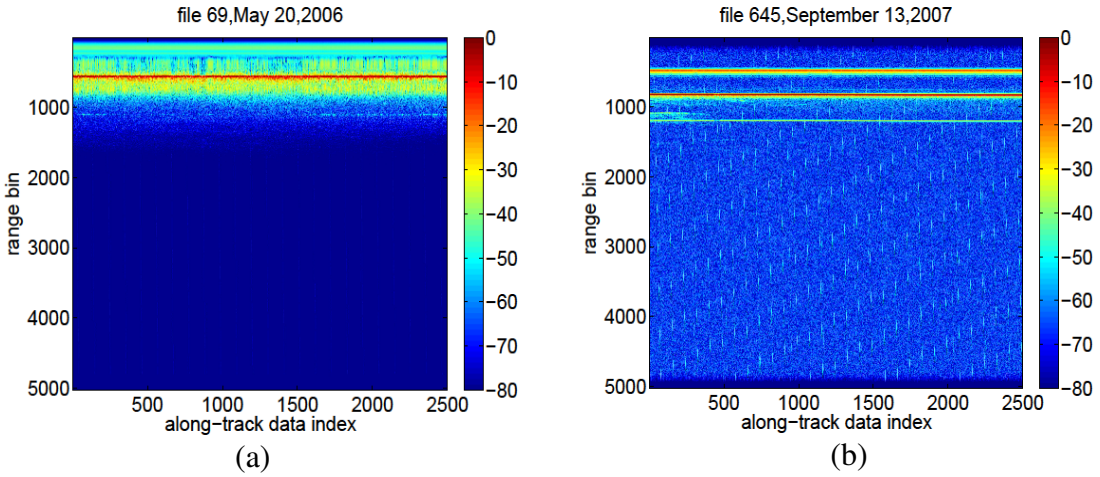

Figure 3.15: 3-us Chirp Ocean Surface Responses: (a) MCRDS Twin Otter; (b) MCRDS P-3

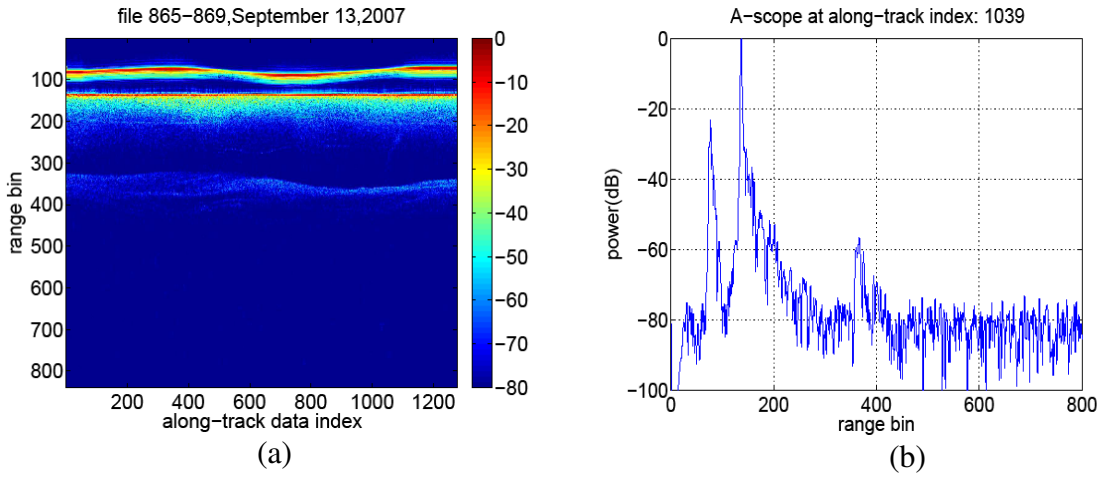

Figure 3.16: 3-us chirp (a) Ice Surface Response (b) A-scope

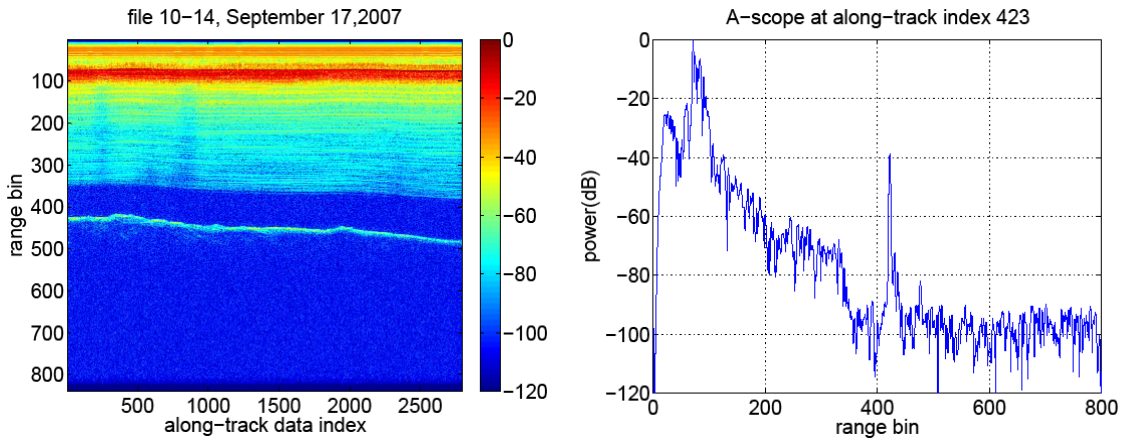

Figure 3.17: 3-us Chirp (a) Ice Bed Response (b) A-scope

Since the sidelobe level has been suppressed to a very low level for the linear-chirp of 10 us (below -60 dB), a very high SNR is required for the verification. In most cases the SNR of bed echoes cannot achieve as high as 60 dB even after SAR and incoherent integration in post processing. This is due to large ice attenuation. And in the operation the radar usually does not record strong echoes from ocean or ice surface when the aircraft height is low to avoid the receiver being saturated. The radio frequency interference (RFI) is also a factor limiting the radar's sensitivity of its high-gain mode. Therefore there are only a few files in the 2007-data that have SNR higher than 60 dB and can be used to verify the sidelobe performance for the longer waveform. Figure 3.18 shows A-scopes of the ocean surface with the 10-us tapered-chirp. The data file is the same as that of Figure 3.15(b); the radar echogram is also similar and therefore not presented here. The blue plot is the A-scope from the single pulse at along-track index of 1050. The sidelobes on the leading side of the ocean

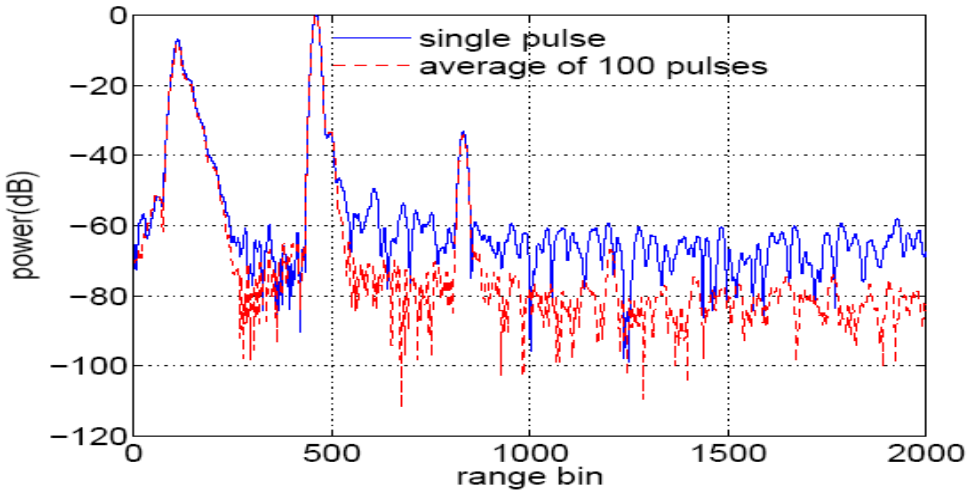

Figure 3.18: 10-us Chirp A-scope of Ocean Surface

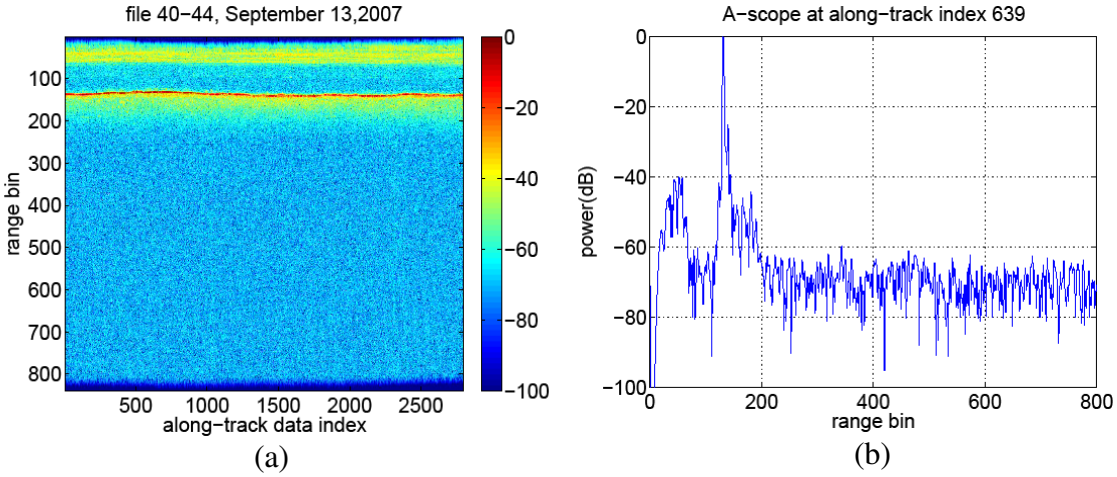

Figure 3.19: 10-us Chirp (a) Ice Bed Response (b) A-scope

surface are observed at least -60 dB. By averaging the 100 pulses between the along-track indexes 1001 and 1100, the noise level is suppressed below -80 dB as shown in the red-dashed plot. And it is clear the PSL is around -64 dB which matches the simulation in Figure 3.8 at the taper ratio of 0.2. Figure 3.19 (a) is a SAR image

from the data collected with the 10-us tapered-chirp on September 17, 2007 in Greenland. The straight line around range bin index of 140 is the ice bed. The depth is about 1200m. A few strong ice bed echoes with SINR of 60dB are observed in this image. No sidelobes are observed above the noise floor on the leading side of the bed echo from the A-scope shown in Figure 3.19 (b). This at least proves that the sidelobe level of -60 dB has been achieved at the ice bed, which is the science requirement for mapping deep layers near to the ice bed.

3.3 Complementary-coded Waveforms Design

3.3.1 Binary Complementary Codes

Golay first comprehensively studied the properties and synthesis methods of binary complementary codes in 1960[35]. Therefore, binary complementary codes are also referred as Golay codes. Golay defined a pair of complementary codes as two equally long finite sequences of two kinds of elements. Within these sequences, the number of pairs of like elements with any given separation in one sequence is equal to the number of pairs of unlike elements with the same separation in the other sequence. Figure 3.20 shows a pair of complementary codes A (00010010) and code B (00011101) to help understand the definition. Each code has a length of 8 bits, and the two kinds of elements are 1 and 0. In the figure, L is used to denote a pair of like elements and U for a pair of unlike elements in code I or code II. For the given separation of 2, it is shown that code I has one pair of unlike elements and four pairs

of like elements, and code II has four pairs of unlike elements and one pair of like elements. The property holds for any other separations like 0, 1, 3 etc.

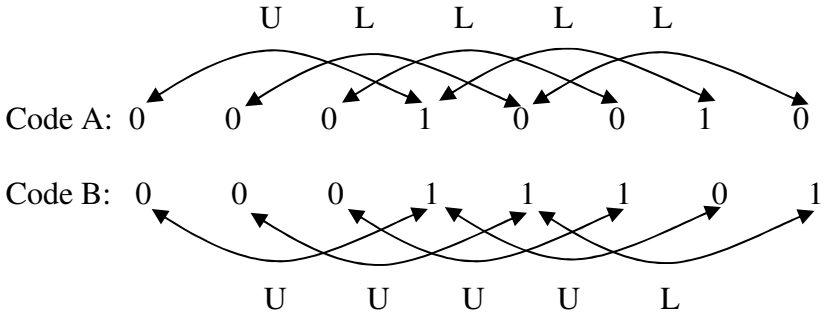

Figure 3.20: A pair of Complementary Codes

The autocorrelation functions of a pair of complementary codes R_A and R_B have a unique property described by the following equation (3.16) if the code elements a and b are either 1 or -1:

$$R_A(j) + R_B(j) = \begin{cases} 2N & j = 0 \\ 0 & j \neq 0 \end{cases} \tag{3.16}$$

where

$$R_A(j) = \sum_{i=1}^{N-j} a_i a_{i+j} \tag{3.17}$$

$$R_B(j) = \sum_{i=1}^{N-j} b_i b_{i+j} \tag{3.18}$$

N is the code length in bits and $-(N-1) \leq j \leq (N-1)$. This property is illustrated in Figure 3.21 with the autocorrelation functions of code A and code B used in Figure

3.20. All the 0's in code A and code B are replaced with -1's to calculate the autocorrelation functions. In Figure 3.21, the red chart is the autocorrelation function of code A, the blue chart is the autocorrelation function of code B and the black chart is the sum of the two autocorrelation functions. The autocorrelation function of each code has a main lobe located at the center with a magnitude of 8 which is the code length, and the sidelobes of the two autocorrelation functions are opposed each other. The summed autocorrelation function cancels the sidelobes and only has a main lobe with a magnitude of 16 which is twice the code length. Because of this property, for two waveforms coded with a pair of complementary codes, the sidelobes of one compressed waveform would be opposite to the ones of the other at the output of the matched filter. Thus the sidelobes would totally be cancelled and the magnitude of the main lobe would double when the two compressed pulses are added together.

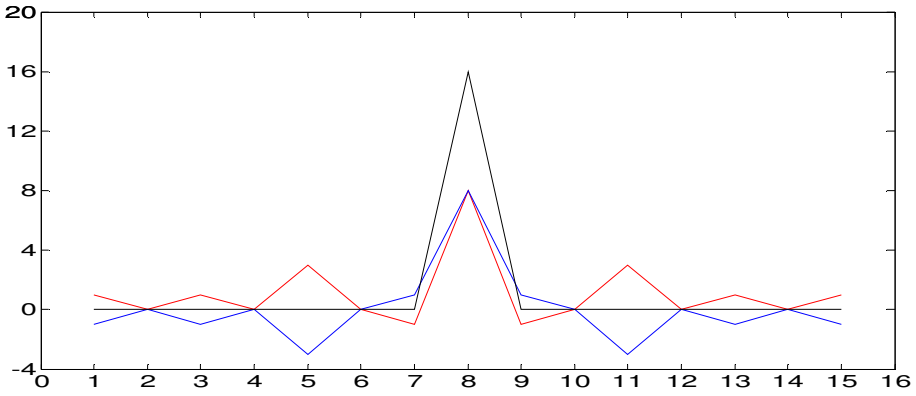

Figure 3.21: Autocorrelation Functions R_A (red), R_B (blue) and $R_A + R_B$ (black)

Golay presented synthesis methods to generate new complementary codes using known complementary codes as the seeds. These methods manipulate the seeds

by operations such as order reverse of elements, interchange of element kinds, appending and interleaving to obtain different complementary codes of the same or longer length. There is a recursive way to generate a specific kind of complementary codes called orthogonal Golay codes without the need for seeds [36]. The orthogonal Golay codes are used in wireless communication. The recursive generation scheme is illustrated in Figure 3.22 and described by equations (3.19) below:

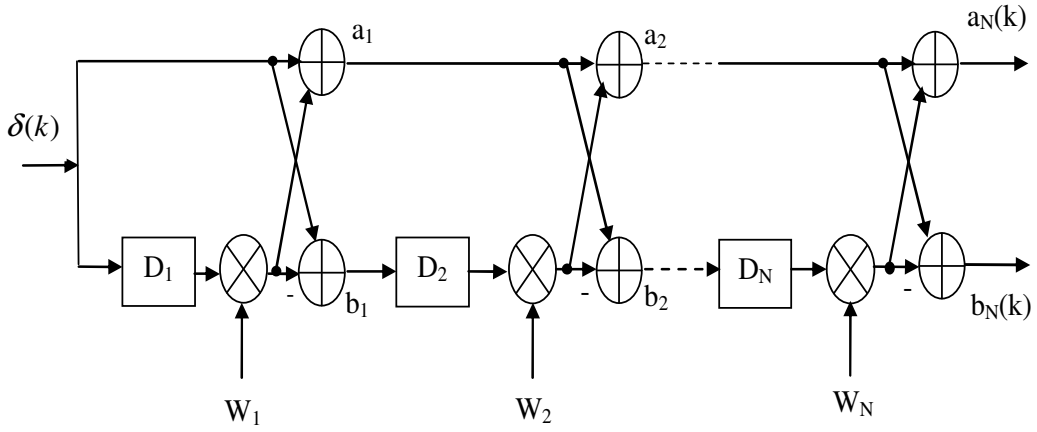

Figure 3.22: Recursive Complementary Codes Generator

$$
\begin{aligned}
a_0(k) &= \delta(k) \\
b_0(k) &= \delta(k) \\
a_n(k) &= a_{n-1}(k) + W_n b_{n-1}(k - D_n) \\
b_n(k) &= a_{n-1}(k) - W_n b_{n-1}(k - D_n)
\end{aligned}
\tag{3.19}
$$

where $\delta(k)$ is the Kronecker delta function, $k = 0,1,2,...,2^N - 1$ representing the time scale, $n = 1,2,...,N$ is the iteration number, $D_n = 2^{P_n}$ is a delay, P_n is any permutation of numbers{0,1,2,…,N-1}, W_n is an arbitrary complex number of unit magnitude for polyphase complementary sequences (if $W_n = 1 \; or \; -1$, the binary Golay codes are

obtained), $a_N(k)$ and $b_N(k)$ are the final two complementary codes of length $L = 2^N$. Another advantage of orthogonal Golay codes is that pulse compression can be performed with the corresponding Efficient Golay Correlator (EGC) which is much faster than general autocorrelation calculation and even faster than the match filtering with FFT and IFFT [37].

Complementary-coded-waveform design is straightforward once complementary codes are generated. Two parameters need to be first determined: 1) N, the number of bits or the length of the complementary codes; and 2) T, the pulse duration. For a pulse of fixed duration, the longer the codes, the bigger the pulse compression gain. But the bit number will be limited by the available bandwidth of the system and the sampling frequency. With N and T determined, the bit duration is determined according to $\tau = T / N$, and the binary phase shift keying (BPSK) modulation scheme can be applied to the carrier wave to generate the transmit complementary waveforms s_A and s_B:

$$s_A = \cos[2\pi f_c t + A(t)\pi] \tag{3.20}$$

$$s_B = \cos[2\pi f_c t + B(t)\pi] \tag{3.21}$$

where f_c is the carrier frequency, $A(t)$ and $B(t)$ equal 1 or 0, and $0 \le t \le T$.

A pair of complementary BPSK waveforms of 3.2 us is designed for low-gain mode and a pair of complementary BPSK waveforms of 8us is designed for high-gain

mode operation of MCRDS P-3. The two plots at the top in Figure 3.23 are the complementary codes of 32 bits generated with the recursive method. The two plots at the bottom are the corresponding BPSK waveforms of 3.2us coded with the complementary codes at the carrier frequency of 30 MHz. The two plots at the top in Figure 3.24 are the complementary codes of 80 bits generated with a pair of known complementary seeds of 10 bits. The two seeds are A_{10} = [1 0 0 1 0 1 0 0 0 1] and B_{10} = [1 0 0 0 0 0 0 1 1 0]. The complementary codes of 80 bits are obtained by recursively appending the seeds according to the following scheme:

$$A_{20} = [A_{10} \ , \ B_{10}], \ B_{20} = [A_{10} \ , \ -B_{10}] \tag{3.22}$$

$$A_{40} = [A_{20} \ , \ B_{20}], \ B_{40} = [A_{20} \ , \ -B_{20}] \tag{3.23}$$

$$A_{80} = [A_{40} \ , \ B_{40}], \ B_{80} = [A_{40} \ , \ -B_{40}] \tag{3.24}$$

where the minus in the above equations means bitwise operation NOT. For example, $-B_{10}$ = [0 1 1 1 1 1 1 0 0 1]. The two plots at the bottom in Figure 3.24 are the corresponding BPSK waveforms of 8us coded with the complementary codes at the carrier frequency of 30MHz. We can also use the recursive scheme describe by equations (3.19) to generate seeds A_{64}, B_{64} and A_{16}, B_{16} and then append them to get a pair of complementary codes of 80 bits.

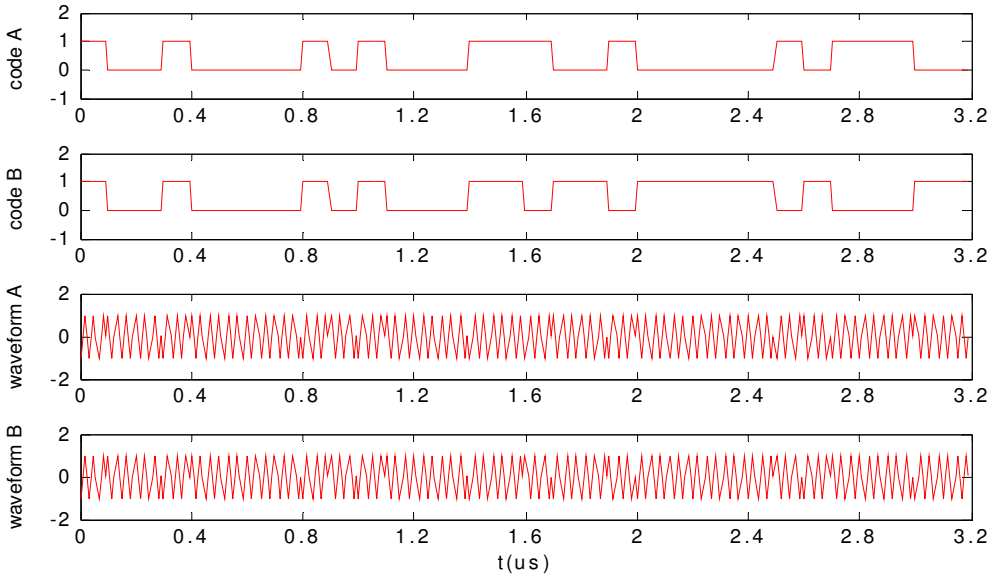

Figure 3.23: 32-bit Complementary Codes and 3.2us BPSK Waveforms

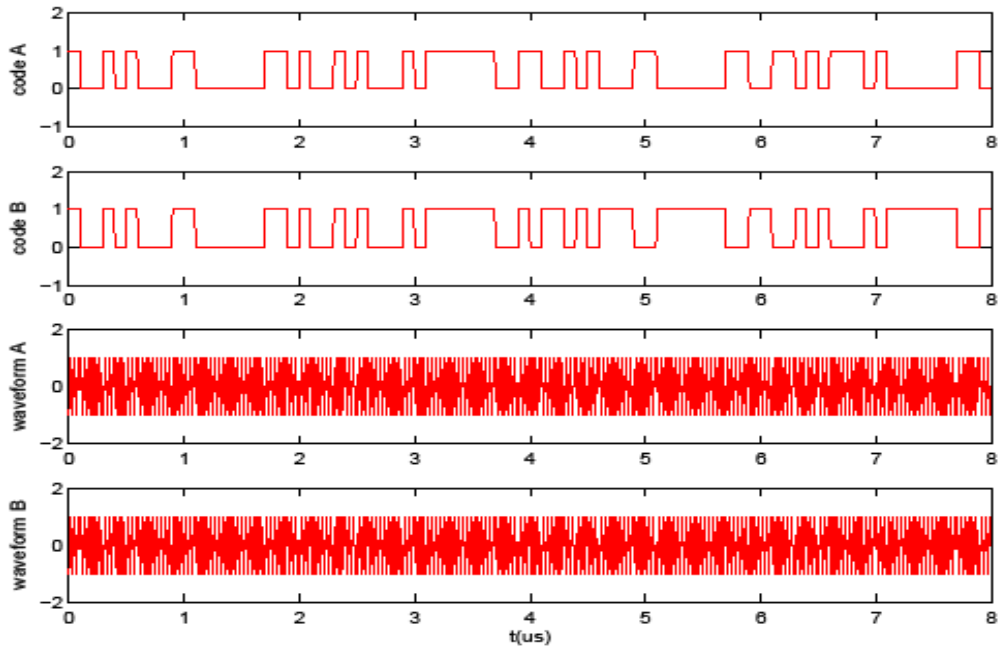

Figure 3.24: 80-bit Complementary Codes and 8us BPSK Waveforms

3.3.2 Effects of Amplitude Mismatch and Phase Shift

In implementation, the two complementary BPSK waveforms generated by AWG are up converted to the carrier frequency of 150 MHz by oversampling. The transmitter alternatively transmits the up-converted BPSK waveforms. On the other hand, the received signals are down converted to 30 MHz by under sampling. The down-converted signals from the two complementary waveforms are compressed and summed together in post data processing to cancel the sidelobes. For ideal case without waveform amplitude mismatch and phase shift, complete sidelobe cancellation is expected as illustrated in Figure 3.25. The two plots at the top are the compressed pulses for code A and B respectively with sidelobes. The two plots at the bottom are the sum of the two compressed pulses in linear and dB scales which show the sidelobe cancelation.

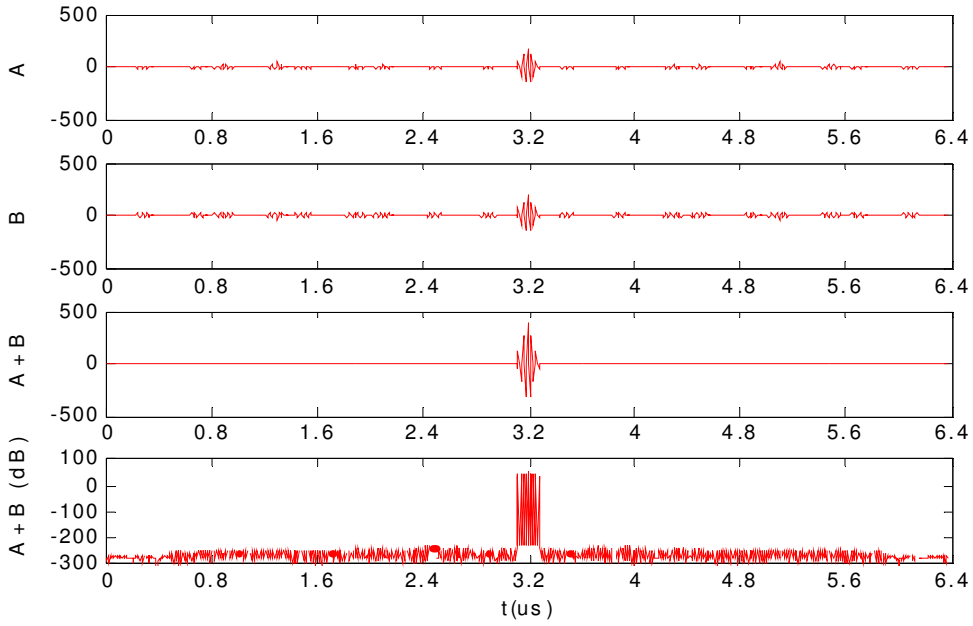

Figure 3.25: Sidelobe Cancellation in Ideal Case

However any signal distortions caused by hardware either in terms of amplitude and/or phase mismatches between the two complementary waveforms will result in sidelobes. The movement between the radar and targets will also result in phase shifts, which is a serious problem for some applications. Fortunately this is not a serious concern in ice mapping with a VHF-band airborne system at a PRF of 10 kHz as the Doppler shift caused by the aircraft motion between two complementary pulses is insignificant. The effects of magnitude mismatch and phase shifts on sidelobe level were studied in detail by simulation in [38]. The results are summarized in Figure 3.26 and 3.27. Figure 3.26 shows the PSL values for different amplitude mismatches (0.1%, 0.5%, 1%, 2%, 3%, 4%, 5%, 10%, and 20%). The percentage of the amplitude mismatch is defined as the amplitude difference between the two complementary waveforms over the amplitude of one of the two waveforms that is used as the reference. According to Figure 3.26, the amplitude mismatch would not exceed 1% in order to suppress PSL below -60dB, which is required to map the deep ice layers near the bed. Figure 3.27 shows the PSL values for different phase shifts (0.5°, 1°, 5°, 10°, 15°, 20° and 25°). The phase shift would not exceed 0.5° for a PSL level of -60dB according to Figure 3.27. It is observed that sidelobes are becoming more sensitive to amplitude mismatch and phase shifts at low levels.

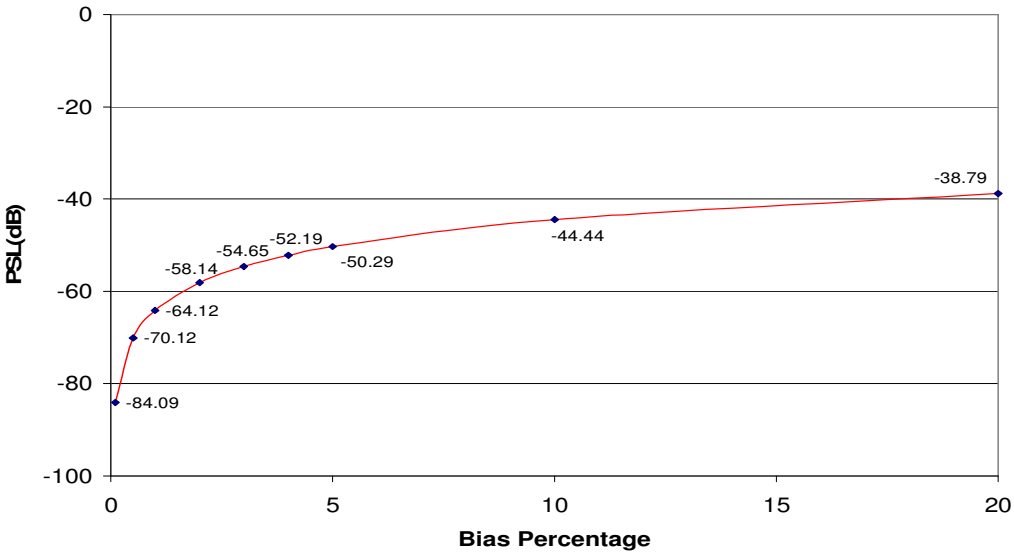

Figure 3.26: Sidelobe Level ~ Amplitude Mismatch

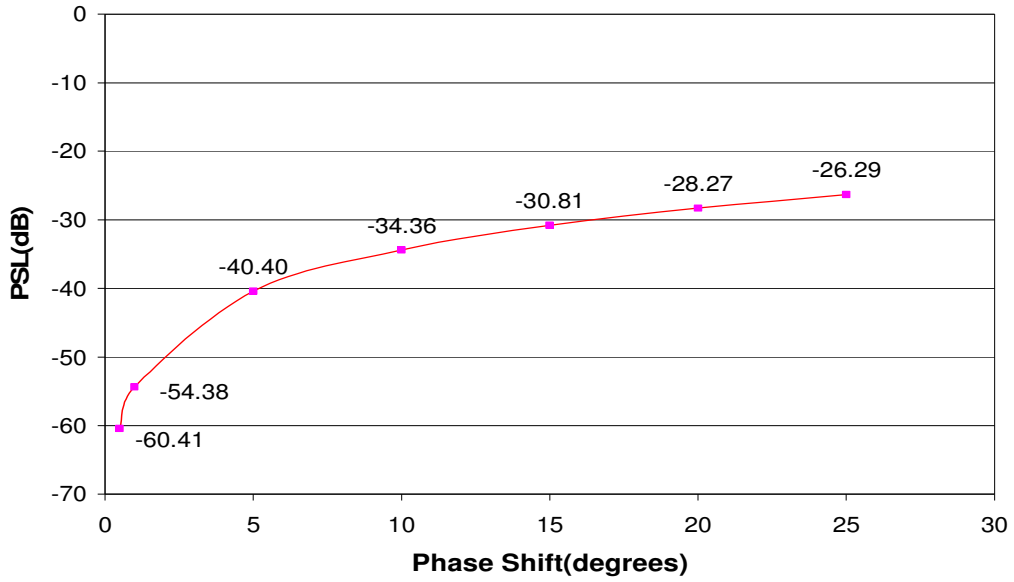

Figure 3.27: Sidelobe Level ~ Phase Shift

3.3.3 Laboratory Measurements and Field Survey Results

At the output of the AWG of MCRDS P-3 radar, the PSL of the generated complementary waveforms is -59.71dB according to the measurements with an oscilloscope. In [38], it is reported the PSL is -72.56dB for the complementary waveforms generated with the Model 2045 Arbitrary Waveform Synthesizer from Analogic Data Precision and -64.89dB with the DBS 2050 VXI Waveform Generator from Analogic Corporation [39, 40]. These measurements from different arbitrary-waveform generators further prove the hardware distortion sensitivity of complementary waveforms at low sidelobe levels. The overall system effects on the sidelobe performance of the designed complementary BPSK waveforms are evaluated by the loop-back delay line measurements in laboratory. The top two plots in Figure 3.28 are the actual two complementary BPSK waveforms of 3.2us recorded by the DAQ. The bottom plot is the compressed pulse and shows the sidelobes level is at -53.36dB. The sidelobe performance is the same for the complementary BPSK waveforms of 8us.

In order to test the sidelobe performance of complementary waveforms that had never been used by any radar systems for ice mapping, MCRDS P-3 used the designed complementary BPSK waveforms in 2008 Greenland field survey and collected few data samples both over ocean and ice. The ocean data were collected on July 25, 2008, and the saved files are archived in the file group 20080725B and

numbered from 0-8. The ice data were collected on August 1, 2008 and the saved files are numbered from 277-301.

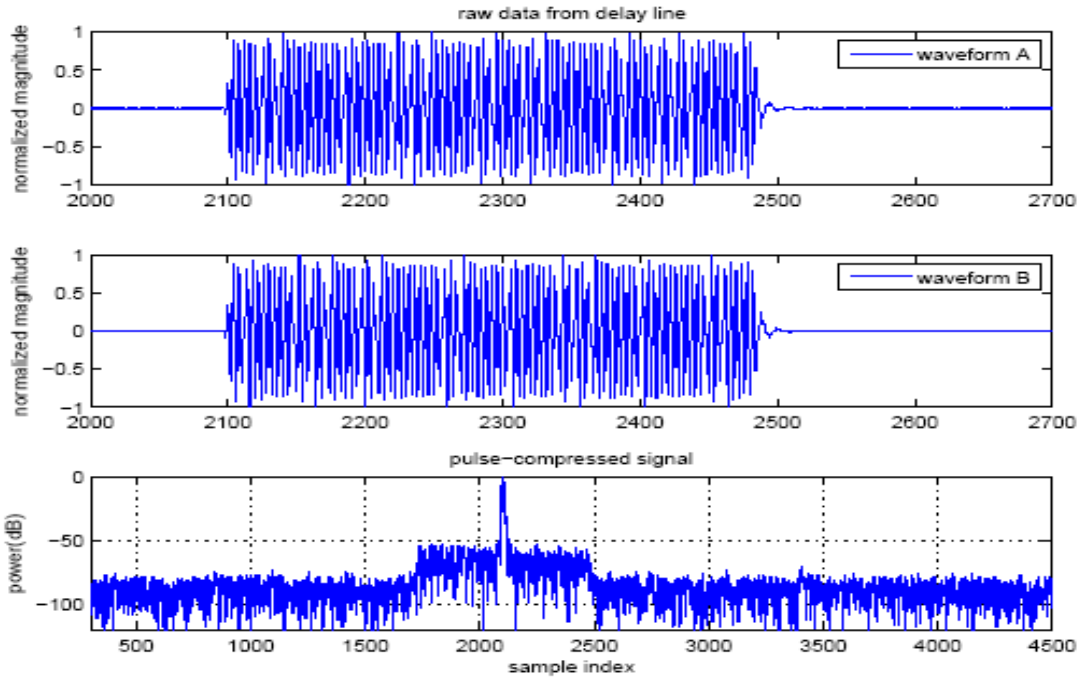

Figure 3.28: 3.2-us Complementary BPSK Waveforms Used by MCRDS P-3

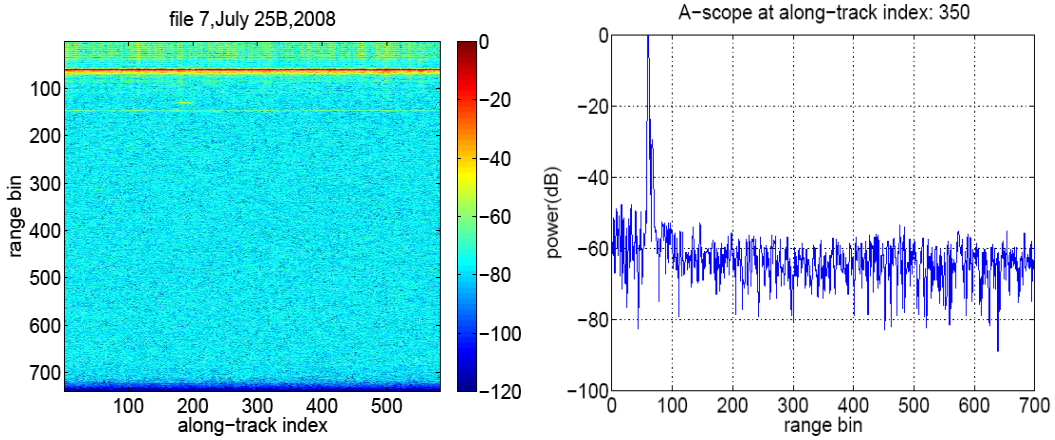

(a) (b)

Figure 3.29: (a) Ocean Surface Response, (b) A-scope

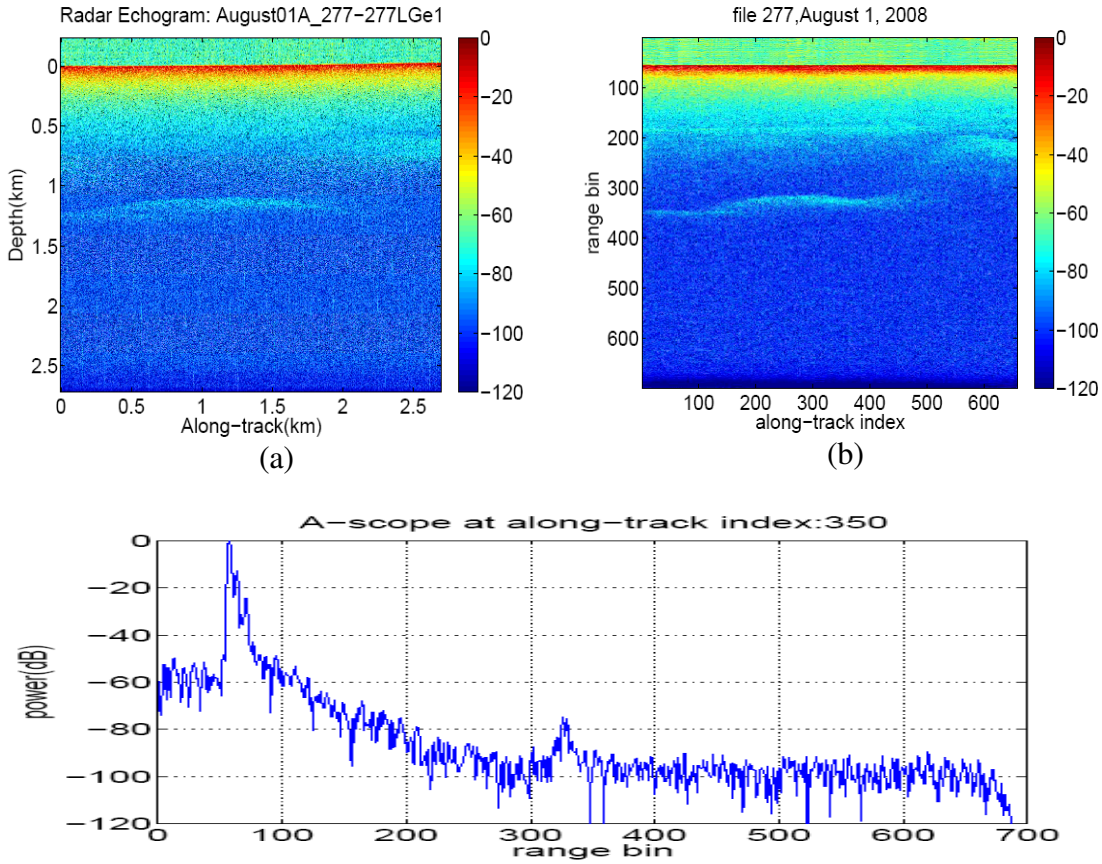

Figure 3.30: Ice Surface Responses of 3.2-us BPSK Waveforms

(a) Echogram (b) SAR image (c) A-scope

Figure 3.29(a) is a sample image from an ocean data file after pulse compression and SAR processing. The horizontal, straight and red line around range bin index of 60 is the ocean surface response to the BPSK waveforms. Figure 3.29(b) is the A-scope at the along-track index of 350 in the left image. The A-scope shows the SNR of the ocean surface is about 60 dB and the sidelobes prior to the ocean-surface peak response is about -48 dB. Figure 3.30(a) is an image over the Greenland

ice sheet after pulse compression. The surface is labeled zero depth and the bed at depth around 1.25km is detected. Figure 3.30(b) is the image after SAR processing which shows the ice bed is focused and the SNR is improved. Figure 3.30(c) is the A-scope at the along-track index of 350 in the SAR image. The A-scope shows the noise floor is at about -95 dB and the sidelobes prior to the ice surface peak response are about -49 dB.

Chapter 4: Data Preconditioning

This chapter discusses three data preconditioning steps for reducing system and radio frequency interference (RFI) effects to maximize gains from pulse compression, SAR, array processing and clutter rejection. These steps include reference function calibration, channel equalization and RFI reduction. Because the data collected by MCRDS P-3 from 2007 campaign in Greenland were degraded by RFI, the focus of this chapter is to describe the RFI suppression algorithm with array processing that was used and proved to be successful in resolving the problem.

4.1 Reference Function Calibration

The linear chirp waveforms designed in Chapter 3 are used as the reference function of the match filter in pulse compression. It has been theoretically proven and is well known that match filter maximizes the output peak SNR if the noise is white noise [41]. However the magnitude and phase of the designed waveforms may experience distortions at every stage of a radar system from waveform generation to data acquisition. The distortions may be caused by the instability of the local oscillator, the nonlinearities of the mixers and the bandpass filter and the impedance mismatch of the antenna. The distortions can be reduced to minimum by elaborate system design, but they are not avoidable. As a result of the system effect the peak SNR cannot be maximized because the ideal reference function is “mismatched” with the received signals. Therefore, there is a need to use modified reference functions

that include the system effects so that a "matched" filtering is enforced in pulse compression to maximize the SNR. This is called the reference function calibration.

The system loopback measurements are used to derive the calibrated reference functions. The so-called loopback setup of a radar system connects the transmitter and receiver with a delay line. Attenuators are used in the setup to reduce the high transmit power and protect the very sensitive receiver. Therefore the recorded waveform includes not only the system effects, but also the effects of delay line, attenuators and any other components used in the setup. The effects of the components used in the loopback setup but not in the real radar operation have to be removed from the measurements to get the system effects. This is done in frequency domain. The transfer function of each component is measured with network analyzer. Since the transfer function of the total loop measurements is the product of the system transfer function and the transfer function of each extra component, the system transfer function is derived by dividing the loop measurements by each component's measurement. The described calibration is required for each channel. The calibration setup for MCRDS Twin Otter is given in [17]. A detail description of the similar calibration procedures for another ground-based radar is given in [12]. The calibration of MCRDS P-3 is documented in [34].

The SNR gain from the above reference function calibration is quantified by calculating the SNR difference at ice bed between two radar echograms. The first

radar echogram is from compressing the radar data with ideal reference function and the other uses the calibrated reference function.

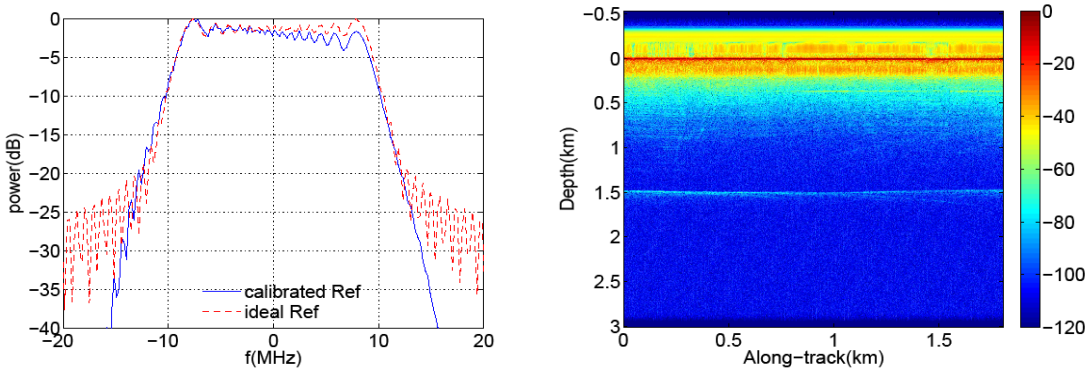

(a) (b)

Figure 4.1: (a) Spectrum of Ideal and Calibrated Reference Functions of MCRDS Twin Otter 3-us Waveform; (b) Radar Echogram from Calibrated Reference Function

Figure 4.1(a) shows the spectrum difference between the ideal 3us waveform and the calibrated waveform of channel 1 of MCRDS Twin Otter. The red-dash line is the spectrum of the ideal waveform and the blue-solid one is the spectrum of the real waveform with the system effects. It is observed that the real signal magnitude is not constant because of the system effects. The spectrum of the 10us waveform has similar distortion. Figure 4.1(b) is the radar echogram from compressing the low-gain data of file 20060527b_80 with the calibrated reference function. For this case, the depth of ice bed is around 1.5km. With five channels uniformly combined, the average SNR at ice bed is 24.55dB and 25.10dB from ideal and the calibrated reference functions. Therefore the reference function calibration gain is 0.55dB. For the high gain data of the same file, with five channels uniformly combined, the

average SNR at ice bed is 34.08dB and 35.18dB from ideal and the calibrated reference functions. The SNR gain from reference calibration is 1.10dB. Although the gain seems small big, every half dB is important in detecting very weak signals like the ones from the deepest ice bed of Jakobshavn glacier.

4.2 Channel Equalization

For a radar system with antenna array of separated channels, each channel cannot be made exactly the same in reality. The channel mismatches in amplitude and phase have to be compensated to achieve the best possible gain from array processing. The compensation for channel mismatches before array processing is called channel equalization. Array processing has two major applications in ice depth sounding: (1) to combine the data from each channel in a way that the weakest nadir echoes from deep ice bed are maximized; (2) to form a receiving beam pattern that has the main beam in the direction of nadir and nulls in the directions of undesired signals like RFI and surface clutter. In the first application, the level of sidelobes is not a major concern and uniform weights can be used to obtain the maximal nadir response because the data from all channels are coherently added if all channels are matched and the plane of the array is horizontal. Therefore to maximize the nadir signal, not only do the channels have to be equalized but the aircraft wing angle and roll also have to be compensated. In the second application, channel mismatches will alter the array response, null location and depth and thus degrade the beamforming performance. Channel mismatches can be the angle of arrival (AOA) independent and

AOA dependent [42]. The former is usually stationary and due to the differences between transfer functions of each receiver channel. The later is random and may be due to mutual coupling, near-field scattering and multipath effects, element position errors (wing flexure for airborne radar), or bandwidth dispersion, etc.

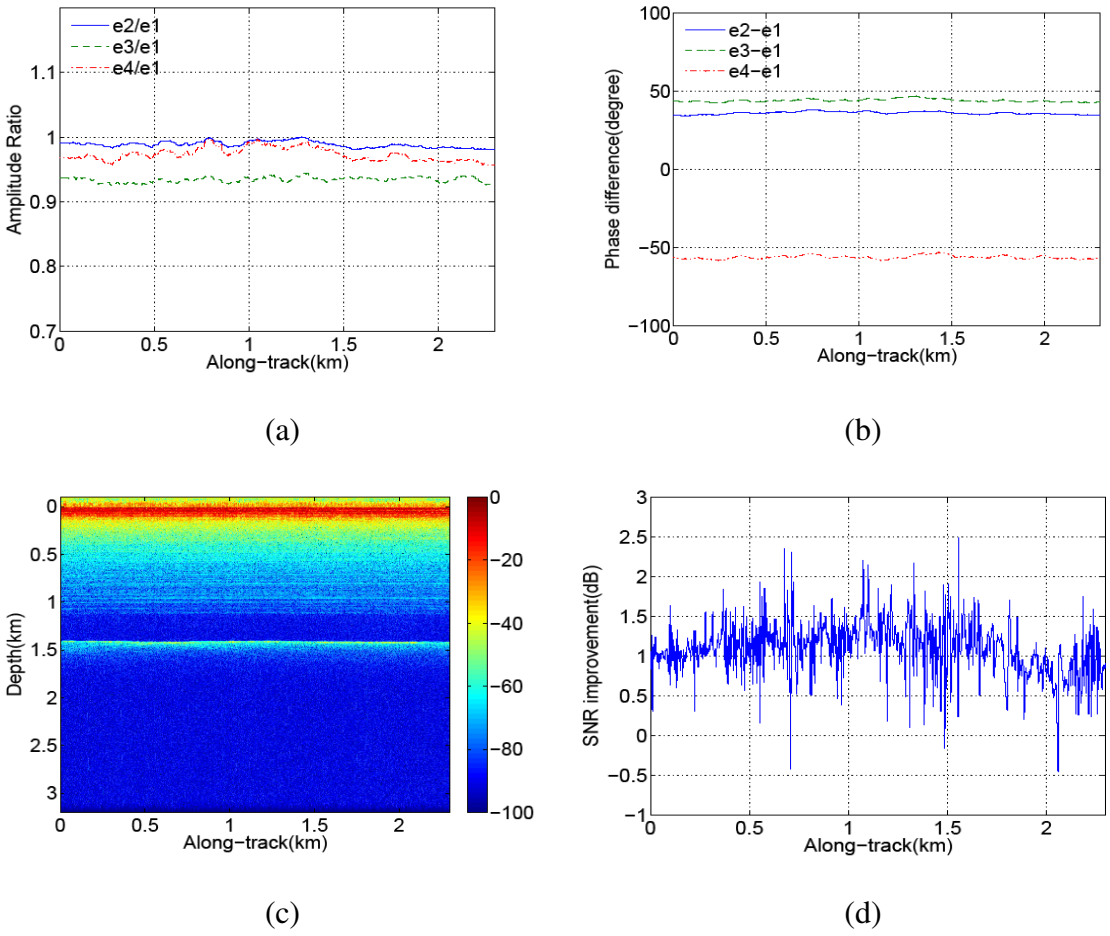

Figure 4.2: Ice Bed SNR Improvement from Channel Equalization

Figure 4.2 presents an example that illustrates how constant amplitude and phase mismatches are estimated and compensated to improve the SNR of ice bed. The

low gain data of the 8th file on September 17, 2007 are used in the calculation. The amplitude and phase mismatch between the four channels are estimated by comparing the amplitudes and phases of the ice surface echoes which are determined by looking for the peaks of every A-scope. The first element is used as the reference for computing the mismatches between channels. A moving average window of 100 records is applied to smooth out the high frequency random variations, so what remains in the estimates are the stationary channel mismatches. Amplitude mismatches are obtained by directly computing the peak magnitude ratios between channels and the phase mismatches are obtained by computing the phase differences between channels taking out the effects of aircraft roll and wing angle. Figure 4.2(a) and (b) display the estimated amplitude and phase mismatches over a distance of about 2.8 km. The mismatches are basically constant although there are some slow variations. On average, the amplitude mismatches are 0.9887, 0.9342 and 0.9734 in terms of magnitude ratio between channel two and one, three and one, and four and one. The corresponding phase mismatches are 35.96°, 43.96° and -56.21°. This amount of amplitude and phase mismatches would result in a loss of 2.37dB in ice bed SNR when the conventional beamforming is performed with the looking direction be the nadir. Figure 4.2(c) is the radar echogram after beamforming with channel equalization. The ice bed is close to 1.5 km in this case. The ice bed SNR is computed and compared with the one without channel equalization. The difference is the SNR improvement from channel equalization which is shown in Figure 4.2(d). It turns out the improvement is 1.09dB on average.

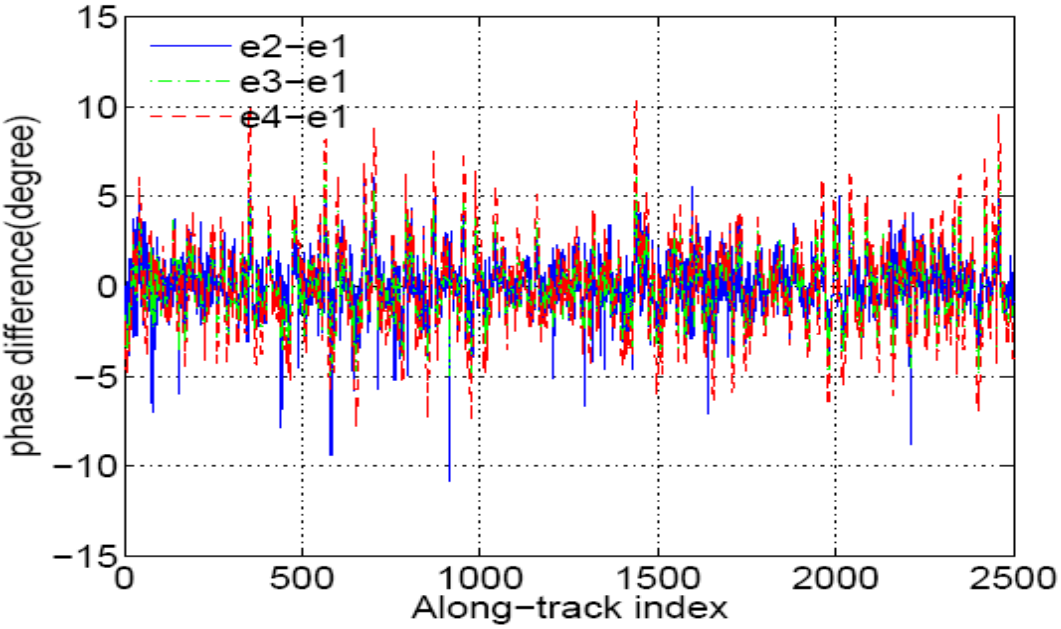

(a)

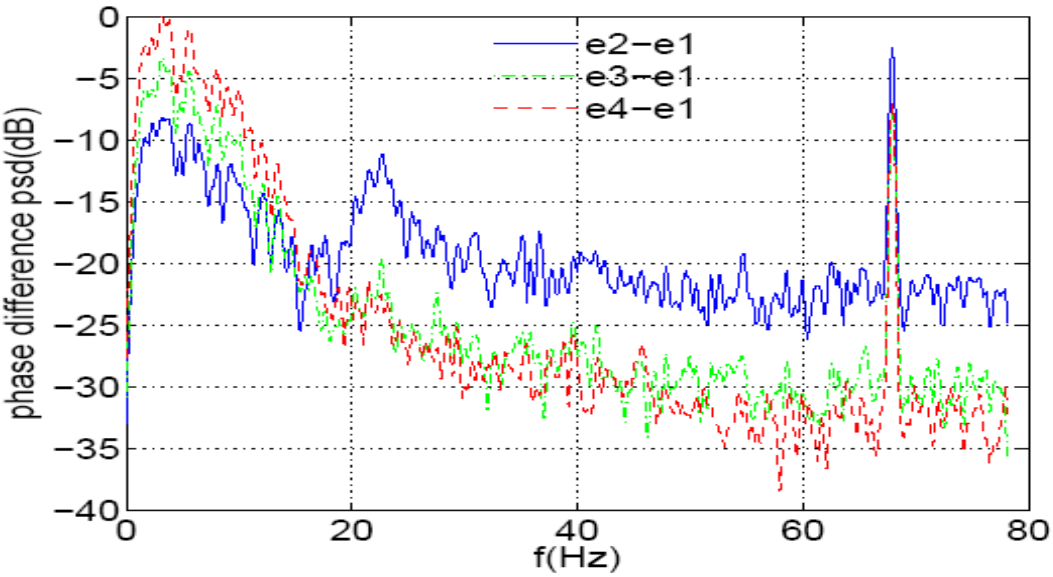

(b)

Figure 4.3: (a) Random Phase Mismatches and (b) the PSD

Random mismatches between channels have been observed in MCRDS P-3 data with strong echoes either from ocean surface, smooth ice surface, or the bed. Figure 4.3 shows an example of analysis using echoes from the smooth ice surface of data file 550 on September 17, 2007. Figure 4.3(a) is the random phase differences between all other channels and channel one. The average phase mismatches have been removed from the plot. The variations are between -10 degrees and 10 degrees. Figure 4.3(b) is the corresponding power spectral density of the phase differences, which indicates significant variations occur at 3.2 Hz, 5.6Hz, 8.1Hz and 67.9Hz.

The random amplitude and phase mismatch effects on null location and depth are critical and can be studied by Monte Carlo simulation. Figure 4.4 shows the simulation results for MCRDS P3 from 1000 runs. Figure 4.4(a) and (b) display respectively the null location and depth variations (1σ) from1% (1σ) amplitude mismatch. The horizontal axis of the plots is the null location in terms of the angle away from nadir. The simulation covers $50^\circ \sim 85^\circ$ at step of1°. According to Figure 4.4(a), for example, if a null is intended to be placed at70°, the actual null locations will be around 70° with a standard deviation of 3° because of the1% amplitude mismatch. Also the depth of the null is not infinite and has a variation of about 9.5dB around its mean as shown in Figure 4.4(b). Similarly Figure 4.4(c) and (d) display respectively the null location and depth variations (1σ) from1°(1σ) phase mismatch. According to Figure 4.4(c) and (d), the standard deviation of the null location at70° is about 6.2° and the null depth variation is 9.5dB.

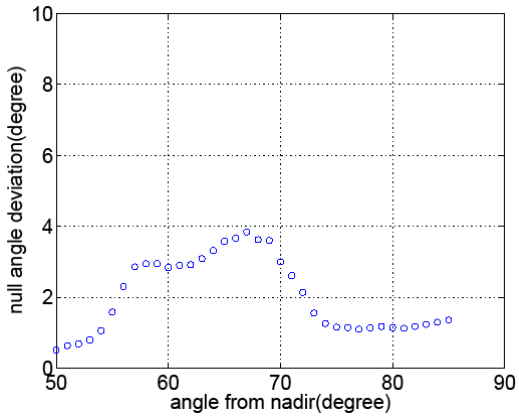

(a)

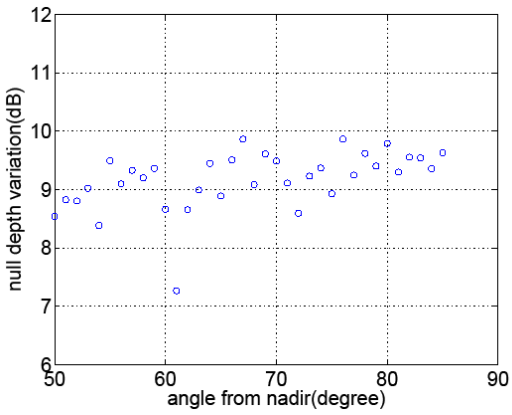

(b)

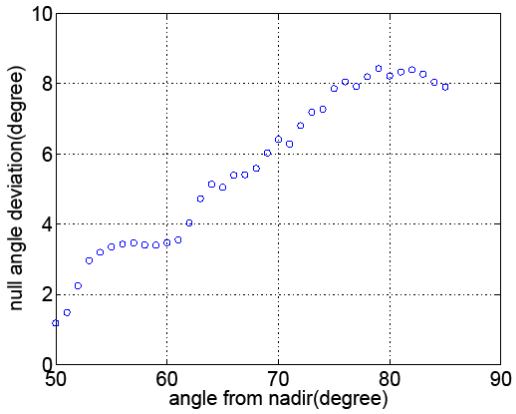

(c)

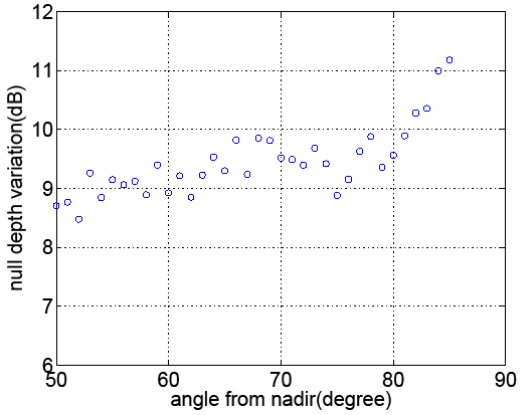

(d)

Figure 4.4: Monte Carlo Simulation of Amplitude and Phase Mismatches

4.3 RFI Suppression

4.3.1 Introduction

Radio frequency interferences are always a possible problem for radar systems operating in VHF/UHF bands because these frequencies are also widely used by television, radio and wireless communications for many civilian and military applications. Signals from these emitter sources are referenced as RFI because they contaminate the spectrum of desired signals. In order to understand the RFI environment encountered by VHF/UFH radar systems, surveys were performed by Grumman E-2C throughout the world to characterize RF interferers in terms of the density of the interference emitters, the type of emitters, their effective radiated power, their modulation bandwidth, duty factor and their temporal dependence. It is found that even in remote locations the average interference power often exceeds receiver noise by many dB [43]. RFI may also come from other electronic systems that work together with the radar system, like the laser altimeter working together with the CReSIS radar systems. Furthermore, any hardware design flaws or improper operation of the radar will introduce RFI internally.

In order to identify the RFI problem the MCRDS P-3 encountered in 2007 field campaign, measurements were taken with the system in different listening modes (the radar does not transmit signals and only receives signals from the

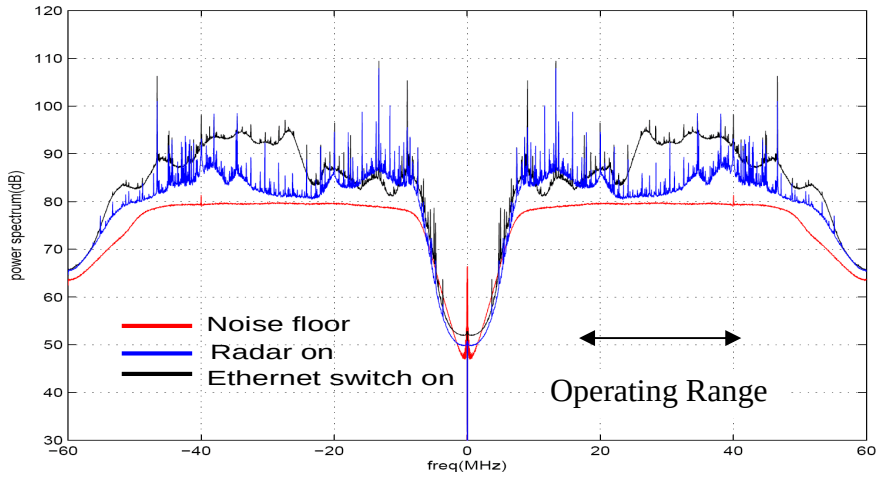

Figure 4.5: Contaminated Spectrum by RFI

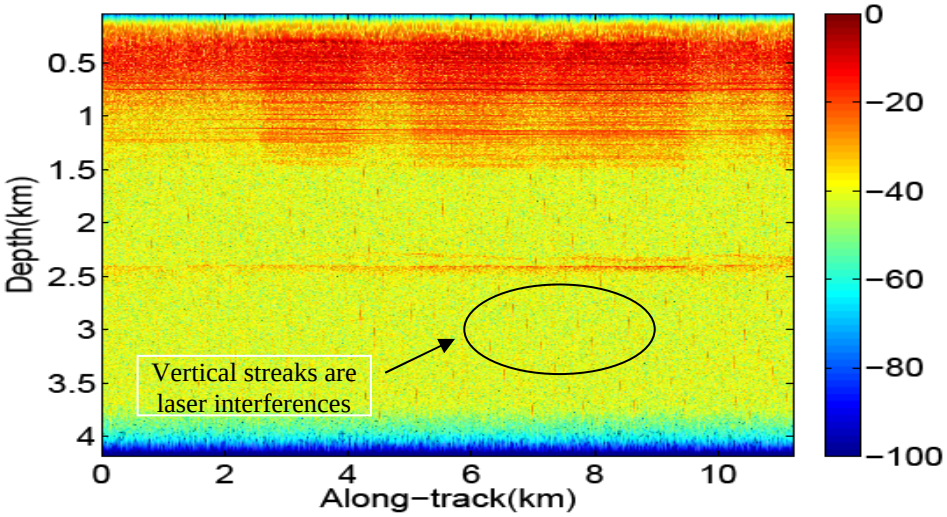

Figure 4.6: Degraded Radar Echogram by RFI

environment) in a SPRINT anechoic chamber in October 2007. Figure 4.5 is the measured signal power spectrums. The bottom plot in red line is the flat spectrum of system noise, measured with no antenna connected. The middle one in blue line was measured with antenna connected. In the operating frequency band, the spectrum is

not as ideal as flat and has many spikes. The spectrum distortion was cause by the system's own radiation. Because of the space limit of the anechoic chamber, the antenna distance was less than 1.5 meters apart from the antenna. In real operation, the system is farther away from the antenna, this system's own radiation effect would be less severe. The top spectrum was measured with emulating the improper use of an Ethernet cable to download data from the radar computer to an external computer in the field campaign. The contaminated spectrum shows the Ethernet interference degrade the radar performance by 15dB. Figure 4.6 is a radar echogram from the data collected by MCRDS P-3 radar in the campaign. It is observed that the radar sensitivity and image quality are severely degraded by the laser and Ethernet interferences. The vertical short streaks in the figure are the interference signals from the laser altimeter in operation. There are similar laser interferences in MCRDS Twin Otter data 2006.

As shown by the above example, the RFI can severely reduce the system sensitivity and degrade the quality of radar images. Therefore, a lot of effort has been made to investigate effective means of suppressing RFI to alleviate its impacts on radar imagery. The RFI suppression technique developed by Grumman is based on least-mean-square (LMS) estimation theory. It utilizes a single transversal filter with multiple taps to achieve both interference suppression and equalization needed to overcome the distortions caused by notching function [44]. The advantages of stepped-frequency waveforms are exploited to avoid spectral regions that are heavily

contaminated with RFI [45]. A least-mean-square filter is applied to suppress narrow-band RFI in wideband radar signals and is tested with data collected in the JPL P-band TopSAR (Synthetic Aperture Radar) program in different noisy environments [46]. A frequency-domain version of LMS filter is implemented to remove slowly-varying narrowband RFI in the experimental data collected by CARABAS, a Swedish airborne UWB SAR system operating in the 20-90MHz band [47]. Compared to LMS filters in time domain, LMS filters in frequency domain are more computationally efficient. Reference [44] proposes an RFI algorithm that makes use of prior information of interferences. The interferences with fixed frequencies and changing frequencies are addressed accordingly. The performance of the algorithm is demonstrated with the data collected by the Army Research Laboratory's UWB Rail SAR. While most RFI suppression methods mainly deal with amplitude images, phase information has to be preserved for interferometric applications. Reference [48] proposes a phase preserving RFI suppression algorithm assuming interferences are a sum of many sinusoidal tones. For SAR systems with array, in addition to time domain and frequency domain information, spatial information provides additional means for RFI suppression as long as the directions of interferences are not the same as the desired signals. Reference [49] presents an adaptive beamforming algorithm of RFI suppression with an experimental eight-elemental array. A brief review of the approaches to RFI suppression for VHF/UHF SAR systems is presented in [50].

4.3.2 Algorithms of RFI Suppression

According to review of the literature, the existing algorithms to suppress RFI may be classified into three categories: (1) model-based; (2) filters; and (3) array processing.

(1) Model-based Approaches

Figure 4.7 shows the basic principle of model-based methods. A model is used to describe the characteristics of RFI based on prior knowledge of RFI. The model estimates the RFI based on the input signal plus RFI and the estimate of RFI is subtracted from the data.

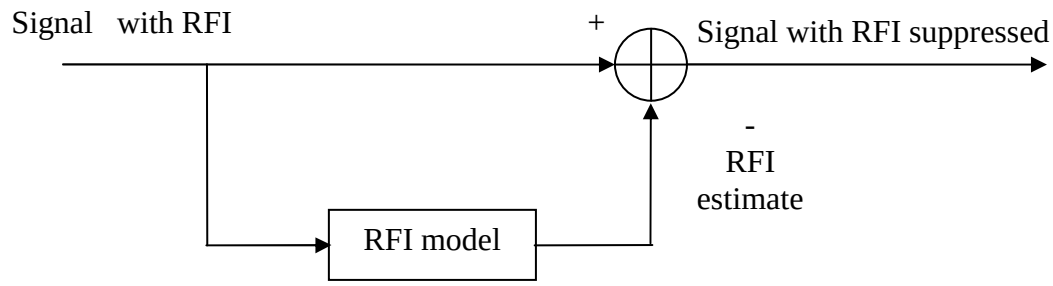

Figure 4.7: Diagram of Model-Based Methods

A commonly used RFI model assumes interference signals are a sum of sinusoids. The received signal is written as

$$x(t) = s(t) + n(t) + \sum_{i=1}^{N} A_i \sin(2\pi f_i t + \phi_i) \tag{4.1}$$

where $s(t)$ is the target return, $n(t)$ is the receiver noise, N is the number of interferers, and A_i, f_i, ϕ_i are the amplitude, frequency, and phase of each sinusoid. In order to estimate the model parameters, the target signal needs to be subtracted from the received signal; otherwise biases in the estimate caused by target signal will degrade the RFI suppression performance. One method to avoid this problem is to use listening mode to collect data for RFI estimation. Another method is to increase the recording length of each pulse so that a portion at the end of each record without target signals can be used for RFI estimation. The standard linear least-mean-square estimation method or maximum-likelihood estimation method can be used to estimate the RFI parameters [44,51]. An iterative procedure can also be implemented to remove interferers one by one in order of their power level. For a small number of static interferers at fixed frequencies, this approach is very effective and the performance is excellent in terms of good interference suppression and little signal distortion.

The target signal, receiver noise and RFI can also be modeled with an autoregressive process:

$$x(j) = -\sum_{k=1}^{N} a(k)x(j-k) + n(j) \tag{4.2}$$

where $x(j)$ is the received sample at time j, $a(k)$ are a set of coefficients of the AP process need to be estimated, and $n(j)$ is white noise. According to [15], the

performance of this approach is comparable to the approach based on the model by equation (4.1).

(2) Filter Approaches

Notch filters and adaptive filters are two kinds of filters that have been used to suppress RFI [45, 46 and 52]. The concept of notch filter method is very straightforward. The spectrum of contaminated signals is examined to identify the interference spikes as those illustrated in Figure 4.6. Then notch filters are designed and applied to remove these spikes in frequency domain. Notch filters work well for fixed narrow band RFI and a small number of interferers. In order to identify the interference spikes, an average spectrum of a number of records needs to be estimated. Lord [45] used median filters to smooth the averaged spectrum to obtain an estimate of target signal envelope and subtract the estimated signal from the average spectrum. The RFI spikes above a certain level of the target signal envelope are identified. One major artifact of notch filters is the loss of signal integrity, which can be recovered in some cases through interpolation.

Adaptive filters have been more widely used compared to notch filters because little prior knowledge about RFI is required, and variations of RFI can be adaptively tracked by automatically adjusting their own parameters [43, 45-47 and 53-55]. LMS adaptive filters are the most common because of their good performance and convenient implementation. Figure 4.8 shows the block diagram of a LMS

adaptive filter implemented in time domain, which is described by recursive equations (4.3) ~ (4.8).

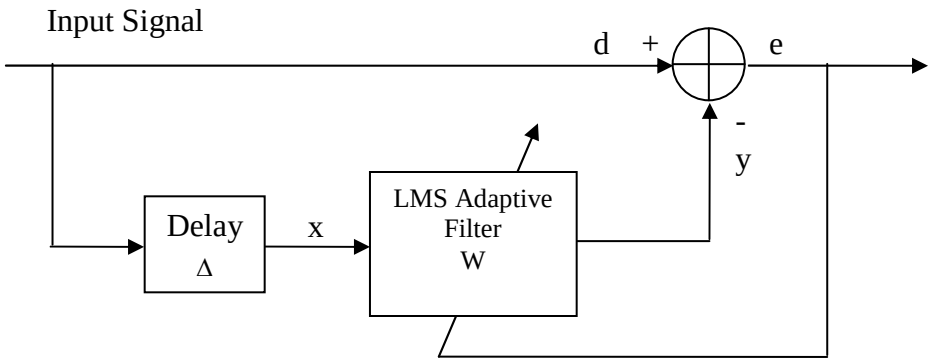

Figure 4.8: Diagram of a LMS Adaptive Filter in Time Domain

For a filter length of n, the input signal vector D and the weight vector W at time j are defined by equations (4.3) and (4.4):

$$D_j = \{d(j), d(j-1), d(j-2), ..., d(j-n+1)\} \tag{4.3}$$

$$W_j = \{w_0(j), w_1(j), w_2(j), ..., w_n(j)\} \tag{4.4}$$

The input X_j to the adaptive filter is a delayed version of the input signal:

$$X_j = D_{j-\Delta} \tag{4.5}$$

The output of the adaptive filter $y(j)$ is an estimate of RFI and is equal to the inner product of the weight and input vectors:

$$y(j) = W_j \cdot X_j^T \tag{4.6}$$

The error signal $e(j)$ is the desired signal with RFI cleaned:

$$e(j) = d(j) - y(j) = d(j) - W_j \cdot X_j^T \tag{4.7}$$

And the weights are updated by minimizing the mean square of $e(j)$:

$$W_{j+1} = W_j + 2\mu \ e(j) X_j^* \tag{4.8}$$

where μ is the step size and X_j^* is the conjugate of X_j.

In the above implementation, three filter parameters, the delay Δ, the step size μ, and the number of weights have to be optimized to get the best performance. Sidelobes are an undesired outcome of filters used for RFI suppression. The filter performance can be evaluated by range compressing the output and measuring the target mainlobe width, the peak sidelobe ratio (PSLR), and the integrated sidelobe ratio (ISLR). Lord [45] discussed the methods to determine the optimal parameters and procedures to improve the filter's performance. In order to reduce the sidelobes caused by the filter, the filter was swept from both ends of the input data and the two filter outputs were averaged. The input data were zero padded to minimize the filter edge effects.

The time domain version of the LMS adaptive filer has been implemented and simulated. Figure 4.9 and Figure 4.10 show a sample result. In the simulation, a chirp of 20 MHz bandwidth was mixed with 6 sinusoid interferences. The interference-to-signal ratios were 30~40 dB as shown by Figure 4.9. Figure 4.10 shows the interferences were notched out by the filter.

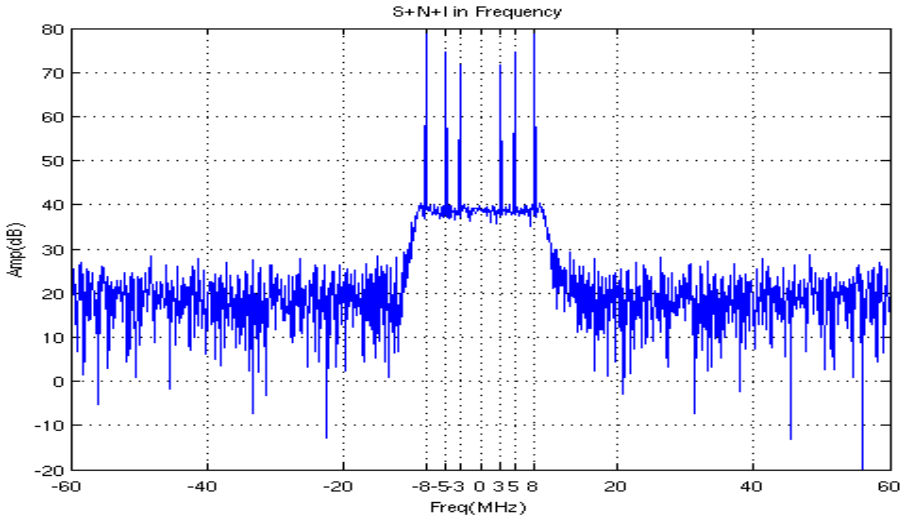

Figure 4.9: Spectrum of Signal with Interferences

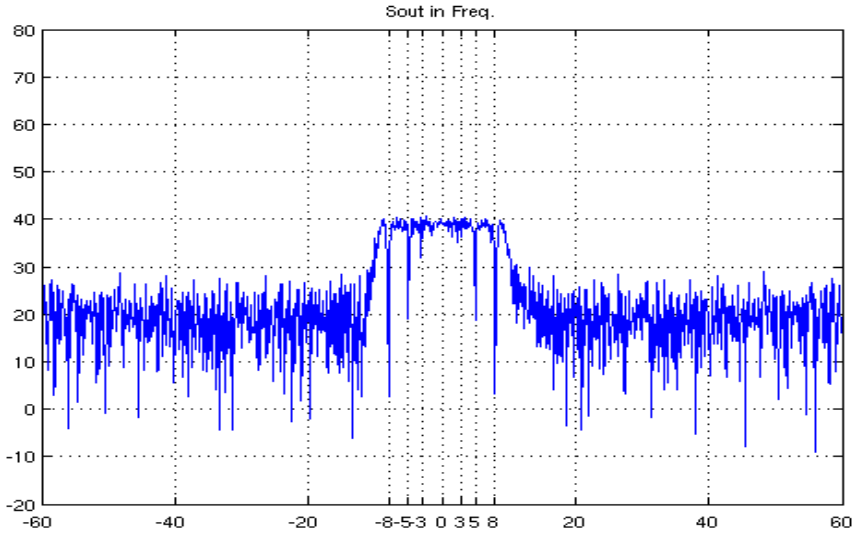

Figure 4.10: Spectrum of Signal with Interference Suppressed

(3) Array Processing Approaches

Array processing has found widespread application in radar, sonar, communications, seismology, diagnostic ultrasound, and multi-channel audio systems

[56]. For SAR systems with an array, in addition to time domain and frequency domain information, spatial information provides additional means for RFI suppression as long as the directions of interferences are not the same as the desired signals. By combining signals received by each element of array, signals from a certain direction can be enhanced and signals from RFI directions can be rejected. This is actually a spatial filtering process, which is usually known as beamforming.

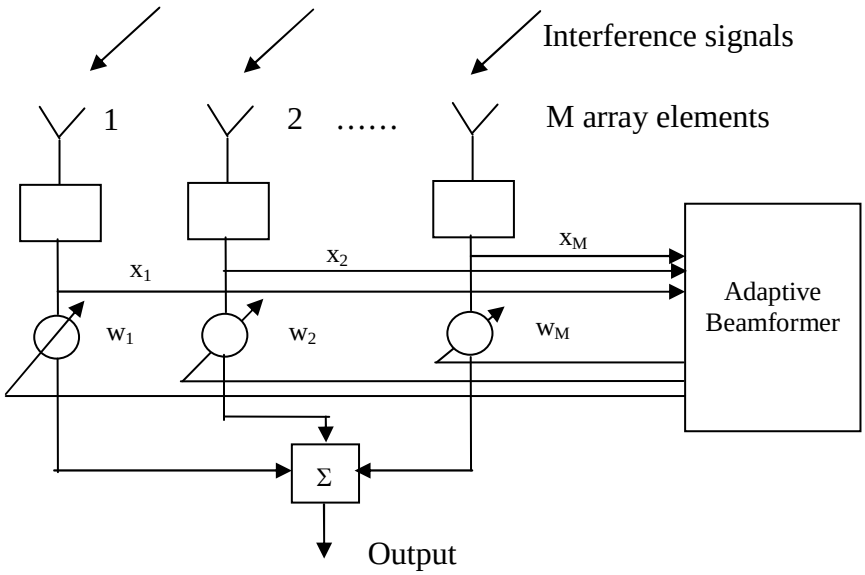

Figure 4.11: Diagram of an MVDR Adaptive Beamformer

Figure 4.11 shows an LMS adaptive filter implemented in spatial domain, usually called MVDR adaptive beamformer, described by equations (4.9)~(4.14). For an array of M elements, the input signal vector X at time j is defined by equations (4.9):

$$X_j = \{x_1(j), x_2(j), x_3(j), ..., x_M(j)\} \tag{4.9}$$

And the weight vector W is

$$W = \{w_1, w_2, w_3, ..., w_M\} \tag{4.10}$$

The output of the adaptive beamformer is

$$y(j) = \sum_{i=1}^{M} x_i(j) w_i \tag{4.11}$$

By minimizing the mean square of the output with the linear constraint

$$W^H S(\theta_0) = g \tag{4.12}$$

the optimal weights are obtained:

$$W = \frac{g^* R^{-1} S(\theta_0)}{S^H(\theta_0) R^{-1} S(\theta_0)} \tag{4.13}$$

where θ_0 is the direction of arrival, $S(\theta_0)$ is the beam steering vector

$$S(\theta_0) = [1, e^{j\theta_0}, ..., e^{j(M-1)\theta_0}] \tag{4.14}$$

g is a complex gain and R is the $M \times M$ correlation matrix. For MVDR adaptive beamformer g is equal to 1.

MVDR algorithm is known as FMV algorithm when it is applied to data in frequency domain. Figure 4.12 is the implementation of FMV algorithm based on reference [57]. This implementation first estimates the steering vector in frequency domain by eigenvalues decomposition of the averaged correlation matrix from multiple snapshots of ice surface or bottom. This part is similar to MUSIC algorithm. Each array snapshot is divided into blocks of some finite length of L_{blk}, and FFT is

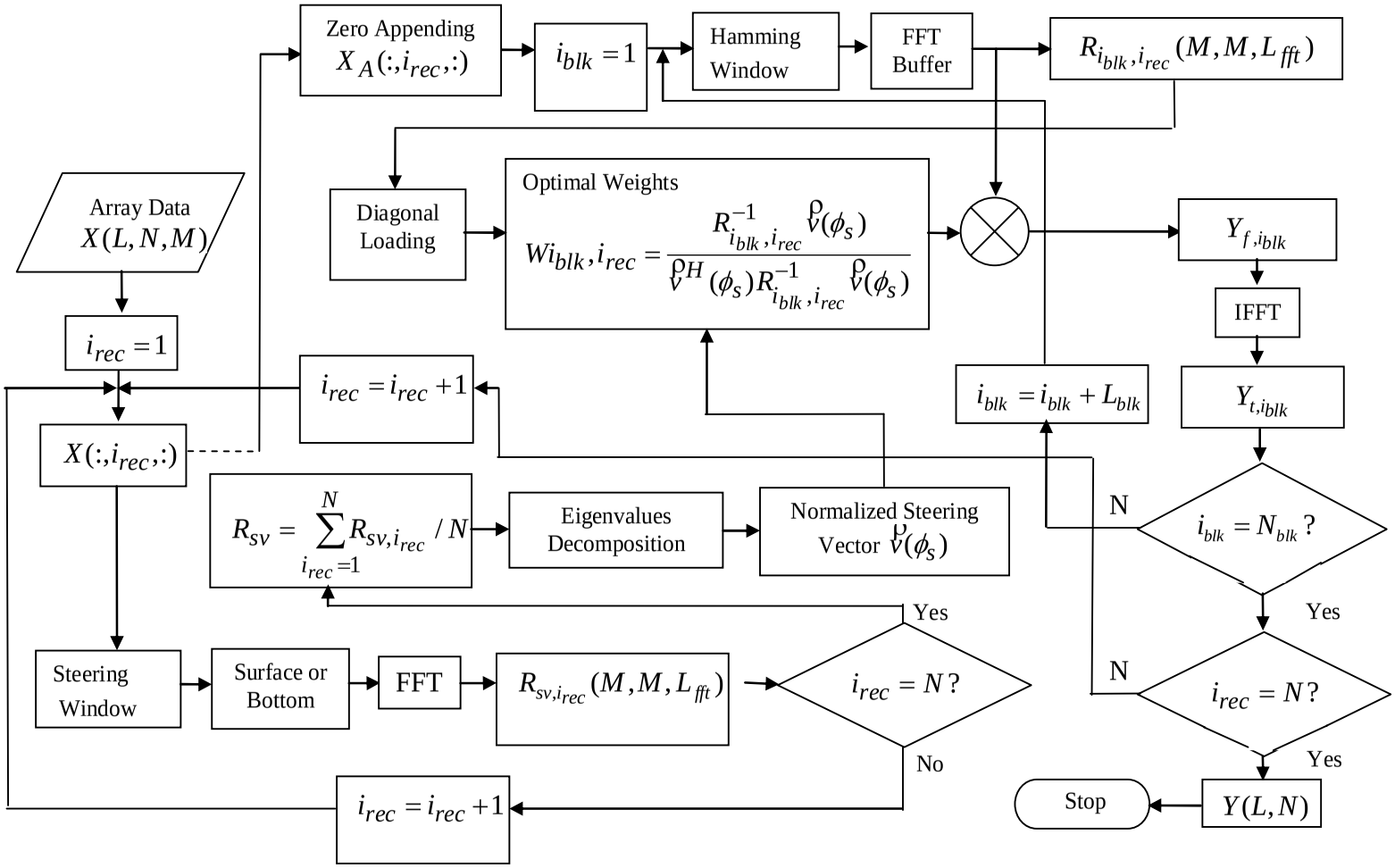

Figure 4.12: Implementation of FMV

carried out over a bigger length of L_{fft}. Correlation matrix is computed in frequency domain over a length of L_{corr}. Hamming window of length L_{ham} is applied in time domain to reduce the circular convolution effects of FFT. The FFT and correlation matrix are computed with a moving window of the block length. The MVDR optimal weights are then calculated for each frequency bin of each block with the steering vector and the corresponding correlation matrix. The output is obtained by multiplying the optimal weights with the array data in frequency domain. Finally the output in time domain is obtained by taking the inverse FFT of the output in frequency domain. The variables and some implementation details in the flow diagram are explained as follows:

1) $X(L, N, M)$, the recorded array data matrix.

L is the length of each snapshot, N is the number of snapshots and M is the number of array element.

2) Steering window

$$w_{sw} = \sin[n\pi/(L_{sv}+1)],\ n = 1,2,...,L_{sv} \tag{4.15}$$

where $L_{sv} = L_2 - L_1 + 1$ is the steering window length. If the index of the surface or bottom is $i_{local-\max}$, then

$$L_1 = i_{local-\max} - (L_{sv} - 1)/2 \tag{4.16}$$

$$L_2 = i_{local-\max} + (L_{sv} - 1)/2 \tag{4.17}$$

3) $R_{sv,i_{rec}}(M,M,L_{fft})$, the correlation matrix of surface or bottom echo of each snapshot.

$$R_{sv,i_{rec}}(M,M,L_{fft}) = [\,fft(X(L_1:L_2,i_{rec},M),L_{fft},1)]^H[\,fft(X(L_1:L_2,i_{rec},M),L_{fft},1)] \tag{4.18}$$

4) R_{sv}, the average correlation matrix from N snapshots.

$$R_{sv} = \sum_{i_{rec}=1}^{N} R_{sv,i_{rec}} / N \tag{4.19}$$

where i_{rec} is the index of snapshots.

5) Eigenvalues decomposition for each frequency bin

$$R_{sv} = \sum_{m=1}^{M} \lambda_m \mathbf{q}_m \mathbf{q}_m^H = Q\Lambda Q^H \tag{4.20}$$

where λ_m is the eigenvalue of R_{sv} in descending order, that is, $\lambda_1 \geq \lambda_2 \geq ... \geq \lambda_M$; $\mathbf{q}_m$ is the corresponding eigenvector; Λ is a diagonal matrix with the eigenvalues in descending order on the diagonal, and

$$Q = [\mathbf{q}_1\ \mathbf{q}_2 ... \mathbf{q}_M\ ] \tag{4.21}$$

6) Normalized steering vector

$$\underset{v}{\rho}(\phi_s) = \mathbf{q}_1 / q_{1-ref} \tag{4.22}$$

where q_{1-ref} is the component of the reference element in $\mathbf{q}_1$ and ϕ_s is the direction of arrival angle.

7) $X_A(L_A, N, M)$, the aero-appended array data matrix. L_A is the length of extended snapshot.

$$\begin{aligned} &X(L_A, N, M) \\ &= [zeros(L_{corr} + L_{blk} + L_{fft}, N, M); X(L, N, M); \\ &zeros((L_{corr} + L_{blk} + L_{fft})/2, N, M)] \end{aligned} \tag{4.23}$$

where $L_A = L + (L_{corr} + L_{blk} + L_{fft}) + (L_{corr} + L_{blk} + L_{fft})/2$; L_{corr}, the length of buffer for running average correlation matrix computation; L_{blk}, the Length of blocks in a snapshot ; L_{fft}, the length of FFT

8) Hamming window

$$w_{ham} = [\text{zeros}(\frac{L_{fft} - L_{ham}}{2}, 1); \text{hamming}(L_{ham}) \tag{4.24}$$

$$\text{zeros}(\frac{L_{fft} - L_{ham}}{2}, 1)]/\max(\text{hamming}(L_{ham})) \tag{4.25}$$

where $L_{ham} = L_{fft}/2$

9) Recursively update running correlation matrix for each frequency bin

$$R_{i_{blk}, i_{rec}}(M, M, L_{fft}) = R_{i_{blk}, i_{rec}}(M, M, L_{fft}) + (B_{in}^H B_{in} - B_{out}^H B_{out}) \tag{4.26}$$

where $B_{in} = fft(w_{ham} .* X_A(i_{blk} + L_{corr} + L_{blk} : i_{blk} + L_{corr} + L_{blk} + L_{fft} - 1, i_{rec,} :))$ is the data goes into the FFT buffer; and

$$B_{out} = fft(w_{ham} .* X_A(i_{blk} : i_{blk} + L_{fft} - 1, i_{rec,} :)) \tag{4.27}$$

is the data exit the FFT buffer; and $R_{i_{blk},i_{rec}}(M,M,L_{fft})$ is initially set to zero.

10) Diagonal loading

$$R_{i_{blk},i_{rec}}(M,M,L_{fft}) = R_{i_{blk},i_{rec}}(M,M,L_{fft}) + [\max(R_{i_{blk},i_{rec}}(M,M,L_{fft}))\, f_{dl} + \varepsilon]I \tag{4.28}$$

where f_{dl} is the diagonal loading factor, ε is the damping factor for recursive computation and I is a diagonal unit matrix.

11) Optimal weights for each frequency bin

$$Wi_{blk},i_{rec} = \frac{R^{-1}_{i_{blk},i_{rec}} \overset{\rho}{V}(\phi_S)}{\overset{\rho}{V}^H(\phi_S) R^{-1}_{i_{blk},i_{rec}} \overset{\rho}{V}(\phi_S)} \tag{4.29}$$

12) $Y_{f,i_{blk}}$, the output in frequency domain

$$Y_{f,i_{blk}} = B_m W^*_{i_{blk},i_{rec}} \tag{4.30}$$

where

$$B_m = fft(w_{ham}.* X_A(i_{blk} + L_{corr}/2 + L_{blk} : i_{blk} + L_{corr}/2 + L_{blk} + L_{fft} - 1, i_{rec,} :)) \tag{4.31}$$

13) $Y_{t,i_{blk}}$, the output in time domain

$$Y_{t,i_{blk}}(i_{blk} + \frac{L_{corr} + L_{fft} + L_{blk}}{2} : i_{blk} + \frac{L_{corr} + L_{fft} + L_{blk}}{2} + L_{blk} - 1)$$

$$= \text{ifft}(Y_{t,i_{blk}})(\frac{L_{fft} - L_{blk}}{2} + 1 : \frac{L_{fft} + L_{blk}}{2}) / w_{ham}(\frac{L_{fft} - L_{blk}}{2} + 1 : \frac{L_{fft} + L_{blk}}{2}) \tag{4.32}$$

14) N_{blk}, the length of data block

$$N_{blk} = L + (L_{corr} + L_{fft} + L_{blk})/2 \tag{4.33}$$

15) $Y(L, N)$, the combined output in time domain with the same length of the original snapshots.

$$Y(L, N) = Y_t(L_{corr} + L_{blk} + L_{fft} + 1 : L_{corr} + L_{blk} + L_{fft} + L, N) \tag{4.31}$$

4.3.3 Results

The above implemented FMV algorithm is applied to ice data collected in 2007 by MCRDS P-3 that are contaminated by laser-altimeter signals and the Ethernet cable used to transfer data from the radar to an external computer. The parameter values are:

$L_{fft} = 512$, $L_{blk} = L_{fft}/4$, $L_{ham} = L_{fft}/2$, $L_{corr} = 4L_{fft}$, $f_{dl} = 0.1$,

$\varepsilon = 10^{-8} \max(\max(X(:, i_{rec}, :))$

Figure 4.13 (a) shows a radar SAR image with RFI; the data from the four channels are uniformly combined. Figure 4.13(b) shows the SAR after RFI suppression by the FMV algorithm. It is observed that the ice layers deeper than 2km are obviously enhanced because of the RFI suppression. Figure 4.14(a) is the A-scope comparison between uniform weighting and the adaptive beamforming by the FMV algorithm, which shows the RFI is suppressed by about 12 dB and the bottom signal peak value is not changed before and after RFI suppression. Figure 4.15 is the SAR image of about 92 km from the flight between NEEM and NGRIP on September 17,

2007. The image is degraded by RFI and some weak and deep layers are not visible because of the reduced sensitivity. Figure 4.16 is the improved SAR image after RFI suppression by the FMV algorithm. It is observed that the weak layer at depth of 1950m, which is masked by RFI in Figure 4.15, becomes visible all the way along the flight path. It is also observed that the deep layers around 2.6km, which are barely visible, are brought up clearly between 0 km and 65km.

It should be noted that there are some vertical streaks in the SAR images of Figure 4.13, 4.15 and 4.16. Along these streaks, signals of the internal layers are weaker. It is concluded after analysis that these streaks result from the ignorance of compensating the aircraft roll effects in both the uniform weighting and the FMV processing. Figure 4.14(b) plots the history of the aircraft roll that corresponds to the SAR images in Figure 4.13 to illustrate the correlation between the vertical steaks and the aircraft roll. According to Figure 4.14(b), there are roll peaks of 4.86, -4.87, 4.92,-4.92 and 5.4 degrees at along-track distances of 0.843 km, 4.4km, 6 km, 8 km and 9.85km. The streaks occur exactly at the same distances in Figure 4.13(b). The receive beam is assumed to point to nadir in both the uniform weighting and the FMV processing. However, the beam direction deviates from nadir because of the roll error and thus results in weaker backscattering. The streaks become more apparent after RFI reduction. This is because the FMV algorithm is adaptive to the random component of channel mismatch and the roll error is the dominant pointing error. So the beam points closer to nadir at small roll angles deviates more from nadir at larger

roll angles which results in more apparent streak intensity contrast. On the other hand, for the uniform weighting, the beam does not point closer to nadir at small roll angles for most time because of the random channel mismatches. Therefore the streak intensity contrast is not as obvious as the case of FMV processing.

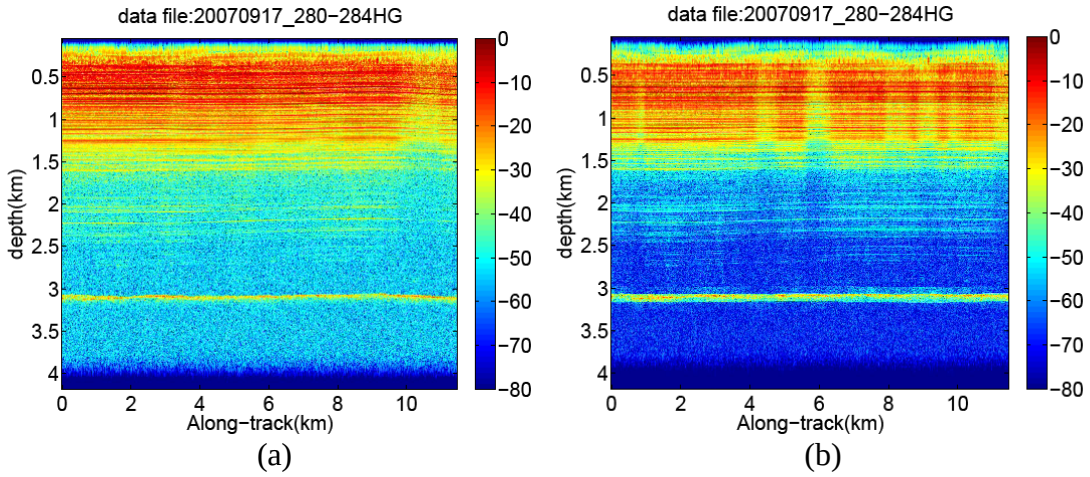

(a) (b)

Figure 4.13: (a) SAR Image with RFI; (b) SAR Image after RFI Supression

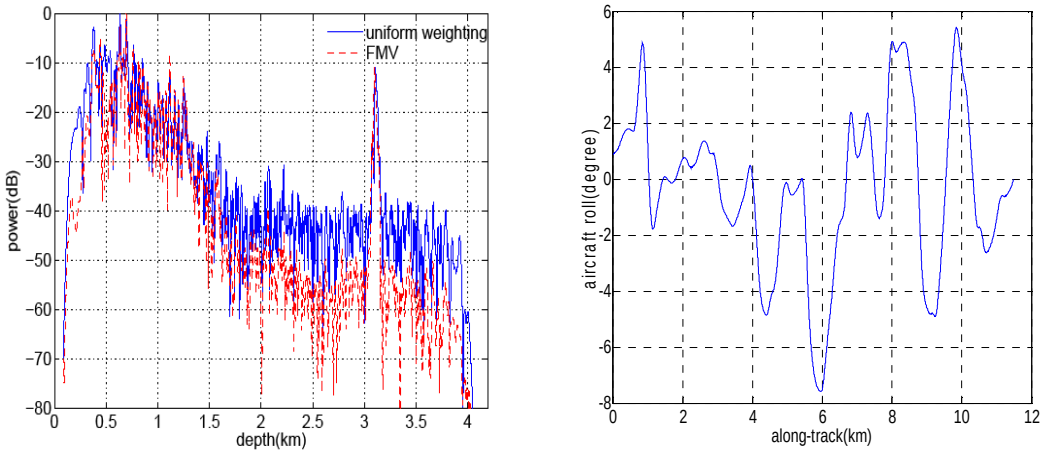

(a) (b)

Figure 4.14: (a) A-scope Comparison; (b) Aircraft Roll Angle

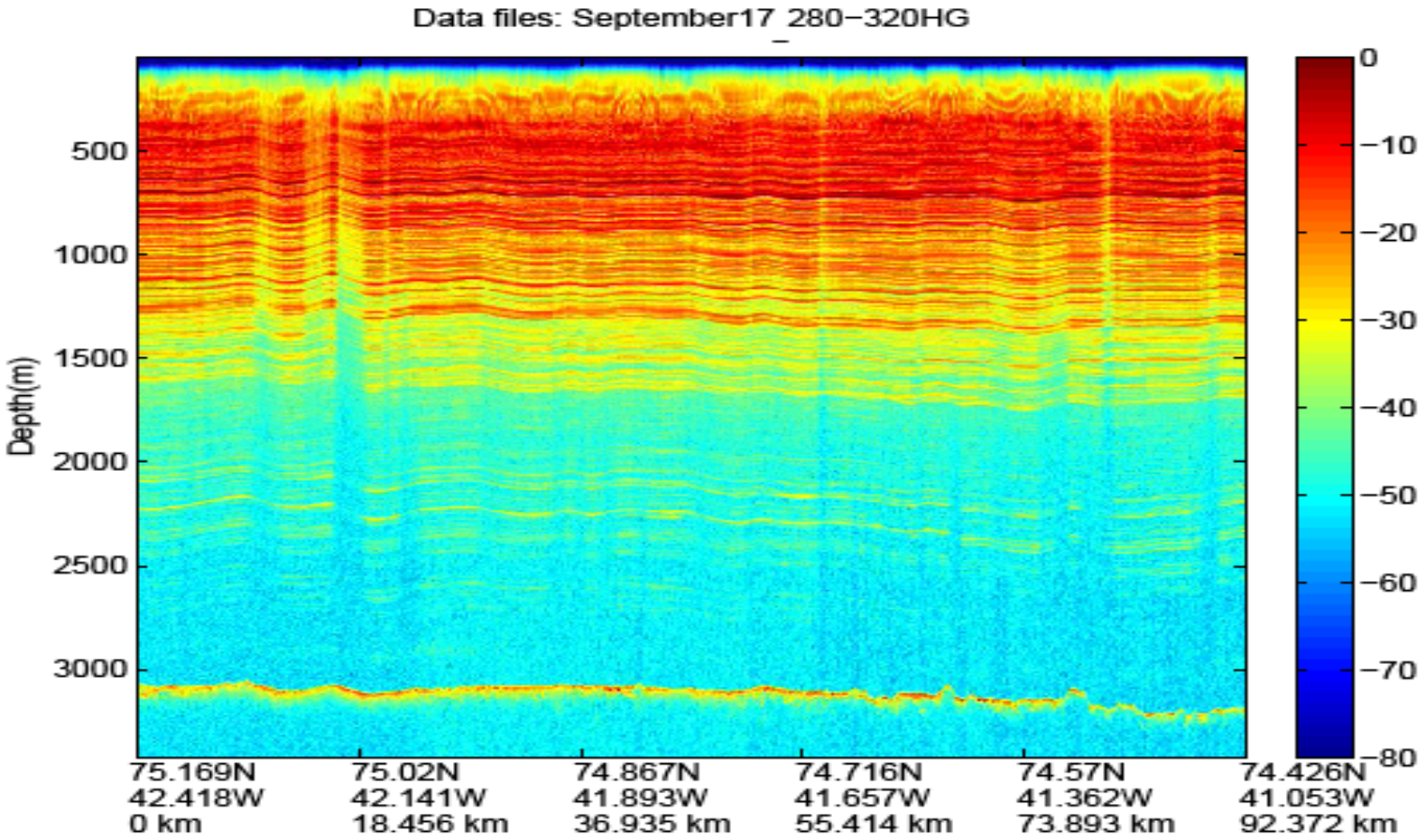

Figure 4.15: SAR Image of Flight Path between NEEM to NGRIP with RFI

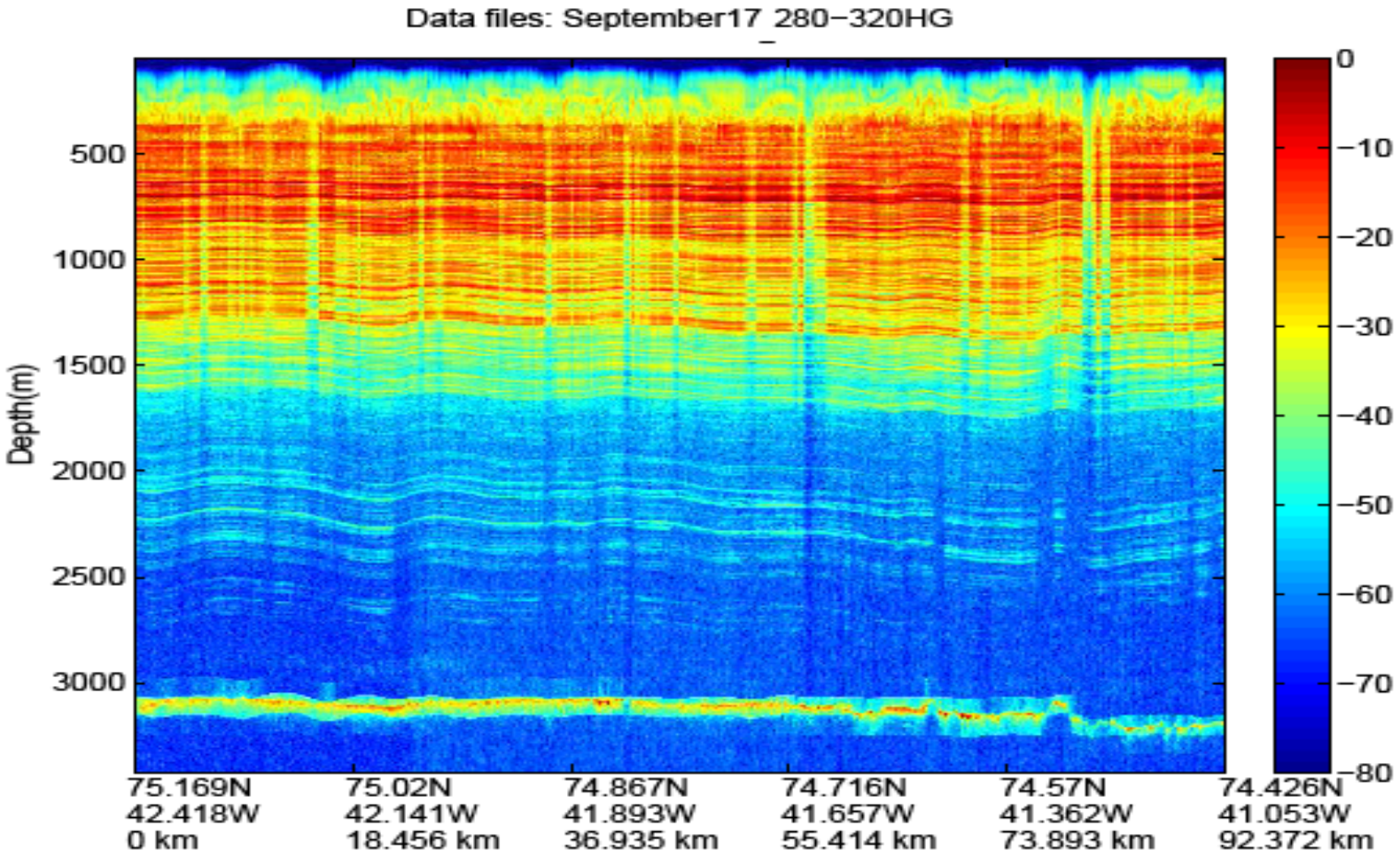

Figure 4.16: SAR Image of Flight Path between NEEM to NGRIP with RFI Supressed

Chapter 5: SAR Processing for Airborne Ice-depth Sounding

5.1 Introduction

The invention of synthetic aperture radar (SAR) is credited to Carl Wiley of Goodyear Aircraft Company, who postulated the concept of Doppler beam sharpening in 1951 [58] . Since then SAR has evolved and has been used in a wide range of civilian and military applications. SAR has revolutionized our ability for ice sheet mapping. Spaceborne SAR provides powerful means to map ice sheet zones, boundaries, surface flow and elevation on a large scale [59, 60]. Airborne and ground-based SAR is able to map basal conditions in detail [61-64]. And the combined analysis of spaceborne and airborne or ground- based SAR helps to understand the ice sheet dynamics better [65].

The advantage of SAR processing for airborne ice-depth sounding is three fold. Firstly, it improves the SNR of ice layers and bed because SAR processing is actually a coherent integration of the multiple observations over the synthesized aperture after the phase differences between the multiple observations are correctly compensated. Secondly, SAR processing refines the azimuth resolution because of the longer synthesized aperture or Doppler beam sharpening. Thirdly, SAR processing rejects the along-track ice surface clutter due to the Doppler phase shift difference between clutter echoes and nadir echoes. The Doppler shift is positive for clutters ahead, negative for clutters behind and zero for nadir signals. On the other

hand, aircraft motion and the refraction at the air-ice interface are two specific issues that have to be dealt with for airborne ice-depth sounding in SAR processing.

Early SAR processing was implemented either with an optical correlator or analog electronic correlator. Digital SAR processor is now popular with the advancement of digital technology and electronics. Different algorithms have been developed for SAR processing either in time domain or frequency domain [66, 67]. This dissertation adopts f-k migration method that originated from wavefront reconstruction theory for seismic signal processing. Compared to time-domain algorithms, f-k method takes advantage of fast Fourier transform in both fast and slow time dimensions. It is much more computationally efficient. It is also convenient to take into the account of the refraction at the air-ice interface and the vertical aircraft motion that is the dominant component for ice-depth sounding. This chapter first introduces the wavefront reconstruction theory, then describes the implementation details of the f-k migration algorithm and the verification of the implemented algorithm by simulation and real sea ice data, and concludes with images of the first ever detected deepest beds of Jakobshavn channel from SAR processing.

5.2 Wavefront Reconstruction Theories

This section provides brief summary of the wavefront reconstruction (WR) theory with particular emphasis on ice-depth sounding and a complete of description of WR theory is given by Yilmaz [68]. As illustrated in Figure 5.1, let us assume that

the aircraft is flying horizontally at constant height h_0 and velocity v_0, and the radar is transmitting signal downward with fixed PRF. The fields of radar EM signal $S(x,z,t)$ in air or ice can be described by the following 2-D wave equation:

$$(\frac{\partial^2}{\partial x^2}+\frac{\partial^2}{\partial z^2}-\frac{4}{c^2}\frac{\partial^2}{\partial t^2})S(x,z,t)=0 \tag{5.1}$$

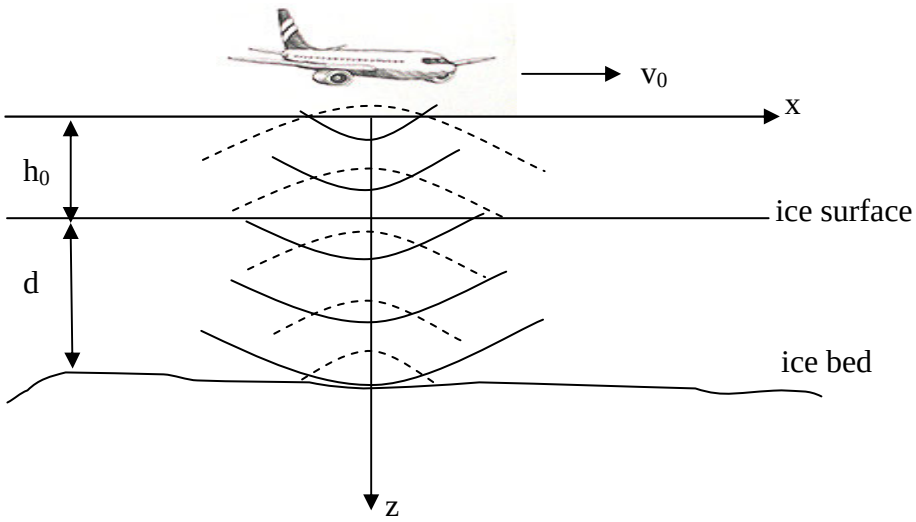

Figure 5.1: Airborne Ice-Depth Sounding Geometry

where x is the coordinate along the horizontal axis pointing to the flying direction, z is the coordinate along vertical axis pointing to nadir, t is the time variable and c is the wave propagation velocity either in the air or ice. The coordinate z is zero along the nominal flight path. Sometimes the x dimension is also referred to as along-track or slow-time and the z dimension as fast-time because the aircraft velocity is much slower compared to the wave propagation. The wave-propagation velocity c can be a

function of x and z in the ice medium. The factor of 4 over c^2 in equation (5.1) takes into account the signal's two-way propagation from the transmitter to the target and then from the target to the receiver. The transmitter and receiver are co-located for monostatic airborne systems. Specifically $S(x,0,t)$ is the signal received at (x,t) and $S(x,z,0)$ is the reflectivity from the target located at (x,z) where a signal source is imagined to 'explode' at time zero. Therefore, the ice-depth sounding turns out to be downward migration from $S(x,0,t)$ to $S(x,z,0)$.

The wave field of $S(x,z,t)$ in frequency and wave-number domain (f,k_x) can be obtained by Fourier transformations over time t and over the horizontal axis x:

$$S(k_x,z,f)=\iint S(x,z,t)e^{-j(2\pi ft-k_x x)}dxdt \tag{5.2}$$

And inversely

$$S(x,z,t)=\iint S(k_x,z,f)e^{j(2\pi ft-k_x x)}dk_x df \tag{5.3}$$

Substitute equation (5.3) into equation (5.1), we get

$$\frac{\partial^2}{\partial z^2}S(k_x,z,f)+k_z^2 S(k_x,z,f)=0 \tag{5.4}$$

where

$$k_z^2=4(\frac{2\pi f}{c})^2-k_x^2=4k^2-k_x^2 \tag{5.5}$$

and $k = 2\pi f / c$ is the total wave number, k_z is the wave number in z dimension. The solution of equation (5.4) for the reflectivity is

$$S(k_x, z, f) = S(k_x, 0, f)\exp(jk_z z) \tag{5.6}$$

The refraction at the air-ice interface and any internal ice layer interface can be handled by using different wave propagation velocities across the interface. At the air-ice interface, we have

$$k_{z\_air}^2 = 4(\frac{2\pi f}{c_{air}})^2 - k_x^2 = 4k_{air}^2 - k_x^2 \tag{5.7}$$

$$k_{z\_ice}^2 = 4(\frac{2\pi f}{c_{ice}})^2 - k_x^2 = 4k_{ice}^2 - k_x^2 \tag{5.8}$$

where c_{air} is the speed of light in the air , $c_{ice} = \frac{c_{air}}{\sqrt{\varepsilon_r}}$ is the speed of light in the ice and ε_r is the relative dielectric constant of ice.

Based on equation (5.3) and (5.6), the basic f-k algorithm for ice-depth sounding, that is to determine $S(x, z, 0)$ from $S(x, 0, t)$, is as follows:

(1) Perform 2-D Fourier transform of $S(x, 0, t)$ over x and t to get $S(k_x, 0, f)$;

(2) Multiply $S(k_x, 0, f)$ firstly by $e^{jk_{z\_air}h_0}$ to migrate $S(k_x, 0, f)$ from the aircraft's height h_0 to ice surface and then by $e^{jk_{z\_ice}d}$ to get the wave fields $S(k_x, z, f)$ at depth d;

(3) Sum all components over f ($t = 0$ at this step in Equation (5.3));

(4) Perform inverse Fourier transform over k_x to obtain $S(x, z, 0)$.

5.3 Motion Compensation

The aircraft's flight path is assumed to be at a constant height in the above f-k migration algorithm. In practice, when an airplane is trying to keep a constant height, it is unavoidable to result in low-frequency height variations because of air turbulence and its longitudinal dynamics [69]. It is intuitive that the height variations will result in topographic deformations of ice surface, layer and bed in the opposite direction in SAR image. The height variations will also result in along-track defocusing based on simulation. The height variations can be calculated with the onboard GPS measurements and be compensated. In ice-depth sounding, the along-track offset is usually much smaller than target range when the synthetic aperture is not very long. In this case, the so-called narrow-beamwidth approximation is valid and the compensation can be accomplished by multiplying the collected data in frequency domain by $e^{jk_c 2\delta h}$ [67]:

$$S(x,0,f) = S(x,0,f)e^{jk_{air}(2\delta h)} \tag{5.9}$$

where δh is the height variation with respect to the nominal height h_0.

As the antenna position is different from that of the GPS receiver, the height difference between the antenna and the GPS receiver is a function of the aircraft's roll angle and pitch angle. The effect of this height difference can be included in

calculating the height variation δh. In flight dynamics, the orientation or attitude of an airplane in the air is defined by three Euler angles between a local earth-fixed coordinate system $o_e x_e y_e z_e$ and the vehicle's body coordinate system $O_b x_b y_b z_b$ with the flat earth assumption. The three Euler angles are roll, pitch and heading angles (ϕ, θ, ψ). Usually $o_e x_e$ is the local north, $o_e y_e$ is the local east and $o_e z_e$ is downward. For our convenience, we translate the origin of $o_e x_e y_e z_e$ to the origin of $O_b x_b y_b z_b$. The body-fixed system will coincide with $o_e x_e y_e z_e$ after three successive rotations which are described by the three matrices in equation (5.10). Therefore, the coordinates of antenna element in $O_b x_b y_b z_b$ can be expressed in $o_e x_e y_e z_e$ as

$$\begin{bmatrix} x_e \\ y_e \\ z_e \end{bmatrix} = \begin{bmatrix} \cos\psi & -\sin\psi & 0 \\ \sin\psi & \cos\psi & 0 \\ 0 & 0 & 1 \end{bmatrix} \begin{bmatrix} \cos\theta & 0 & \sin\theta \\ 0 & 1 & 0 \\ -\sin\theta & 0 & \cos\theta \end{bmatrix} \begin{bmatrix} 1 & 0 & 0 \\ 0 & \cos\phi & -\sin\phi \\ 0 & \sin\phi & \cos\phi \end{bmatrix} \begin{bmatrix} x_b \\ y_b \\ z_b \end{bmatrix} \quad (5.10)$$

And the vertical component is

$$z_e = \begin{bmatrix} -\sin\theta & \cos\theta\sin\phi & \cos\theta\cos\phi \end{bmatrix} \begin{bmatrix} x_b \\ y_b \\ z_b \end{bmatrix} \quad (5.11)$$

So the height difference between the antenna and the GPS receiver is

$$\begin{aligned} \Delta h &= -\Delta z_e = -(z_{e\_antenna} - z_{e\_gps}) \\ &= \begin{bmatrix} -\sin\theta & \cos\theta\sin\phi & \cos\theta\cos\phi \end{bmatrix} \begin{bmatrix} x_{b\_gps} - x_{b\_antenna} \\ y_{b\_gps} - y_{b\_antenna} \\ z_{b\_gps} - z_{b\_antenna} \end{bmatrix} \end{aligned} \quad (5.12)$$

Because the transmitter and receiver antenna array are installed separately under the left and right wing, the right-wing will be going down and the left-wing will be going up for positive roll, and it is vice-versa for negative roll. Therefore, the average of the height differences for the transmitter and receiver antenna are used in the calculation, that is

$$\Delta h = \frac{\Delta h_R + \Delta h_L}{2} \tag{5.13}$$

where Δh_R is different for each receiver element but Δh_L is the same for all transmitter elements assuming a common phase center. Finally the height variation is

$$\delta h = h_{gps} + \Delta h - mean(h_{gps} + \Delta h) \tag{5.14}$$

where h_{gps} is the altitude from GPS data.

The next example will illustrate the effectiveness of the motion compensation algorithm. The data used in the example were collected on September 17 in Greenland in low-gain mode. The data file number is from 30 to 34. The aircraft's average height and speed are 575.11m and 134.50m/s. The time histories in Figure 5.2 show the aircraft's roll, pitch motions and elevation variations. The pitch and roll are from the onboard Inertial Navigation System (INS) measurements and the elevation is from the onboard GPS measurements. The aircraft elevation varies between -58.61 m and 36.68 m with reference to its mean value. Figure 5.3 is the computed height variations of the four antenna elements with respect to the GPS receiver using the equations (5.10) – (5.12).

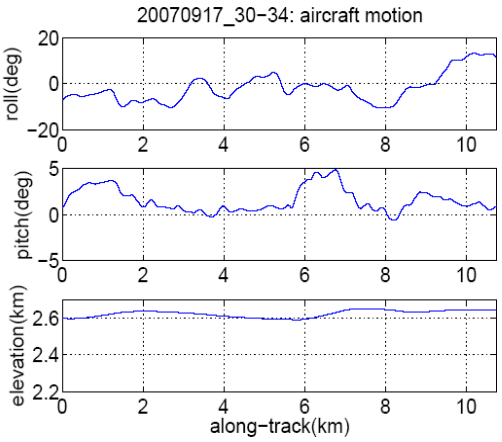

Figure 5.2: Aircraft Motion History

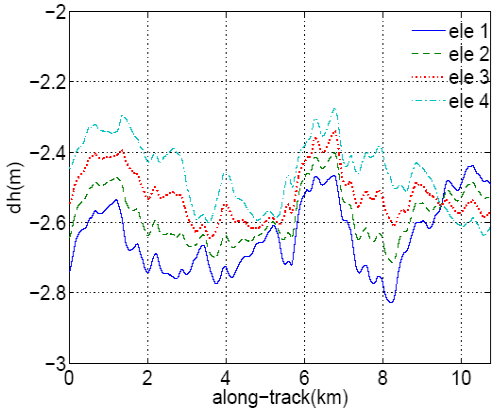

Figure 5.3: Element Height Differences

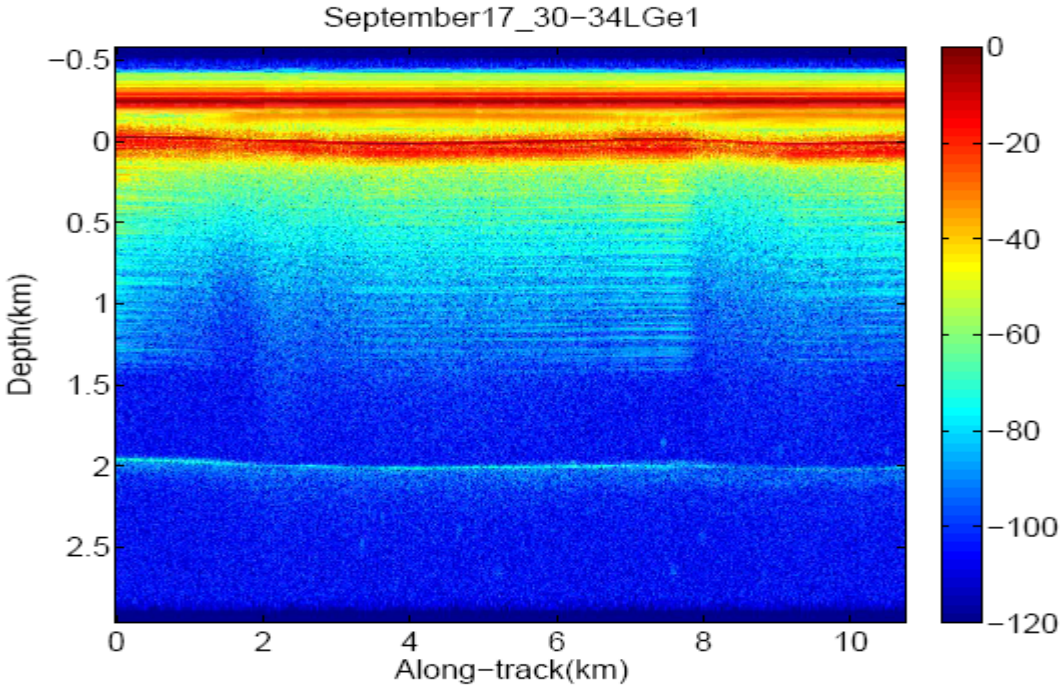

Figure 5.4: SAR Image without Motion Compensation

The SAR image from the first-antenna element without motion compensation is shown in Figure 5.4. It is observed in the image that the feedthrough is horizontally constant without vertical variations as the distance between the transmitter and receiver is fixed and independent of aircraft motions. The surface variations are opposite to the changes of the aircraft elevation. There is obvious defocusing for both surface and ice layers at along-track distance around 2km and 8.5km because of the aircraft's height variations. The ice layers and bed are not flat.

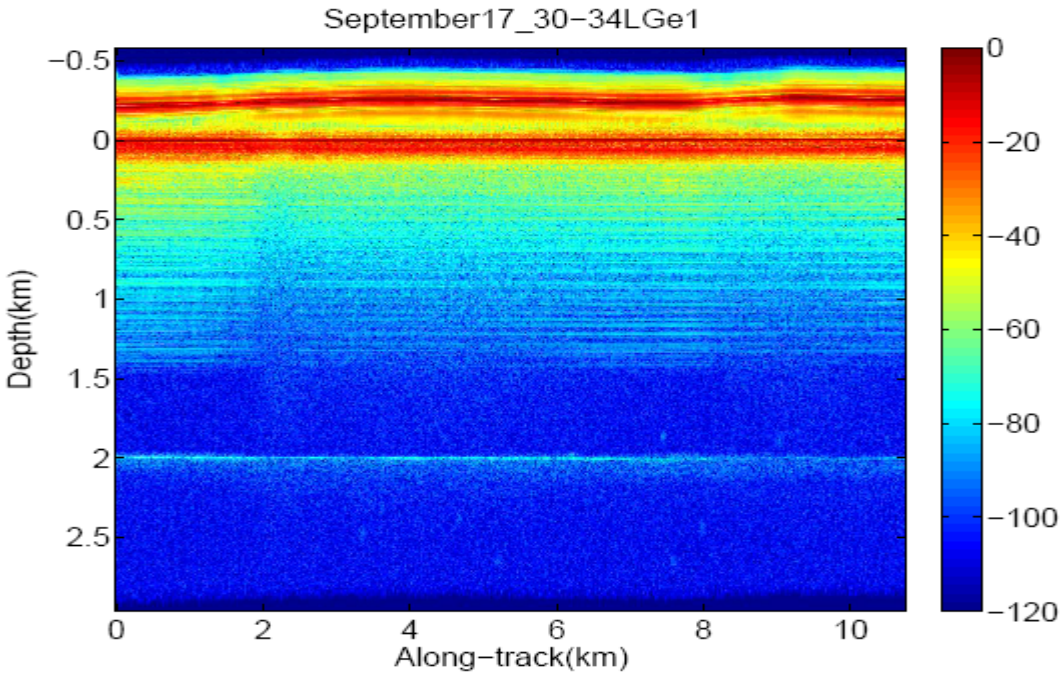

Figure 5.5: SAR Image with Motion Compensation

Figure 5.5 presents the SAR image with motion compensation for comparison. The feedthrough varies vertically after motion compensation which actually represents the aircraft's height variations. The surface, ice layers and bed become flat

and most of the defocusing has been removed by motion compensation. Figure 5.6 (a) and (b) are the zoomed-in images of the feedthrough and surface in linear scale to illustrate their changes more clearly after motion compensation.

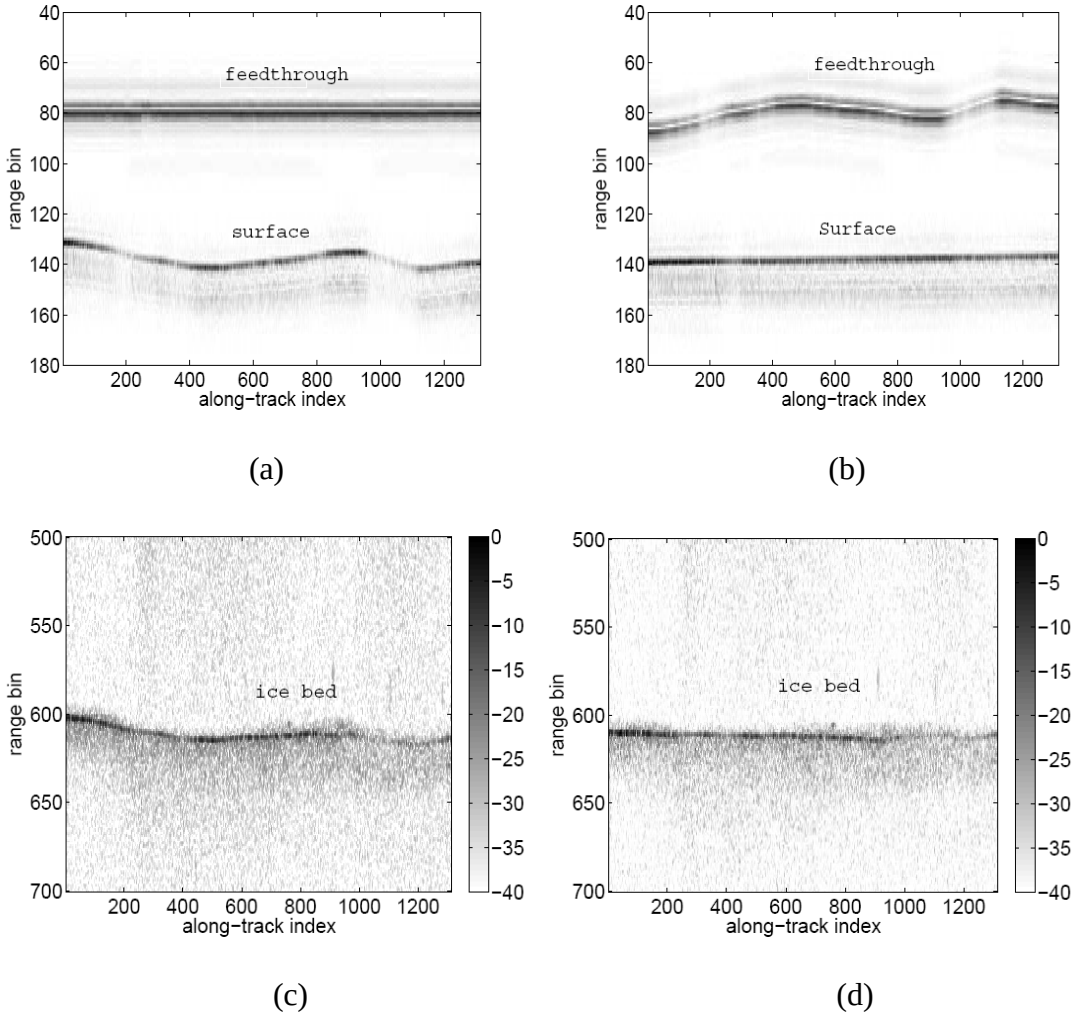

Figure 5.6: Feedthrough, Ice Surface and Bed Comparison with Motion Compensation

(a) and (c) No Motion Compensation,; (b) and (d) with Motion Compensation

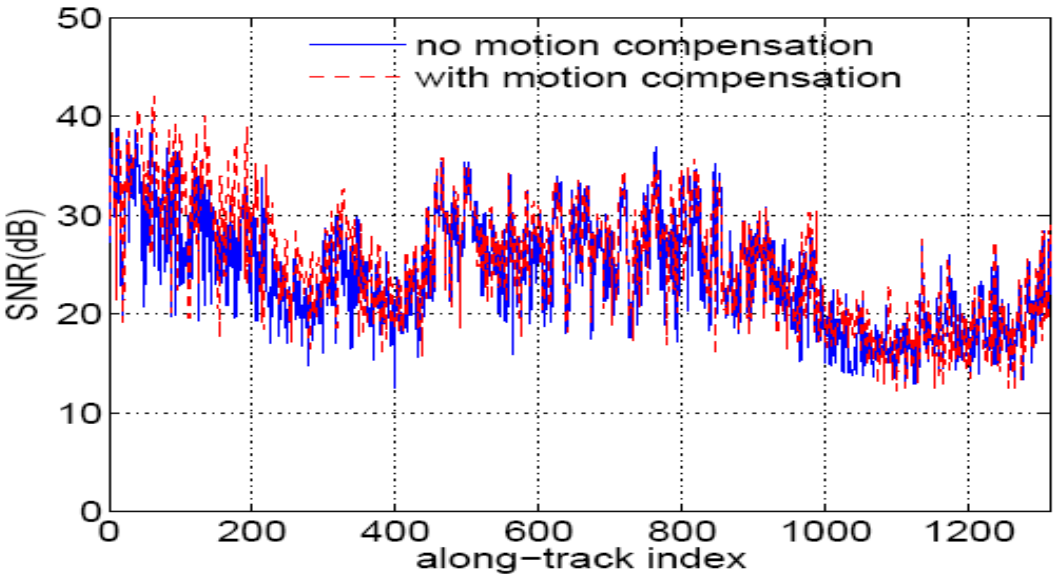

Figure 5.7: SNR Comparison at Ice Bed

Figure 5.6 (c) and (d) are the zoomed-in images of the ice bed to illustrate topographic corrections after motion compensation. Figure 5.7 compares the SNR at the ice bed. The noise level is computed as the average of all the data samples 500 meters beyond the ice bed. The blue chart in the figure is the ice bed SNR without motion compensation and the red-dash chart is the SNR with motion compensation. The average ice bed SNR is 24.08 dB without motion compensation and 25.19 dB after motion compensation. Therefore, on average an improvement of 1.11 dB in SNR at the bed has been achieved by motion compensation. The same comparison has been performed for other data files. Generally the average SNR improvement is around 1~1.6dB.

5.4 Algorithm Implementation and Verification

5.4.1 Algorithm Flow Chart and Implementation

The described f-k migration algorithm for airborne ice-depth sounding has been implemented in MATLAB as illustrated in the flow chart in Figure 5.8. The section describes the implementation step by step:

(1) Compress the received raw data $S(t,x,0)$, which is a $n \times m$ matrix (usually 4672×2500 for a file recorded by MCRDS radars). A column of the matrix is the fast time samples of an echoed transmit pulse and the second dimension of the matrix is the slow time dimension. Each file stores 2500 pulses of the same duration. The raw data are bandpass signals from 20 MHz to 40 MHz with the center frequency at 30 MHz. The bandpass signals are converted to baseband, low-pass filtered and the pulse compression is carried out in frequency domain by multiplication with the conjugate of the base band reference function $S_{b\_ref}(t)$. A window function is applied to the reference function either in time domain or frequency domain to reduce sidelobes from pulse compression. The baseband conversion represents the bandpass signal in complex number with I and Q components of 10 MHz that is half of the signal bandwidth. The bandwidth reduction makes it possible to decimate the data with a larger factor and the required guardband for filtering. The equations for base band conversion and pulse compression are

$$S_b(t,x,0) = S(t,x,0)e^{-j2\pi f_c t} \tag{5.15}$$

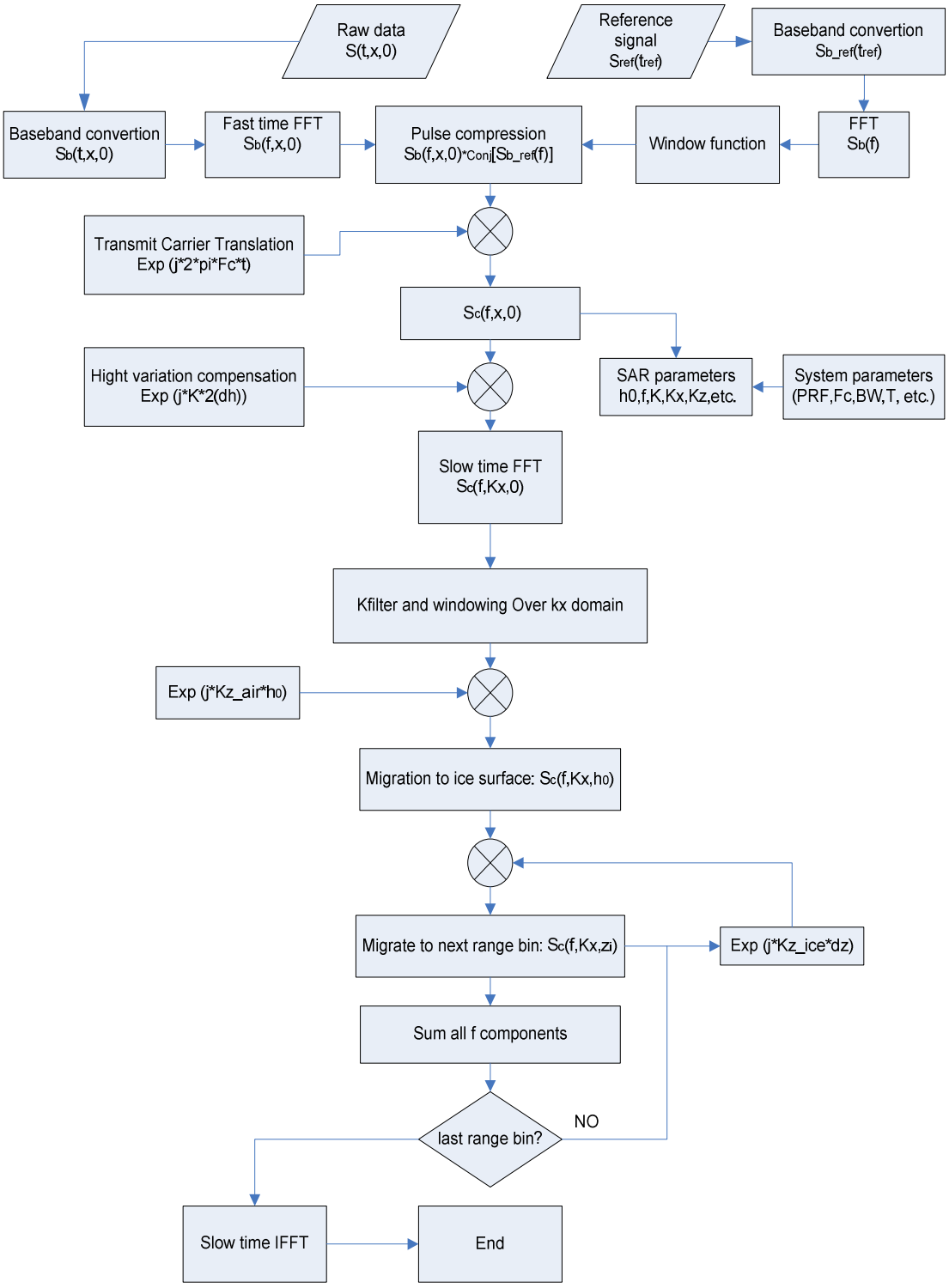

Figure 5.8: Flow Chart of f-k Migration Algorithm for Airborne Ice-depth Sounding

$$S_{b\_ref}(t_{ref}) = S_{ref}(t_{ref})e^{-j2\pi f_c t_{ref}} \tag{5.16}$$

$$S_c(f, x, 0) = FFT[S_b(t_a, x, 0)] \cdot conj(FFT[S_{b\_ref}(t_a)]) \tag{5.17}$$

where $t = [0 : dt : (n-1)dt]$, $t_{ref} = [0 : dt : (n_{ref} - 1)dt]$, $dt = 1/Fs$ is the sampling period which is the reciprocal of the sampling frequency F_s and $n_{ref} = TF_s + 1$ the number of samples of the reference function with duration T. The baseband-converted signal in (5.15) and (5.16) are passed through a Butterworth filter with cutoff frequency at 10 MHz to remove the higher harmonic signals. Butterworth low-pass filter is used because it has the maximum flatness in the passband so that the best sidelobe performance can be achieved during pulse compression. In equation (5.17), the FFT is performed on the fast time dimension and the minimum length of FFT is $n_a = n + n_{ref} - 1$ both for the data and the reference function to avoid circular convolution. Therefore, n_{ref-1} zeros are added on the top of each column of $S_b(t, x, 0)$ to get $S_b(t_a, x, 0)$ and $n-1$ zeros are added at the end of $S_{b\_ref}(t_{ref})$ to get $S_{b\_ref}(t_a)$, where $t_a = [0 : dt : (n_a - 1)dt]$ is the time axis extended by zero appending. The FFT length n_a can also be chosen as the first integer power of 2 greater than $n + n_{ref} - 1$ so that the FFT operation is faster. However, appending too many zeros increases memory requirements, which will be an issue to process big data sets. In order to save memory, fast-time data decimation can be performed at this step. The compressed-data in baseband are then translated to the transmit carrier frequency for SAR processing.

(2) Compute parameters needed in SAR processing with known system parameters and compressed data. The first SAR parameter is the average height h_0 of the aircraft. The average height is calculated from each instant height along track using the strong surface echoes identified in time domain after the radar data are pulse compressed. In order to calculate the instant height as accurate as possible, the maximum surface echo is located as the starting point, and then surface echoes are searched on both sides of the maximum surface echo. When there is a sudden jump exceeding a reasonable threshold at an along-track position, the height is set to the value of its previous location. After removing the unusual jumps which always happen in radar data, a polynomial fit equivalent to a low-pass filter is applied to the surface echoes to get the instant height at each along-track position. Other SAR parameters, including the frequency axis f , wave number axes k_x and k_z are calculated as follows:

$$f = F_c + [-\frac{n}{2}\Delta f : \Delta f : (\frac{n}{2} - 1)\Delta f] \tag{5.18}$$

$$k_x = [-\frac{m}{2}\Delta k_y : \Delta k_y : (\frac{m}{2} - 1)\Delta k_y] \tag{5.19}$$

$$k_z = \sqrt{4k^2 - k_x^2} = \sqrt{4(\frac{2\pi f}{c})^2 - k_x^2} \tag{5.20}$$

where F_c is the transmit carrier frequency, $\Delta f = F_S/(n-1)$ is the frequency spacing between two adjacent samples, $\Delta k_y = \frac{2\pi}{(m-1)\Delta y}$ is the along-track wave number spacing and Δy is the average distance the aircraft moves between two adjacent

records. In operation the aircraft cannot fly at an absolute constant speed, the actual spatial distance between two adjacent records may have small variations. The variation can be accounted for by data interpolation in slow time domain. However no obvious improvements have been observed by comparing f-k migrated data with and without interpolation. In equation (5.19), k_x is limited within [-2k, 2k] and the k, k_z in equation (5.20) should be calculated separately for both air and ice medium according to equations (5.7) and (5.8).

(3) Compensate height variations by applying the filter $e^{jk(2\delta h)}$ to the fast time compressed data in frequency domain. This is accomplished according to equations (5.9) ~ (5.14).

(4) Take FFT in slow time dimension to transform the data in f-k domain

(5) Apply K-filter in f-k domain. The so-called K-filter controls the aperture length in SAR processing and removes noise energy. K-filter is actually an idealized antenna radiation pattern filter implemented in wave number domain. Figure 5.9 illustrates an antenna element with beamwidth β. For a point target T at depth d, the effective synthesized aperture length is L. As the aircraft arrives at the left end of L, the target first enters the element's field of view. As the aircraft leaves the right end of L, the target exits the element's field of view. From the geometry, it is obvious that

$$L = 2d \tan\frac{\beta}{2} \tag{5.21}$$

and in wave number domain,

$$\frac{\beta}{2} = \sin^{-1}\frac{k_x}{2k} \tag{5.22}$$

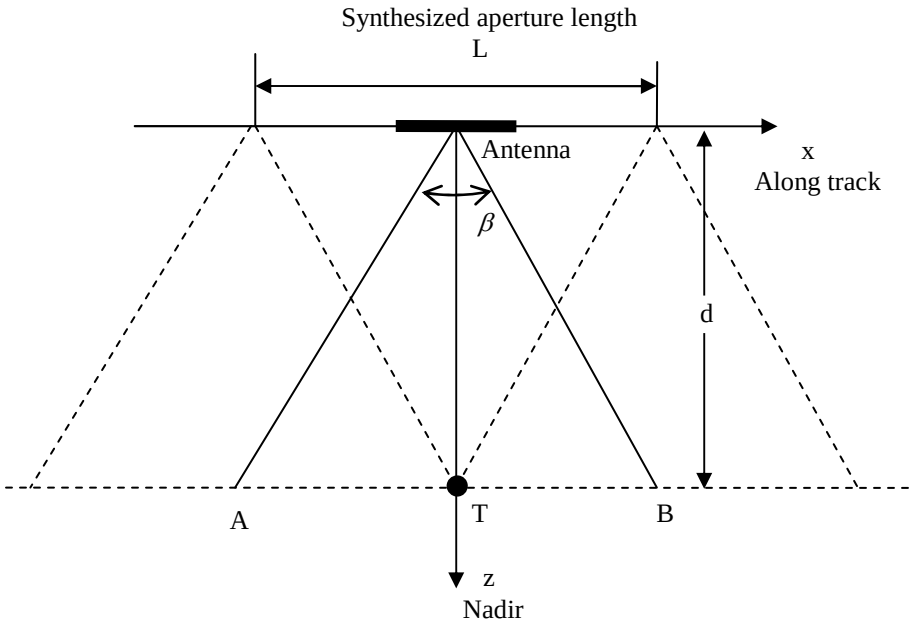

Figure 5.9: Geometry of K-filter

So the K-filter is

$$K\_filter = 1 \qquad \text{if} \quad \left|\sin^{-1}\frac{k_x}{2k}\right| \le \frac{\beta}{2} \tag{5.23}$$

$$K\_filter = 0 \qquad \text{if} \quad \left|\sin^{-1}\frac{k_x}{2k}\right| > \frac{\beta}{2} \tag{5.24}$$

Apply the K-filter to the data as follows:

$$S(f, k_x, 0) = S(f, k_x, 0) * K\_filter * W_k \tag{5.25}$$

The window function W_k is applied to reduce the sidelobes from azimuth compression.

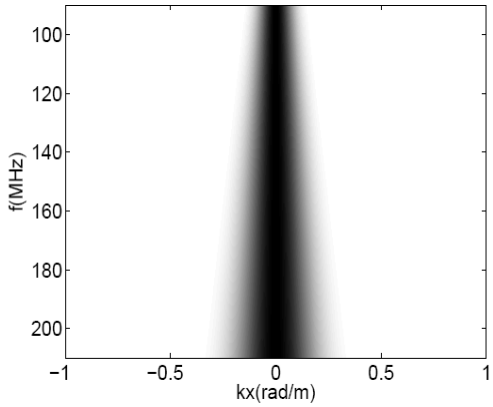

Figure 5.10: Trapezoidal K-filter

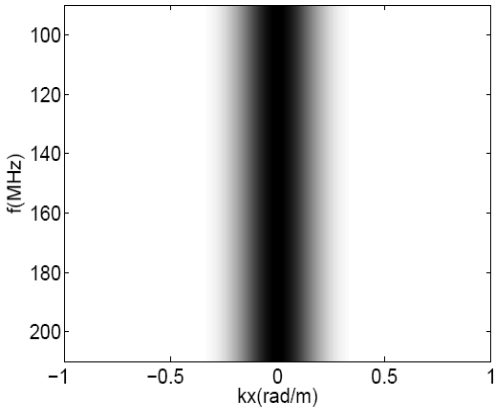

Figure 5.11: Rectangular K-filter

The K-filter described by equations (5.23) and (5.24) is trapezoidal in f-k domain as shown in Figure 5.10. The aperture length is proportional to depth in this case. The K-filter keeps the signal energy within the trapezoid and nulls the noise outside of the trapezoid. However this nulling sometimes may result in some artifacts because the algorithm sums all frequency components (step 8) for each k_x but at edges of the filter some lower-frequency components have been removed at this step. Therefore, the rectangular filter shown in Figure 5.11 is employed to avoid the artifacts. The aperture length is constant for all depth in this case and the filter keeps the signal energy within $\pm k_{x\_\max}$ and nulls the noise outside of the rectangle. The parameter $k_{x\_\max}$ is half of the maximum width of the trapezoidal K-filter.

(6) Migrate the data in air medium from the average aircraft height to ice surface by multiplying the data with $e^{jk_{z\_air}h_0}$.

(7) Migrate the data from ice surface to the first range bin and then from the first range bin to deeper ice with a step size of dz which can be a range bin or multiple range bins. This is accomplished by multiplying the data by $e^{jk_{z\_ice}dz}$. In the fast time dimension, the first range bin is assumed to be at zero time in previous steps, but actually there is a time delay between transmit (corresponding to the real zero time) and the time when the first range bin is recorded. The time shift is compensated in frequency domain at this step by multiplying the migrated data at the first range bin by $e^{-j2(k_{air}h_0+k_{ice}z_1)}$.

(8) Sum all frequency components at each depth by adding up all samples in a column.

(9) Take IFFT of the summed data for all depths to get the final SAR image.

5.4.2 Algorithm Verification

The implemented algorithm described in section 5.4.1 is verified with both simulation and real data.

(1) Verification with simulation

Five point targets in ice at different depths and azimuth positions are simulated with MCRDS radar parameters [70, 71]. The coordinates (x, z) of the five point targets are (0, 500), (100, 1000), (-200, 1500), (-250, 2000) and (300, 3000) in meters. The aircraft height and speed is 500m and 60m/s, which is typical in the radar operation with Twin Otter airplane. The antenna beamwidth is set to 10 degrees. In the simulation, the transmit chirp is assumed to be 3 us, and the received signal is the

superposition of the five point target responses. The refraction at the air-ice interface is modeled according to geometry and the Snell's law [72]. A simplified case is first simulated, assuming the point targets are perfect reflectors, no signal spreading loss in air, propagation loss in ice and receiver noise. This simulation is to ensure the pulse compression performance in terms of range resolution and sidelobe levels, to verify the f-k migration across air and ice media, the azimuth resolution improvement and the narrow-beamwidth motion compensation. The five lightly-curved strips in Figure 5.12 are the receiver signals from the five point targets. The strip length is proportional to the range for the fixed antenna beam width pattern and the strip width is 450m corresponding to the pulse duration. The five strips are compressed into the five slightly-curved lines in Figure 5.13. The 3dB compressed pulse width is 6.33m as result of using Hanning window to reduce the sidelobes, which is 1.5 times of the pulse width of match filtering. The first range sidelobe is -31.6 dB that matches the theoretical value of Hanning window. Figure 5.14 shows the five curved lines focus into five points after f-k migration. Since in the simulation the rectangular K-filter's width and the window width are determined by the depth of deepest point target, the azimuth sidelobe of this target is -31.6 dB that matches the theoretical value of Hanning window. However the window size is wider for other shallower targets, the azimuth sidelobes are therefore higher. The sidelobe increases to -28.5 dB for the target at the surface. The azimuth resolution is 5.72 m for the deepest target which is the theoretical value for 10-degree aperture. The other shallower targets have better azimuth resolutions because the rectangular K-filter results in larger apertures than 10

degrees for them. The azimuth resolution of the surface target is 4.76m which is the best. In order to illustrate the motion effects clearly, large height variations ($\sigma = 20cm$) are introduced in the simulation. Figure 5.15 shows the five point targets blur and spread along-track without motion compensation. These effects are removed with motion compensation included in the simulation and the SAR image is almost the same with Figure 5.14.

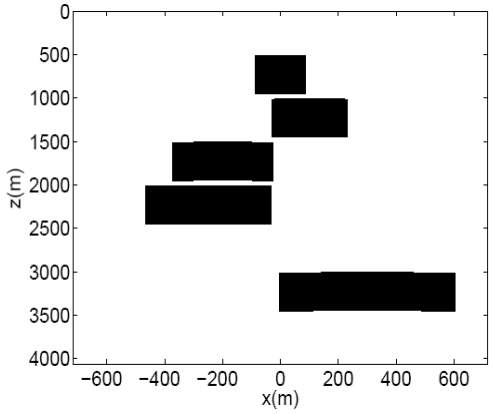

Figure 5.12: Simulated SAR Signals

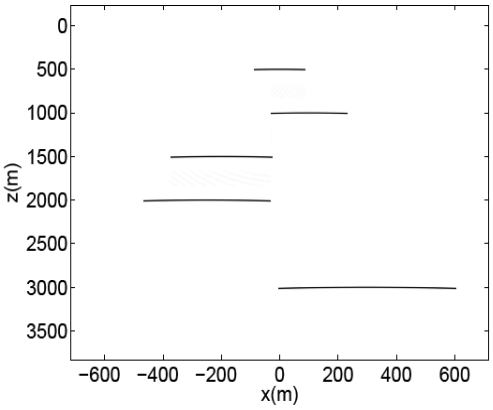

Figure 5.13: Compressed SAR Signals

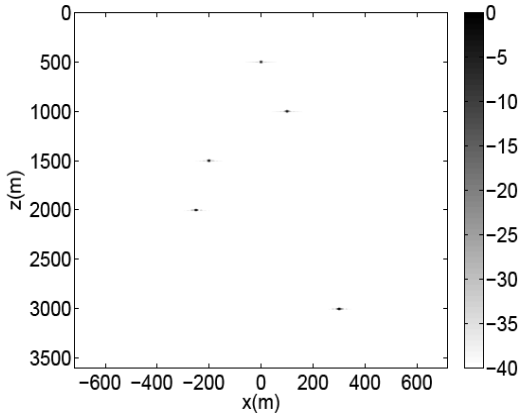

Figure 5.14: Simulated SAR image

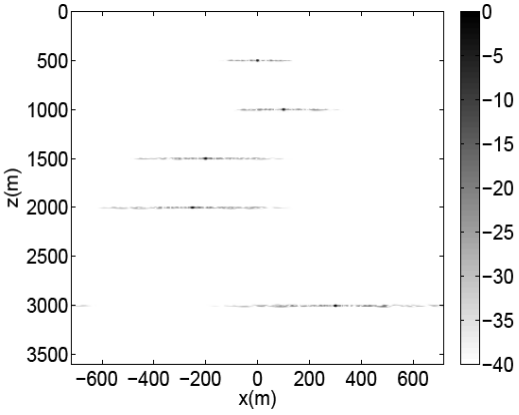

Figure 5.15: Height Variation Effect

A more realistic case is then simulated to verify the SNR improvement of SAR processing. In this case the reflectivity is assumed to be a simple exponential function of incidence angle. The signal spreading loss in air and the propagation loss in ice (20dB/km) are included. The receiver noise is

$$N = kBT_0F = 1.38065\times10^{-23}\times20\times10^{6}\times290\times10^{3/10} = -127.96dB \quad (5.26)$$

Figure 5.16 is the simulated received signals from the five point targets, which shows only the first point target is visible and other point targets are immerged in noise. Since the transmit power is 800 W (29 dBW) and the minimum signal power loss from spreading and ice attenuation is around -150 dB according to Figure 5.19, the biggest received power is around -121 dBW that is 7 dB above the noise power. This explains why it is visible. But for the second target, the minimum signal power loss is around -170 dBW, and the biggest received power is around -141 dBW that is below the noise power. For a bandwidth-time product of 60, the signal-to-noise ratio improvement from pulse compression is about 17.78 dB minus the loss from mismatch filtering. Therefore, the power level after range compression would be around the level of the noise. This explains why the second target is barely visible in Figure 5.17 and other three targets with bigger power losses are invisible. As expected, further signal-to-noise ratio improvement from SAR processing brings up the second target at location (100, 1000) from noise. This is shown in Figure 5.18.

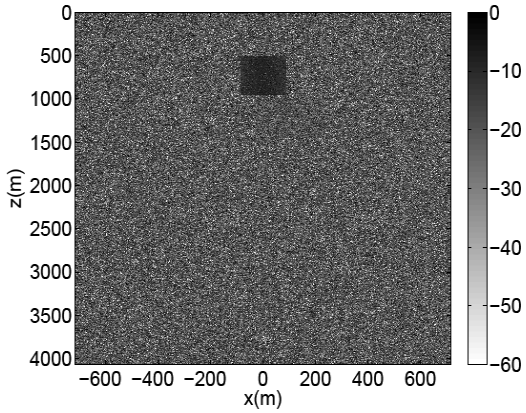

Figure 5.16: SAR Signals with Noise

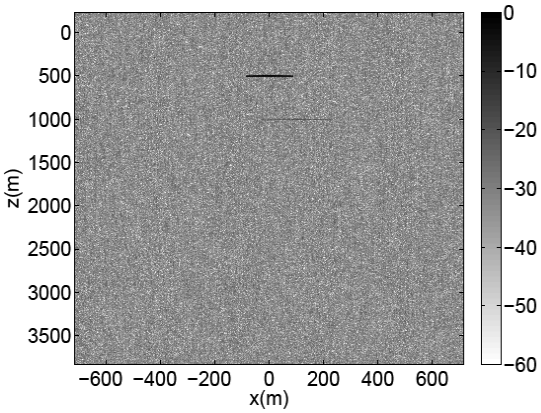

Figure 5.17: Compressed SAR Signals with Noise

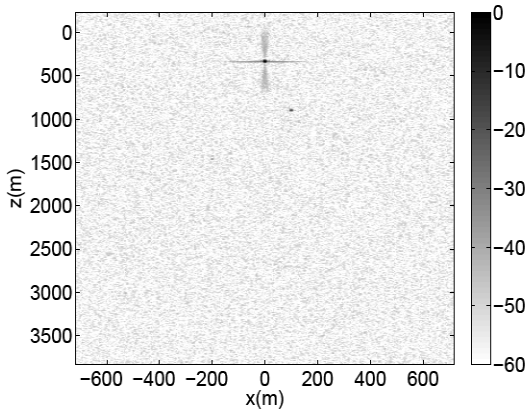

Figure 5.18: SAR Image with Noise

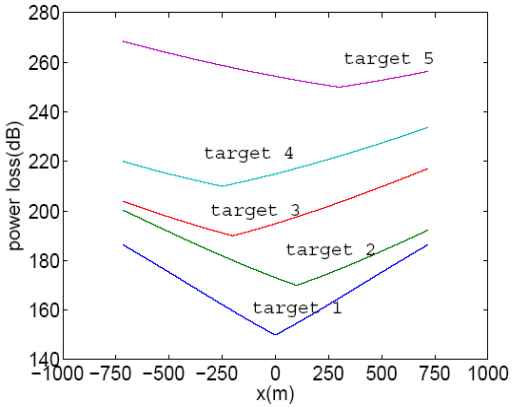

Figure 5.19: Simulated Signal Power Loss

(2) Verification with simulation and sea ice data

The algorithm is further verified using MCRDS P-3 radar parameters and a method that combines simulation and a set of sea ice data collected on September 13, 2007 during the Greenland survey. Figure 5.20 illustrates the verification method and Figure 21 is the picture of the sea ice in the sea close to Humboldt glacier, Thule, Greenland. Since the strong reflection from the edge of sea ice is similar to the response of a point target, a point target is simulated to have the same radar system

and SAR geometry parameters with a selected piece of sea ice. The output of the SAR code using the simulated data is verified first in terms of SNR and resolution improvements and then compared with the output using the sea ice data. Figure 5.22 shows the radar echogram of the sea ice from the low-gain mode. Each hyperbola represents a chunk of sea ice at different range and azimuth position. The aircraft height, speed and the spacing between two adjacent records are respectively 660 meters, 123.83 m/s and 0.7926m. Figure 5.23 is the output image from the SAR algorithm code, which shows the hyperbolas focus into point targets after SAR processing. The selected piece of sea ice in simulation is around the middle of the SAR image and are marked both in Figure 5.22 and 5.23 as the point target. The target range is 3225.8m (2565.8m+660m) and the along-track distance relative to the first pulse of the data set is 4797.4m.

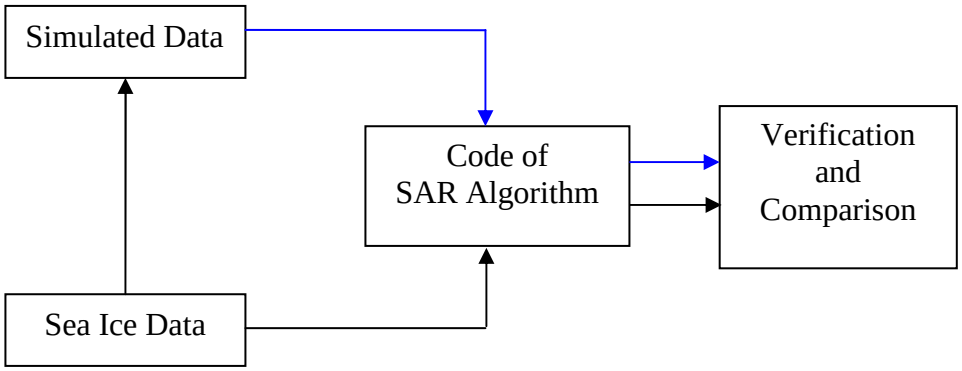

Figure 5.20: Block Diagram of SAR Algorithm Verification

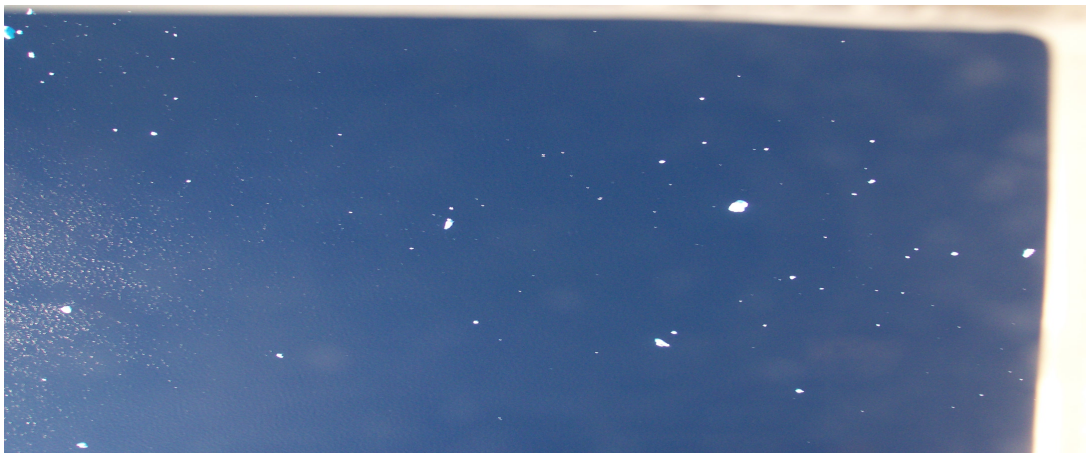

Figure 5.21: Picture of Sea Ice (courtesy of NASA)

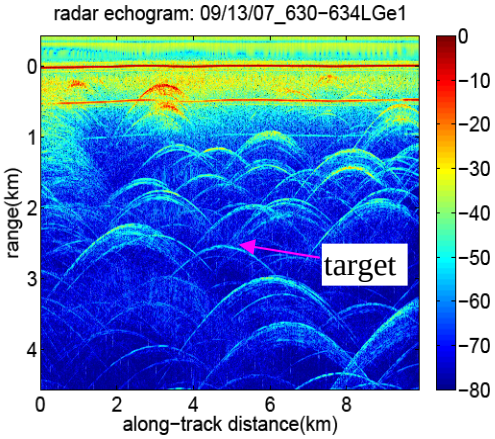

Figure 5.22: Echogram of Sea Ice Data

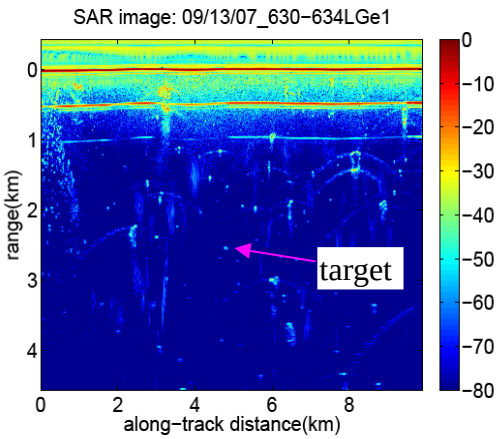

Figure 5.23: SAR Image of Sea Ice

For convenience to verify the SNR improvement from signal processing, the SNR is set to zero in the simulation. Figure 5.24 shows the zoomed-in SAR images of the point target from the simulation and sea ice. Because the sea-ice edge is not a perfect point reflector, it is observed from Figure 5.24 that the simulated point target has a perfect shape and better resolution compared to the sea-ice result. Figure 5.25 shows the A-scopes across the point target from the simulation. The A-scope across

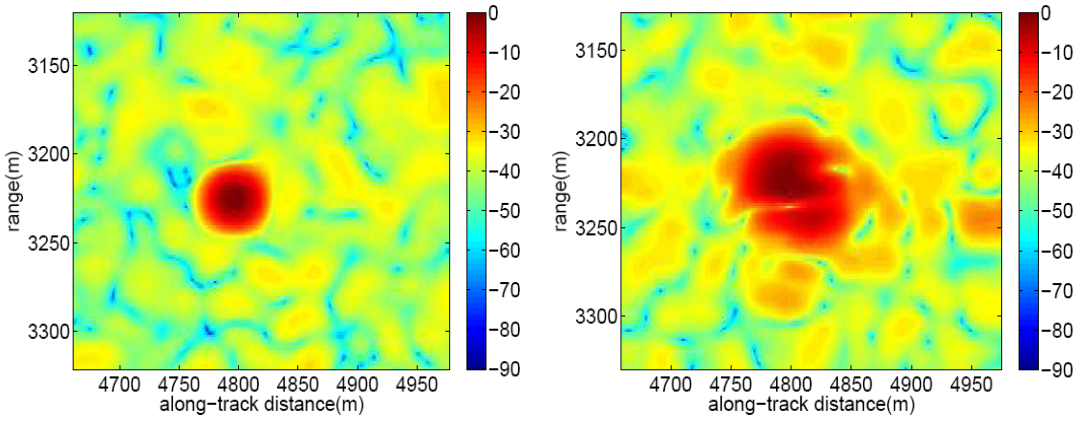

(a) (b)

Figure 5.24: Zoomed in SAR Images of Point Target: (a) Simulation; (b) Sea Ice

the point target in range dimension in plot (a) shows the target is buried in noise before range compression. The A-scope in plot (b) shows the target is brought up from noise as a result of SNR improvement by range compression. The SNR improvement is around 17.8dB which is as expected because the signal's time-bandwidth product is 60(3us by 20MHz). The range resolution from simulation turns out to be 13.5m. The range resolution loss factor is 1.8 from mismatch filtering with Chebyshev window. Plot (c) is the A-scopes across the point target in range dimension after SAR processing. The blue chart in the plot corresponds to an aperture of 281m (5-degree antenna beamwidth). The SNR is about 42.8dB, which means an improvement of 25dB from SAR processing. This is as expected, as for an aperture of 281m about 355 data points along the hyperbola are coherently integrated. The red chart in dash line corresponds to a longer aperture of 562m (10-degree antenna beamwidth). It is observed the range resolutions are the same and the longer aperture

results in additional SNR improvement of 3dB. Plot (d) is the A-scopes across the point target in azimuth dimension after SAR processing. The blue chart in the plot corresponds to the shorter aperture and the red chart in dash line corresponds to the longer aperture. It is observed the azimuth resolution is about twice better for the longer aperture.

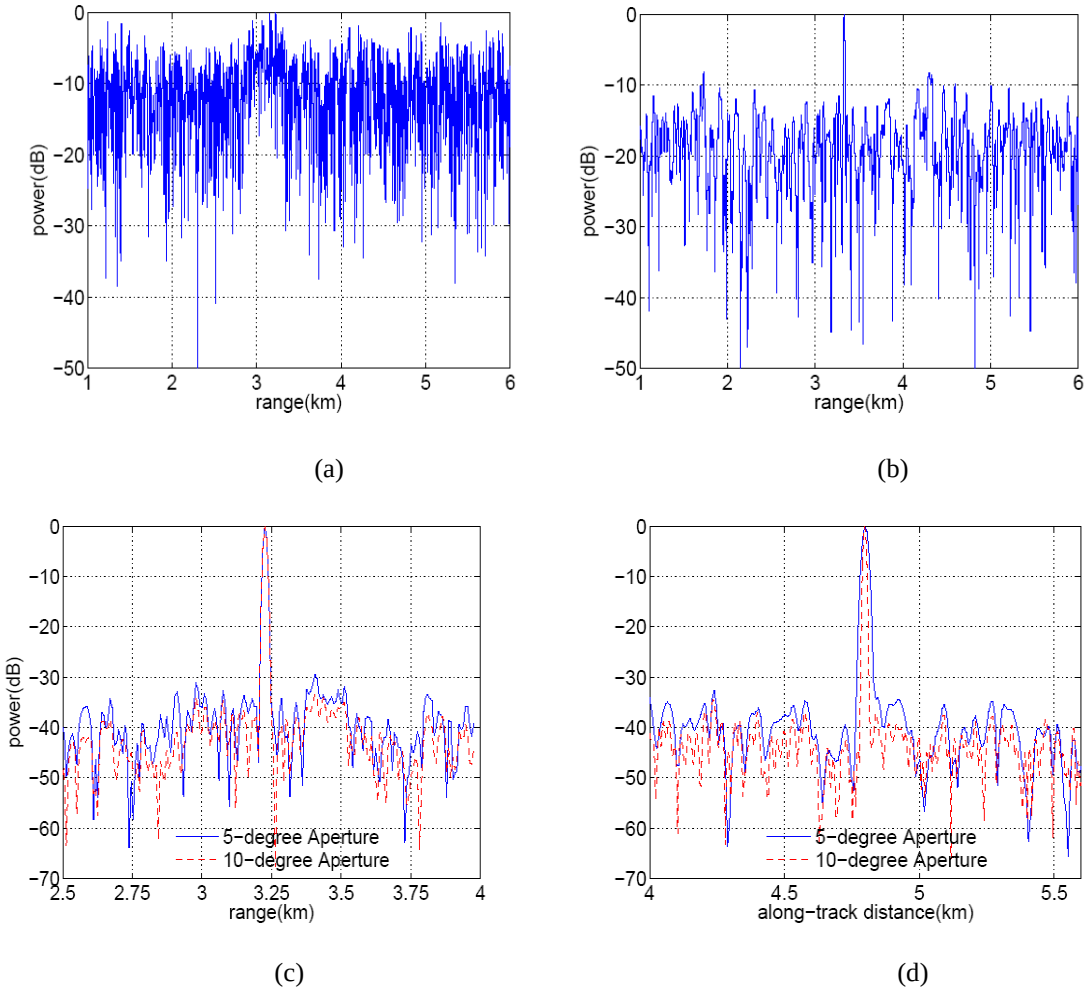

Figure 5.25: A-scopes from Simulation: (a) Range Dimension before Pulse Compression; (b) Range Dimension after Pulse compression; (c) Range Dimension after SAR Processing; (d) Azimuth Dimension after SAR Processing

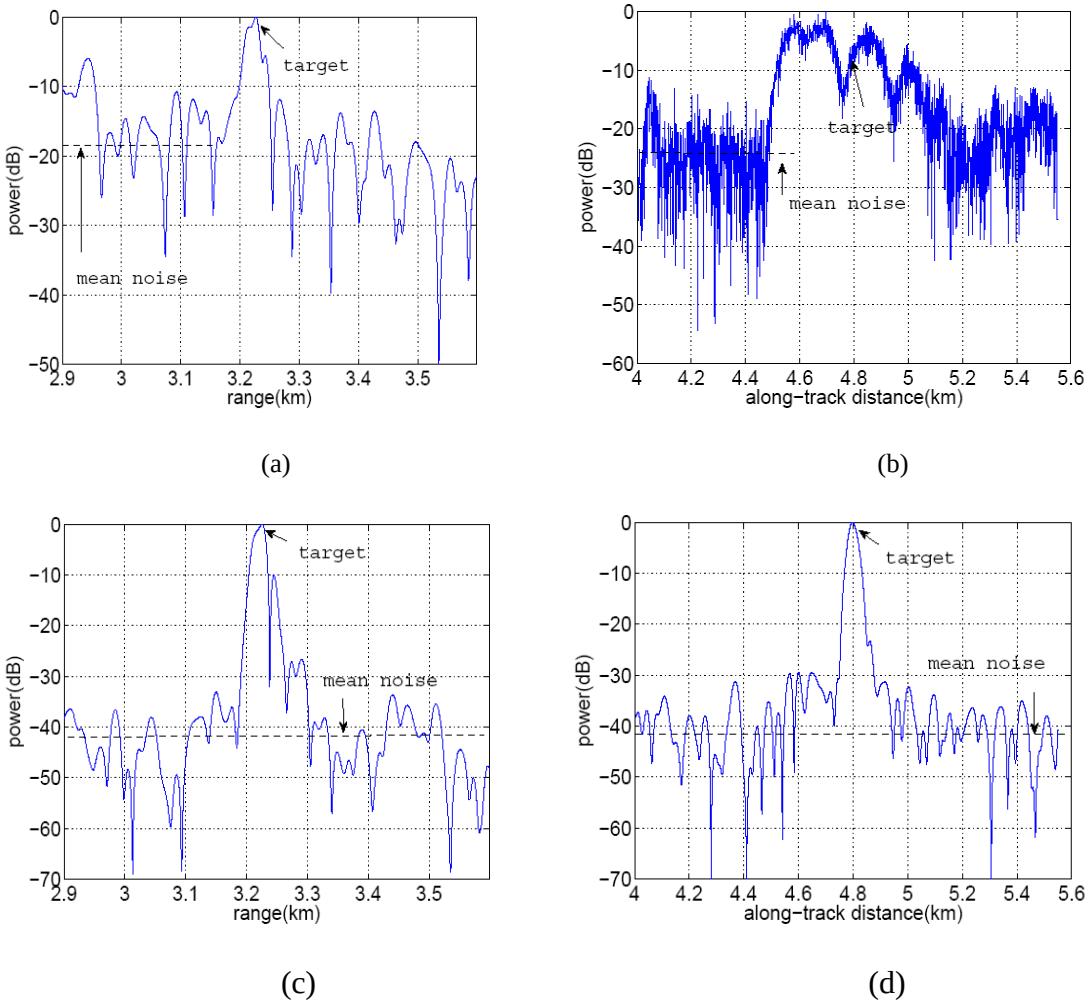

Figure 5.26: A-scopes from Sea Ice: (a) Range Dimension after Pulse Compression; (b) Azimuth Dimension after Pulse compression; (c) Range Dimension after SAR Processing; (d) Azimuth Dimension after SAR Processing

Figure 5.26 are the A-scopes across the sea-ice point target. Plot (a) and (b) are the A-scopes across the sea-ice target respectively in range and azimuth dimensions after pulse compression. Since the echo SNR from this piece of sea-ice happens to be around 0 dB, the SNR is around 17.8 dB after pulse compression. Plot (c) and (d) are the A-scopes across the sea-ice target, respectively, in range and

azimuth dimensions after SAR processing that show the SNR is around 42.8 dB and the SNR improvement from SAR processing is close to 25dB. The range and azimuth resolutions are 20.4 m and 34.3 m according to the A-scopes. Table 5.1 puts together the SNR improvement from SAR processing, range resolution and azimuth resolutions for comparison.

Table 5.1: Comparison of Simulated Data and Sea Ice Data (5-degree Aperture)

	Simulated Data	Sea Ice Data
Range Resolution	13.5m	20.44m
Azimuth Resolution	21m	34.3m
SNR Improvement by SAR	25dB	~ 25dB

5.5 Data Processing Results of Jakobshavn Glacier

Jakobshavn glacier is a large outlet glacier in west Greenland. It is one of the fastest flowing glaciers on Earth and a major component of ice balance of Greenland ice sheet. The glacier's discharge has doubled in recent years. It drains about 7.5% of all the Greenland Ice Sheet. In order to better understand the ice dynamics behind this rapid increase in ice discharge, remote sensing data were collected using MCRDS Twin Otter along and across the glacier channel on May 29 and 30 in 2006. The map in Figure 5.27 shows the glacier's east-westward ice stream and three cross flight lines marked with three blue short lines. The channel extends about 150 km from

calving front to the ice sheet interior where several ice-stream tributaries join to form the main channel of the glacier. The three cross-flight lines are respectively about 42 km, 52.5 km and 63 km upstream of the calving front, and are numbered as cross flight 1, 2 and 3 from east to west for convenience of reference.

Figure 5.28, 5.30 and 5.32 are the SAR images of the channel using high-gain data from these three cross flights. A very large synthetic aperture length (30-degree antenna beam width) and careful array processing were used to enhance the very weak returns from the deep ice bed of the channel. Since the signal propagation loss is much greater in the channel than in the interior of the ice sheet where the thickness is the same, even with the high sensitivity of the MCRDS Twin Otter, elaborate SAR and array processing, the ice bed of the channel are barely mapped from cross flight 1 and 2. The ice bed of the channel is clearly mapped from cross flight 3. This is because the thickness of cross flight 3 is about 200 meters less compared to cross flight 1 and 2. Figure 5.29, 5.31 and 5.33 are A-scopes corresponding to the red-dashed lines in Figure 5.28, 5.30 and 5.32. Theses A-scopes show that the SNR at the channel ice bed is only about 3dB for cross flight 1 and 2, and 4 dB higher for cross fight 3. The ice thickness is about 2.7 km for cross flight 1 and 2 and 2.5km for cross flight 3. These are the first ever radar soundings of the deepest parts of the Jakobshavn channel and match with seismic measurements [73].

Figure 5.32 and Figure 5.34 clearly show in the channel the large amount of signal attenuation, which is one of the major challenges in sounding fast-flowing glaciers like Jakobshavn. The received signal as a function of depth is compared at two locations in Figure 5.32: (1) outside the channel marked with the red-solid line and (2) in the channel marked with the red-dashed line. Figure 5.34 is the A-scope comparison that indicates the in-channel bed return is 70 dB lower than that for 1-km thick ice outside the channel. The total thickness of ice in the channel is about 2.5 km. Thus, the total loss consisting of propagation and return losses is about 70 dB for 1.5 km thick ice in the channel in contrast to the 60 dB combined loss reported by Paden [74] for more than 3-km thick ice in the interior of an ice sheet. The very high loss might be from warm ice near the bed, high return loss due to impedance matching effect caused by increase in ice temperature as a function of depth near the bed, and additional scattering loss from volume inclusions in the ice.

The SAR images from the cross flights provide detailed knowledge of the channel's geometry which is important to understand the glacier's ice dynamics. According to these images, the channel width is about 7 km at the top and narrowed to several hundred meters at the bed. It is analyzed that the topographic effects of the channel's narrow width and large depth may increase the geothermal heat flux by as much as 50% that is supplied to the basal ice to facilitate fast flow [64].

Figure 5.35 is the SAR image from the flight line along the channel on May 29, 2006. The channel bed is clearly mapped from 60 km to 130 km of the calving front. It is observed that there are two distinct, although weak, echoes for the first 40 km shown in the image: one from the bed and the other from an interface located between 200 m and 500 m above the bed. Measurements of the temperature adjacent to and in the channel indicated that there might be 200-500 m of temperate ice at the base of the glacier [75-77]. The return above the bed in the radar image might be from the cold-temperate ice interface.

Finally Jokobshavn thickness profile and elevation is given in Figure 5.36 combining the along, cross flight lines radar data and the NASA Airborne Thematic Mapper data. In the figure, the thickness below the sea level are plotted in blue vertical lines and the thickness above the sea level are plotted in light gray vertical lines.

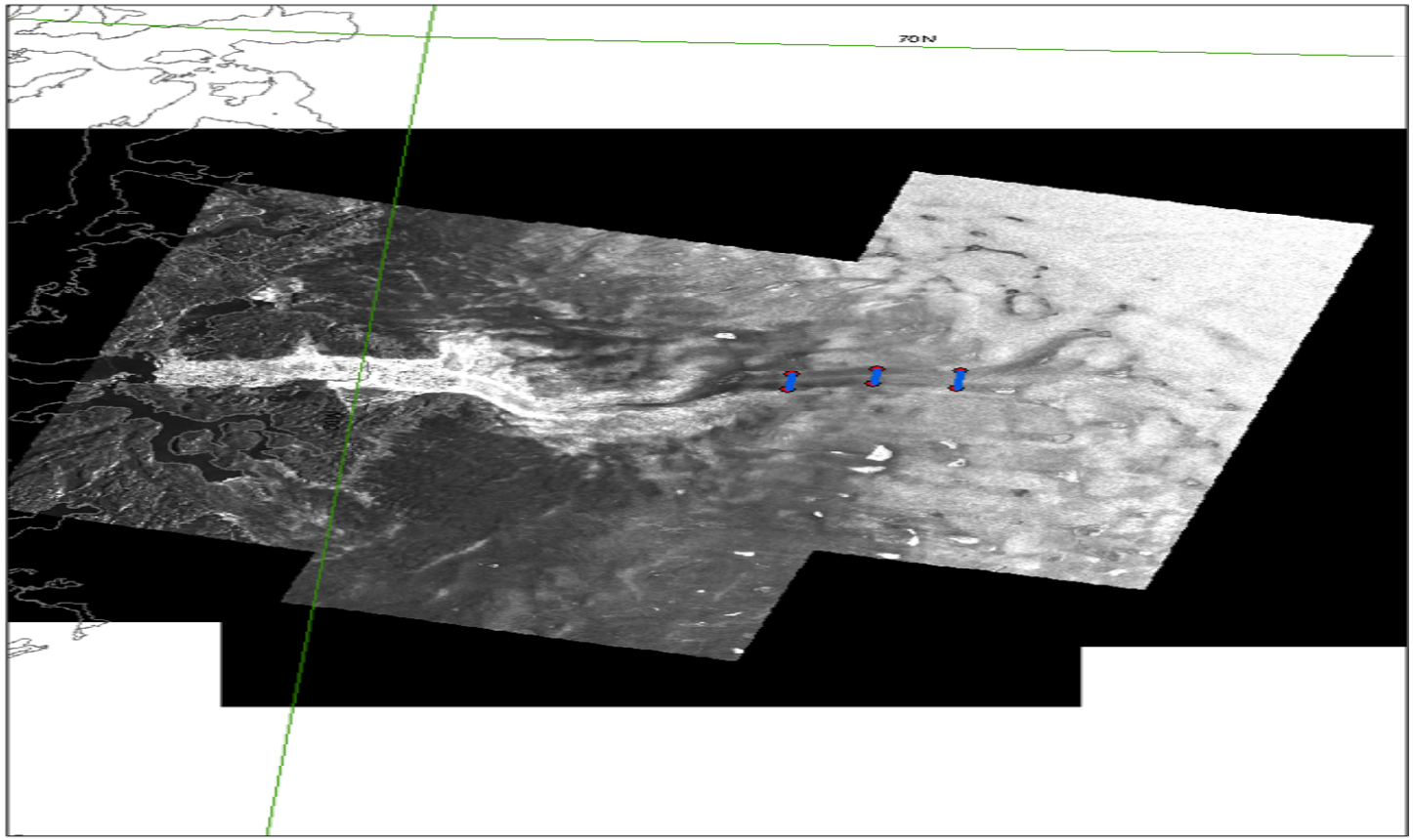

Figure 5.27: Jakobshavn Glacier and the cross flight lines

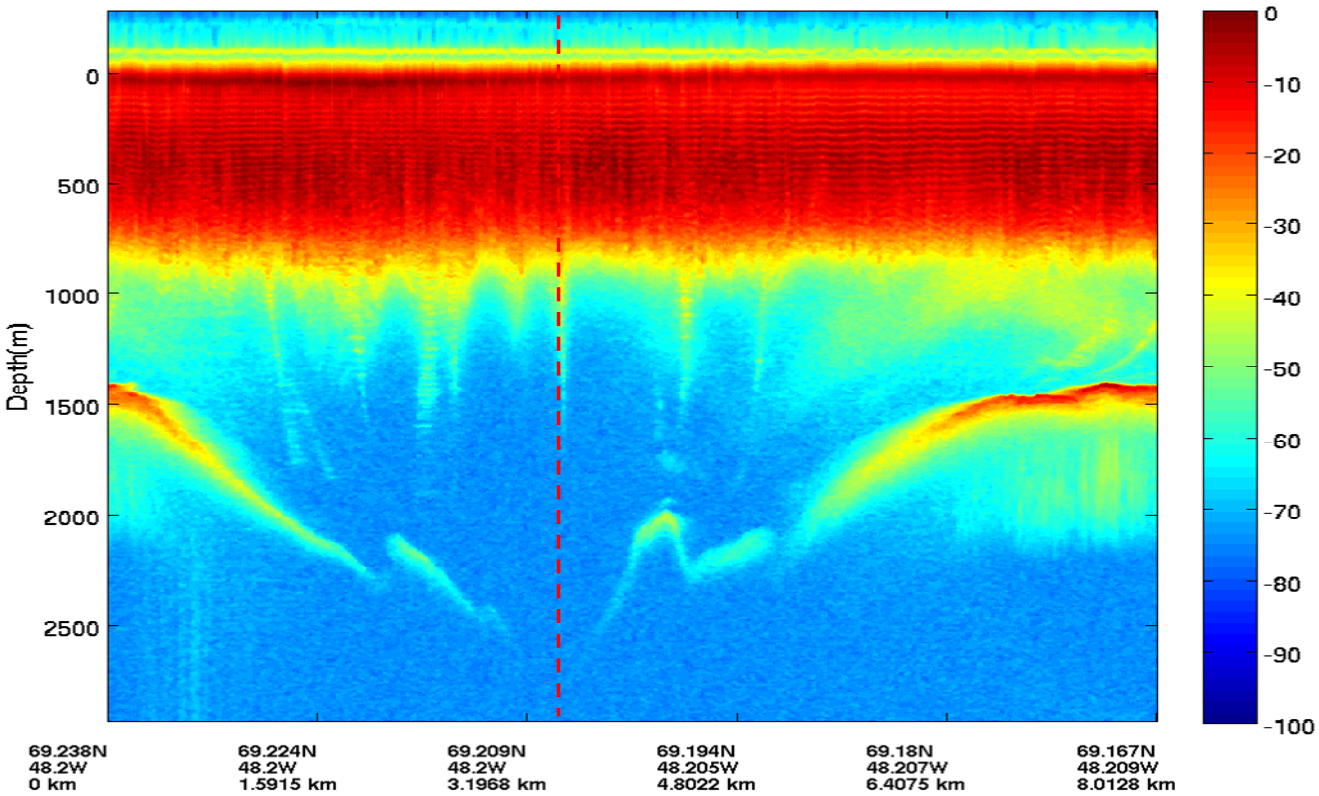

Figure 5.28: SAR Image of Cross Flight 1

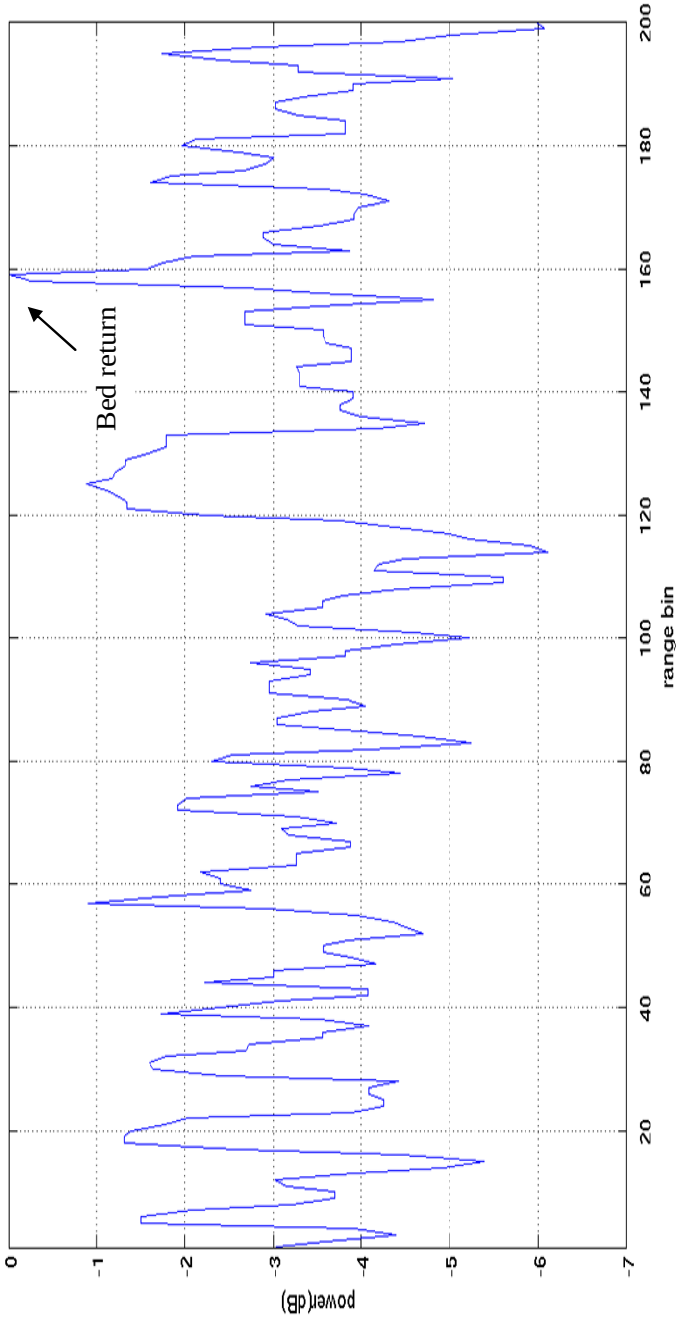

Figure 5.29: A-scope of Cross Flight 1

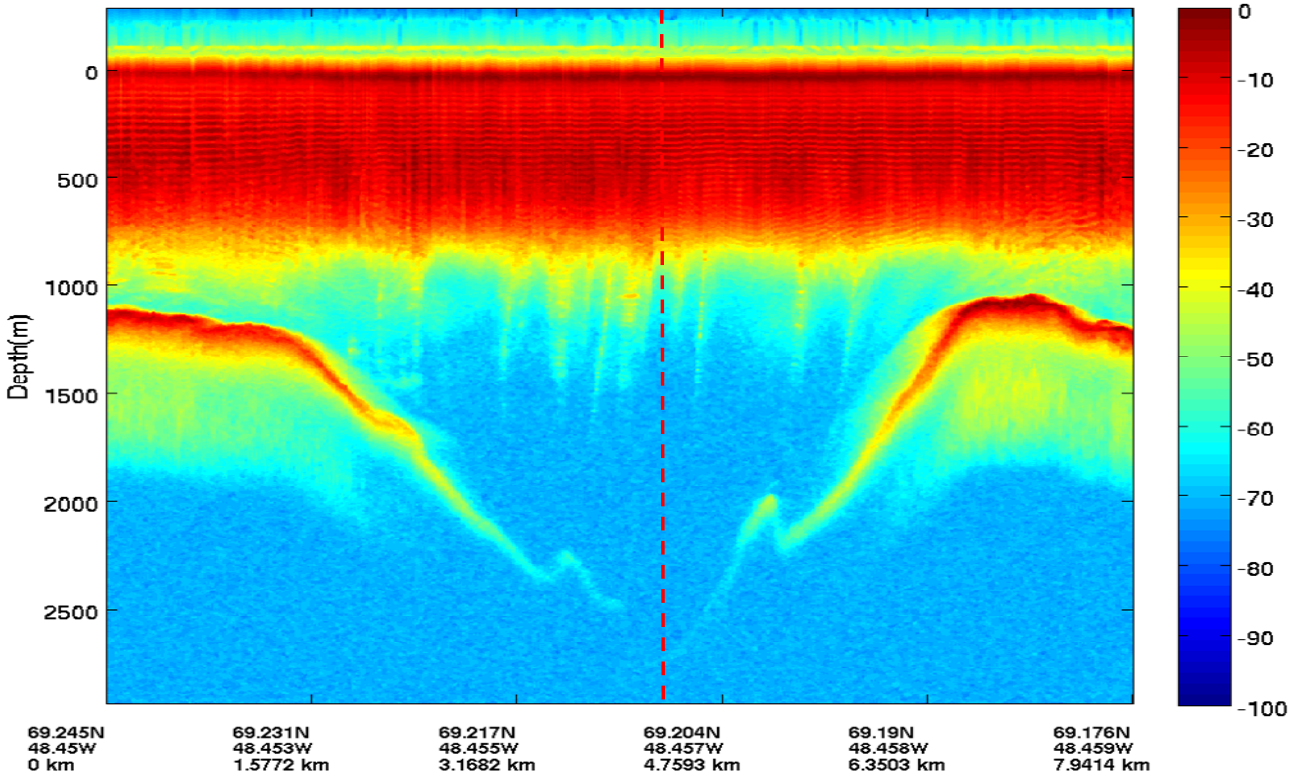

Figure 5.30: SAR Image of Cross Flight 2

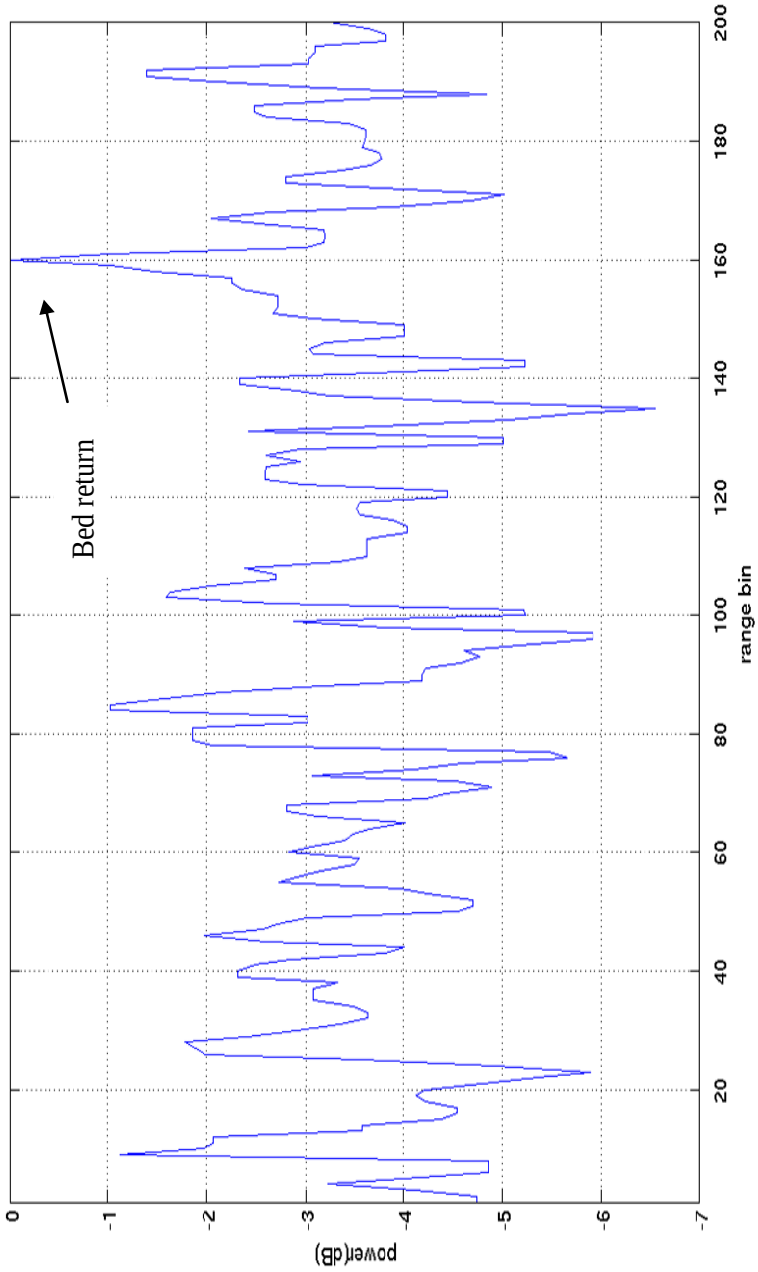

Figure 5.31: A-scope of Cross Flight 2

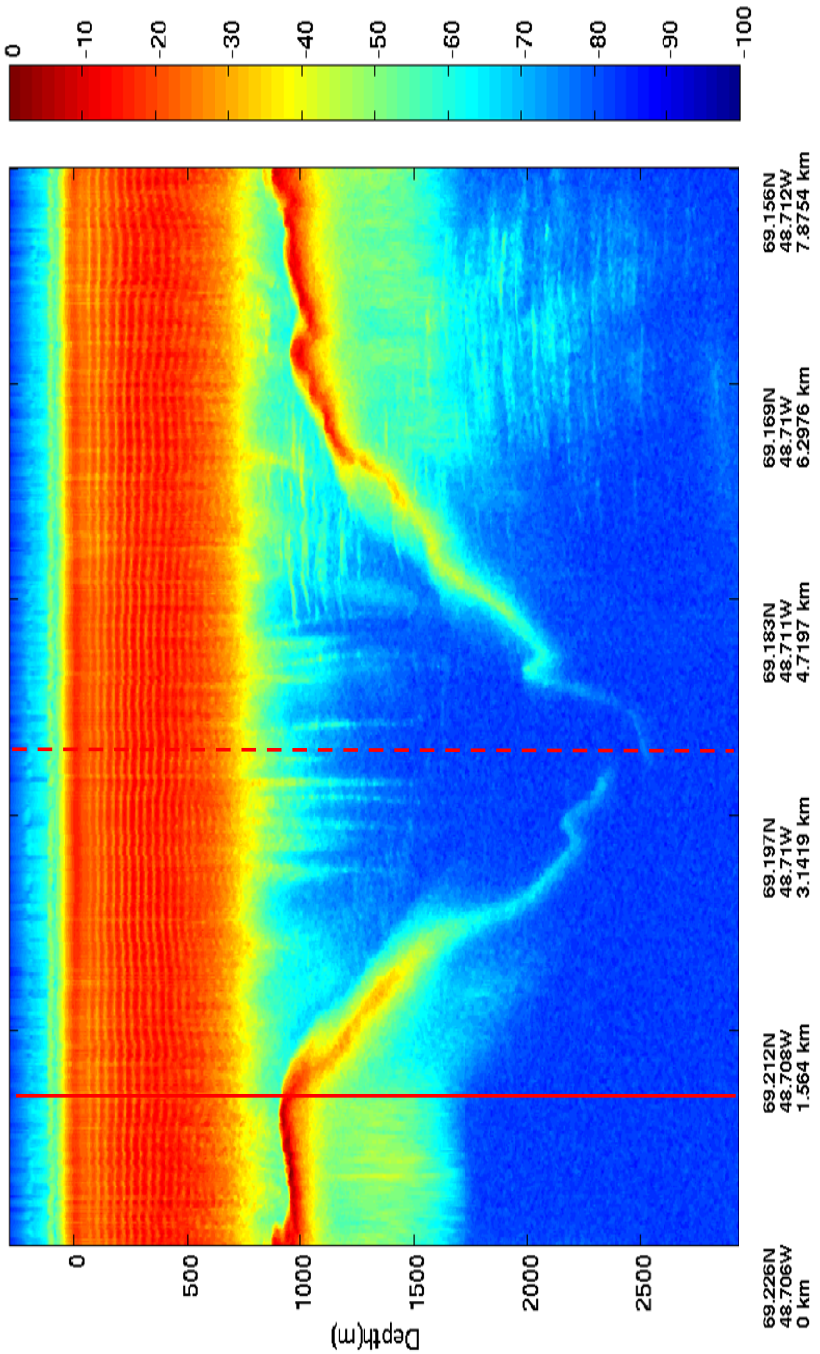

Figure 5.32: SAR Image of Cross Flight 3

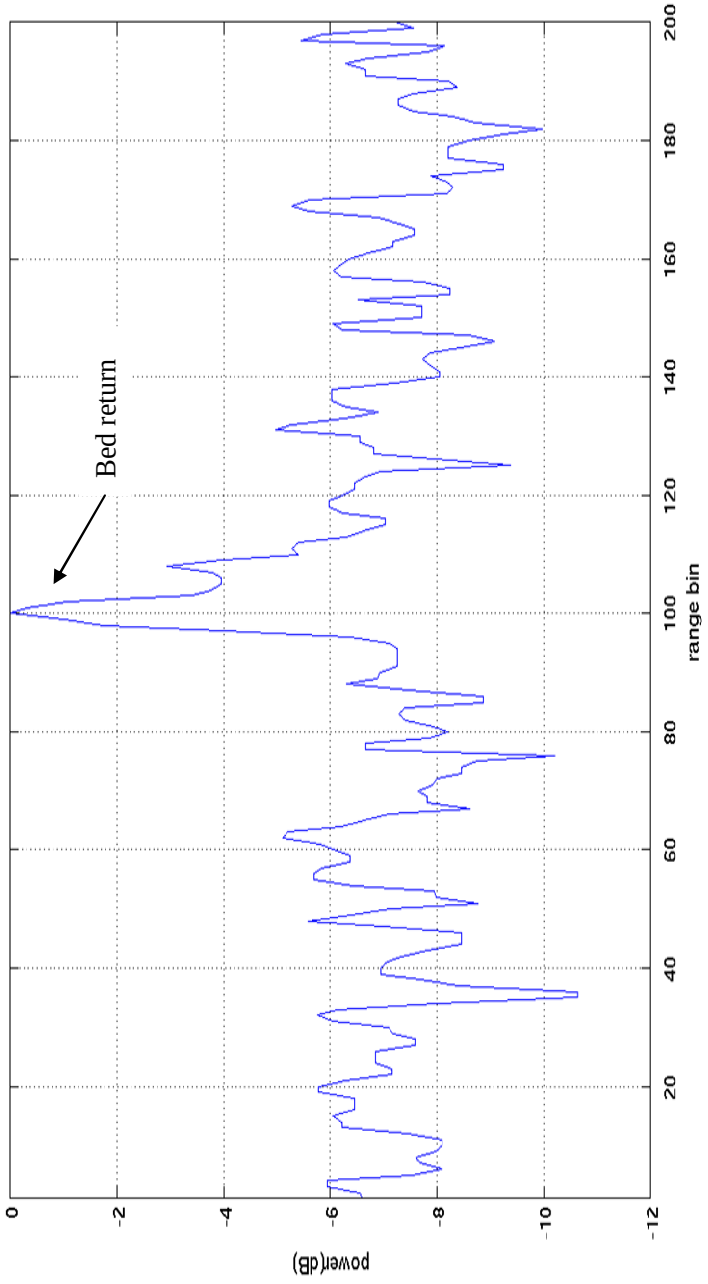

Figure 5.33: *A*-scope of Cross Flight 3

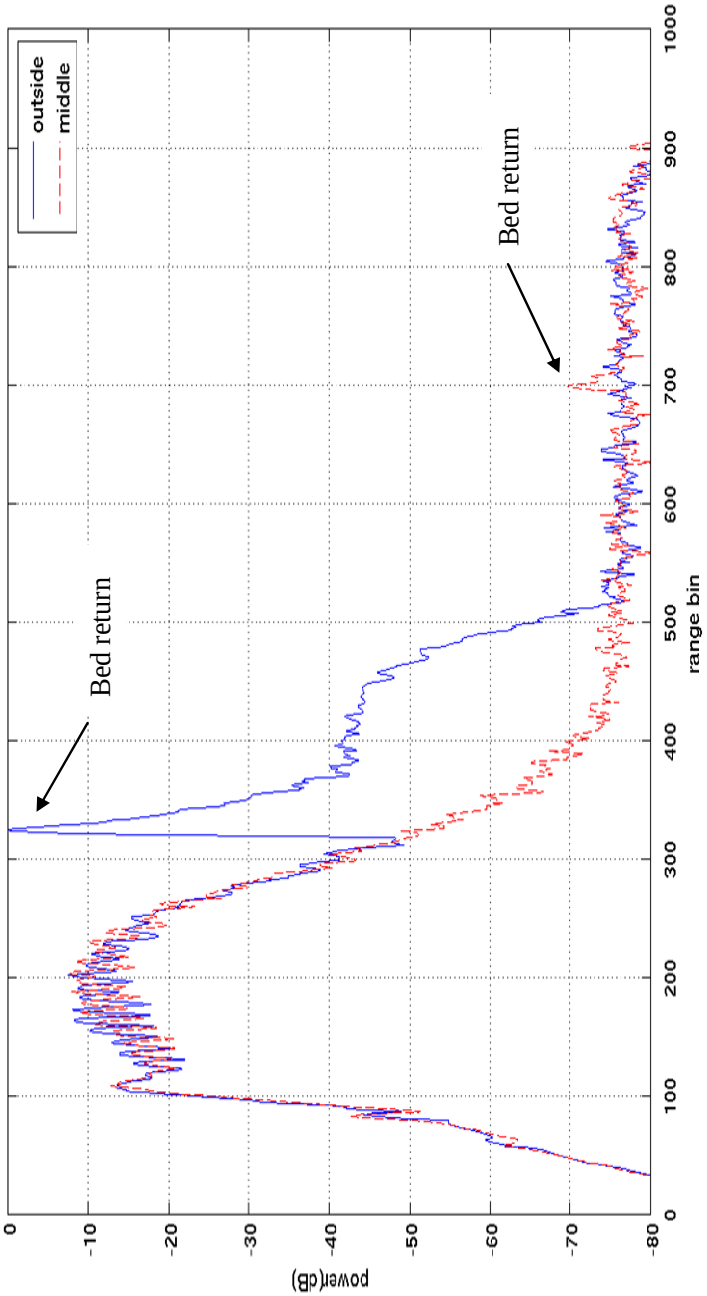

Figure 5.34: A-scope Comparison of Cross Flight 3

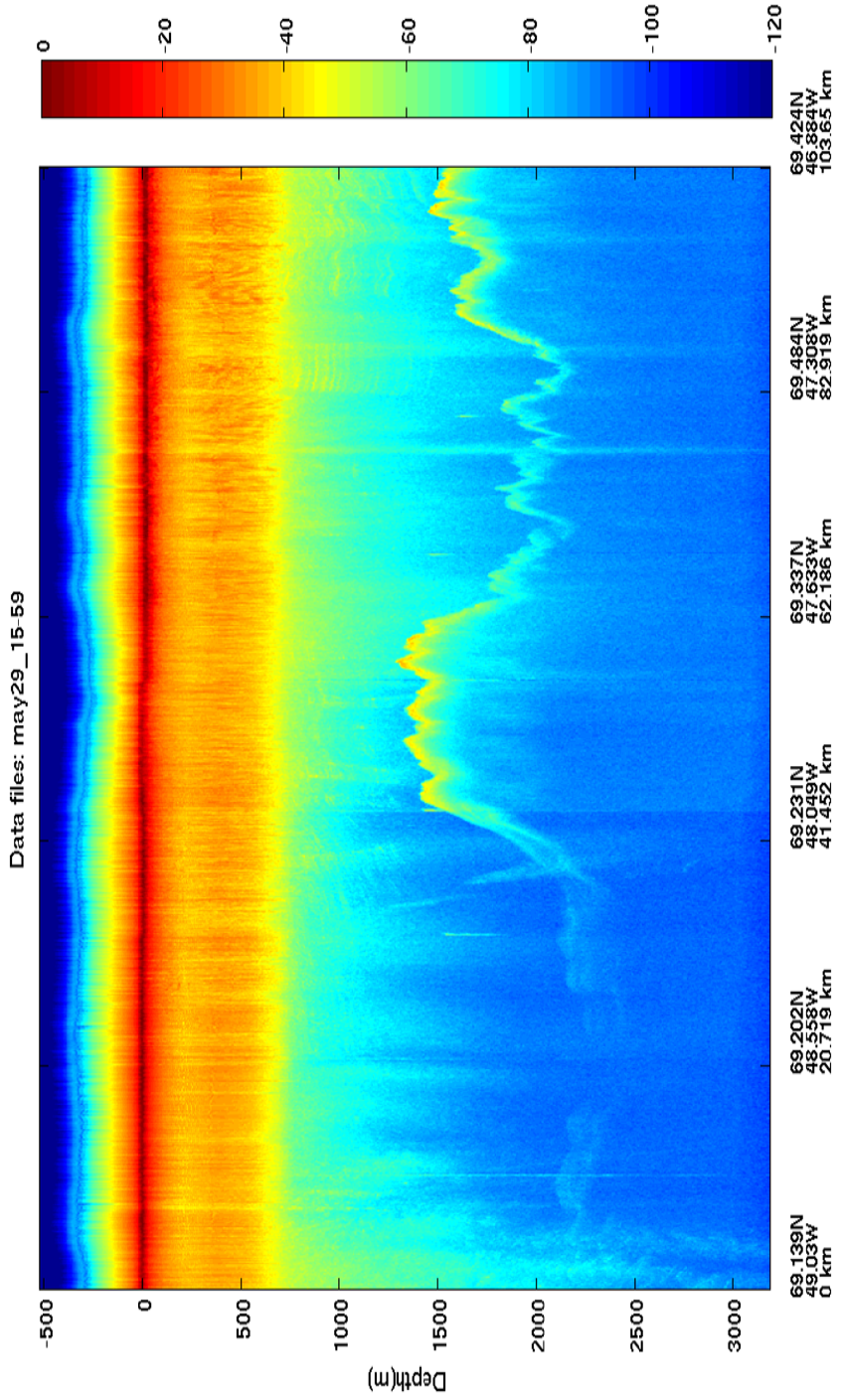

Figure 5.35: SAR Image of Along-Channel Flight

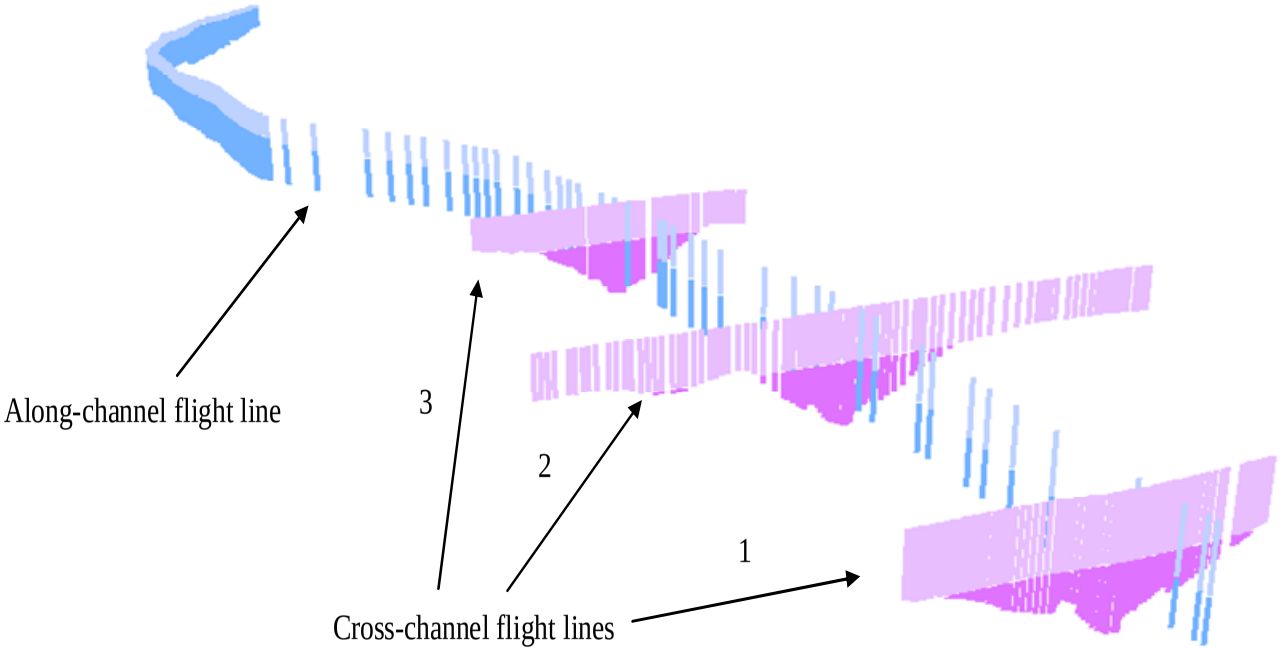

Figure 5.36 Jakobshavn Ice Thickness Profile

Chapter 6: Ice Surface Clutter Reduction

6.1 Introduction

Ice-sounding radars usually have a widebeam antenna pattern because they use VHF/UHF frequencies to achieve deep penetration into ice. Although the direction of measurement is at nadir, part of the transmitted energy illuminates ice surface at large incidence angles. When the surface is smooth, this energy is reflected away from radar receivers in the specular direction. When the surface becomes rough, some of the energy is backscattered toward the receivers and this backscattered signal can mask weak echoes from the internal layers and ice bed that arrive at the same time at the receivers. These undesired off-nadir signals are called clutter.

Across-track clutter is a big limiting factor in sounding outlet glaciers since the ice surface is heavily crevassed as shown in Figure 1.3 and Figure 1.4 in Chapter 1. In radar echograms, strong along-track ice surface clutter often forms slant streaks when the airplane is either approaching or leaving the clutter source. Because of this aircraft motion, the along-track clutter has Doppler shift and thus can be easily removed by Doppler or SAR processing. On the other hand, across-track clutter does not have Doppler shift, one has to make use of other techniques suppress it. In reference [78], two methods are used together to remove the surface clutter in the data collected by an incoherent-pulsed airborne radar at the Dry Valleys, Antarctica. The first method simulates surface echoes using aircraft position, the modeled radar

antenna pattern and the surface digital elevation model (DEM). The simulated data are compared with measured data to identify echoes from the surface. The second method migrates significant echoes in the radar data to surface and maps them onto both the DEM and optical imagery to identify candidate surface returns. These methods are critically dependent on having a good model of surface topography and are not applicable to outlet glaciers because the crevassed surface changes over time. Reference [79] proposes a repeat-pass method for a P-band space-borne radar to suppress ice surface clutter. This method uses the geometry of several passes to synthesize a sparse array and puts nulls in the direction of clutter. The method requires parallel flight paths, which are very difficult to be guaranteed for airborne radars. Reference [80] comes up with a concept of interferometric filtering for clutter reduction based on the fact that the basal fringes in the near-nadir direction vary much faster with cross-track distance than fringes from the clutter generated at large cross-track distances. Raney suggests the use of polarimetric selectivity for suppressing cross-track clutter in a sounding radar in two ways: (1) transmitting full-beam circular polarization and separating the desired signal of interest from the clutter based on the different signal and clutter polarizations, and (2) transmitting and receiving circular polarization at the radar's nadir and elliptical polarization at the radar's off-nadir regions and filtering out the elliptical polarization [81].

Since MCRDS radar uses a small linear-array for cross-track ice clutter suppression, Reference [82] studied two beamforming techniques based on linear

array theory. The first is the data-dependent Minimum Variance Distortionless Response (MVDR) method and the second is a data-independent null-steering method in which the DOAs (direction of arrival) of surface clutter from left and right are assumed known for a given depth and two nulls are placed in the DOAs to cancel the clutter. It is found the MVDR method works well when good estimate of clutter DOAs can be obtained from data statistics. High clutter-to-noise ratio or enough number of array elements is required to get a good estimate of clutter DOAs. However, for weak echoes of deep layers or regions of outlet glaciers where the ice bed echoes are very weak, even weak clutter can mask the desired signals. In addition, the number of array elements is limited by the aircraft wingspan for airborne radar. In order to make the data-independent method work, careful aircraft motion compensation and channel equalization must be performed to ensure deep nulls and accurate null placements.

This chapter will firstly briefly describe the beamforming theory of linear array, presents some results from applying the above two clutter suppression methods and then describes a beam-spaced clutter suppression method that does not need to accurately estimate clutter DOAs and null placements. This method uses beamforming techniques to estimate the clutter power profile from data and then remove the clutter by subtracting it from the data. This method works in many clutter scenarios.

6.2 Beamforming Theory of Linear Array

Consider a linear-array of N identical elements with uniform spacing d along y-axis as shown in Figure 6.1. Assume the array is in the far field of sounding targets, so the signals from targets can be thought as plane wave fronts impinging on the array. For a homogeneous media, the wavefront from a target at direction θ arrives at the N th element first and the first element last. The progressive phase lead of the n th element with respect to the $(n-1)$ th element 1 is

$$\phi = kd \sin\theta \tag{6.1}$$

where k is the wave number. The angle θ is called the direction of arrival (DOA) in beamforming theory.

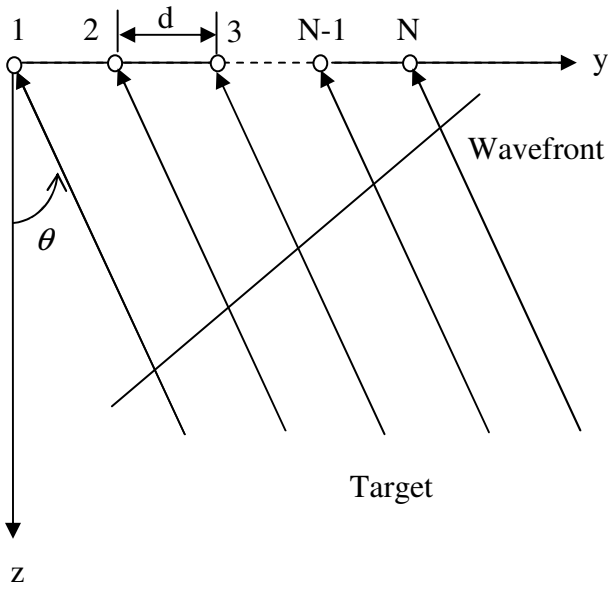

Figure 6.1: Geometry of Linear Array

According to antenna theories [83], the field of the array can be written as the multiplication of the field of the first element and the array factor, which is

$$AF = \sum_{n=1}^{N} e^{j(n-1)\phi} = e^{j(N-1)\phi/2} \frac{\sin(N\phi/2)}{\sin(\phi/2)} = e^{j(N-1)kd\sin\theta/2} \frac{\sin(Nkd\sin\theta/2)}{\sin(kd\sin\theta/2)} \quad (6.2)$$

The power gain of the array is the square of the array factor.

The element spacing of a linear-array has to be small enough to avoid grating lobes and aliasing signals. It can be observed from the above equation that the array factor has maximums equal to N when $kd\sin\theta/2 = \pm m\pi$ or $\sin\theta = \pm m\lambda/d$, where m is an integer and λ is the wavelength. The maximum at nadir, $\theta = 0$, is the desired mainlobe and the other maximums are undesired and called grating lobes. Obviously the condition to avoid grating lobes is $d < \lambda$. From the point of view of spatial sampling [84], one can think of the linear array as sampling the wavefront at a spatial frequency of $1/d$. Since the spatial frequency of the wavefront along the array is $\sin\theta/\lambda$, similar to Shannon's theorem for discrete-time sampling, in order to avoid aliasing the spatial sampling frequency has to satisfy $\frac{1}{d} \geq 2\frac{\sin\theta}{\lambda}$ which reduces to $d \leq \lambda/2$ for $-90^\circ \leq \theta \leq 90^\circ$. Since smaller spacing than $\lambda/2$ only provides redundant information and conflicts with the desire to have as much aperture as possible for a fixed number of array elements, the spacing of a linear array is generally set to $\lambda/2$.

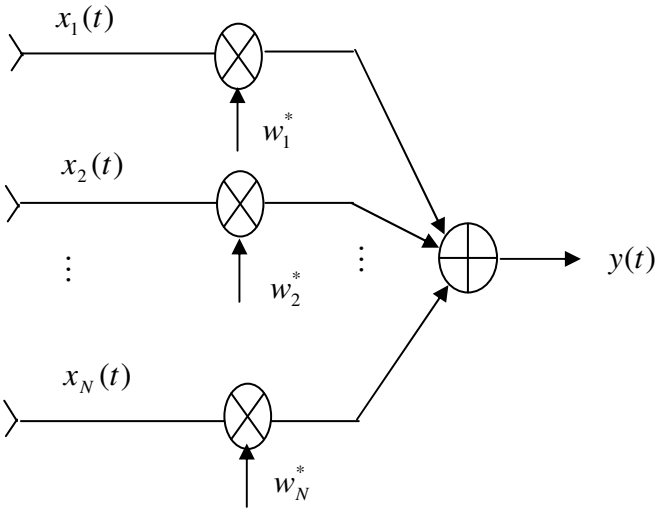

Figure 6.2: Beamforming Operations

Figure 6.2 illustrates the basic operations of beamforming where signals from each element $x_1(t)$, $x_2(t)$,…, $x_N(t)$ are multiplied respectively by complex weights $w_1^*, w_2^*,\ldots, w_N^*$ and summed to form the array output $y(t)$. The complex weights are determined in such a way that the signals from a particular direction of interest are emphasized and the ones from other directions are suppressed. Thus a beamformer can be thought as a spatial filter similar to a frequency filter for temporal signals. In vector notation, a beamformer can simply be written as

$$y(t) = \mathbf{w}^H \mathbf{x}(t) \tag{6.3}$$

where

$$\mathbf{w} = [w_1, w_2, ..., w_N]^T \tag{6.4}$$

$$\mathbf{x} = [x_1(t), x_2(t), ..., x_N(t)]^T \tag{6.5}$$

and superscripts T and H denote the transpose and complex conjugate transpose of a vector or matrix. For a linear-array, the steering vector to the direction of interest, θ, is defined as

$$\mathbf{S}(\theta) = [1, e^{j\phi}, e^{j2\phi}, ..., e^{j(N-1)\phi}]^T \tag{6.6}$$

and the beamformer response is

$$g(\theta) = \mathbf{w}^H \mathbf{S}(\theta) \tag{6.7}$$

The square of the response magnitude $\left|g(\theta)\right|^2$ is known as the beam pattern, which is usually used to evaluate the performance of a beamformer.

From simple to complex, there are three commonly used beamforming techniques: 1) conventional beamformer; 2) null-steering beamformer; 3) optimal beamformer [85]. A conventional beamformer steers the array in a particular direction θ_0 known as look direction and its mean output power is the same as the signal power from the look direction. The weights of conventional beamformer is

$$\mathbf{w} = \frac{\mathbf{S}(\theta_0)}{N} \tag{6.8}$$

where $\mathbf{S}(\theta_0)$ is the steering vector to the look direction. Obviously the weights of conventional beamformer have equal magnitude. A null-steering beamformer has a unity response in the look direction θ_0 and places zero response at clutter or interferer directions $\theta_1, \theta_2, \ldots, \theta_k$. This property can be written in the following simultaneous equations:

$$\mathbf{w}^H C = \mathbf{g} \tag{6.9}$$

where C is the steering matrix and $\mathbf{g}$ is the response vector

$$C = [\mathbf{S}(\theta_0), \mathbf{S}(\theta_1), ..., \mathbf{S}(\theta_k)], \qquad k \leq N - 2 \tag{6.10}$$

$$\mathbf{g} = [1, 0, ..., 0]^T \tag{6.11}$$

The weight vector of the null-steering beamformer is obtained by solving equation (6.9) and turns out to be:

$$\mathbf{w}^H = \mathbf{g}^T C^H (CC^H)^{-1} \tag{6.12}$$

The objective of an optimal beamformer is to maximize the signal-to-interference-plus-noise ratio (SINR). The optimal weights are of the following form:

$$\mathbf{w} = \alpha \mathbf{R}_{i+n}^{-1} \mathbf{S}(\theta_0) \tag{6.13}$$

where $\mathbf{R}_{i+n}$ is the interference-plus-noise correlation matrix, α is a constant that can be set to satisfy some constraint. When the look-direction distortionless response constraint

$$\mathbf{w}^H \mathbf{S}(\theta_0) = 1 \tag{6.14}$$

is imposed, the optimal beamformer is known as MVDR beamformer which has been discussed in Chapter 4. Substituting equation (6.13) in (6.14), it can be derived that

$$\alpha = \frac{1}{\mathbf{S}^H(\theta_0) \mathbf{R}_{i+n}^{-1} \mathbf{S}(\theta_0)} \tag{6.15}$$

The optimal weights for MVDR beamformer are obtained by substituting the above equation in (6.13):

$$\mathbf{w} = \frac{\mathbf{R}_{i+n}^{-1}\mathbf{S}(\theta_0)}{\mathbf{S}^H(\theta_0)\mathbf{R}_{i+n}^{-1}\mathbf{S}(\theta_0)} \tag{6.16}$$

6.3 Ice Clutter Reduction Algorithms

Three clutter reduction algorithms have been studied at CReSIS based on beamforming theories: 1) data-dependent MVDR algorithm, 2) data-independent null- steering algorithm and 3) clutter-power estimation algorithm. Chapter 4 presents the FMV algorithm for RFI suppression, an implementation of MVDR algorithm in frequency domain. The implementation can be used the same way for ice clutter suppression. Therefore this section will only present the implementation of the second and the third algorithms.

6.3.1 Data-Independent Null-Steering Algorithm

The detail implementation of the data-independent null-steering algorithm given here is complimentary to the discussion by Chandini [82]. The clutter scenario is illustrated in Figure 6.3, in which the desired nadir echo 2 and the undesired surface echoes from 1 and 3 arrive at the receiver simultaneously. When the power of signals from 1 and 3 is stronger than 2, the clutters will mask the signals from nadir. The null steering method assumes the DOA of ice surface clutter be calculated according to

$$\theta = \pm\cos^{-1}(\frac{h}{R}) \tag{6.17}$$

where h is the aircraft height above the ice surface, and R is the range of the ice surface clutter on both sides to the receiver. This range is equal to the equivalent range from the ice bed to the receiver that consists of two components:

$$R = h + \sqrt{\varepsilon_{ice}}\, d \tag{6.18}$$

where d is the ice bed depth and ε_{ice} is the dielectric constant of ice.

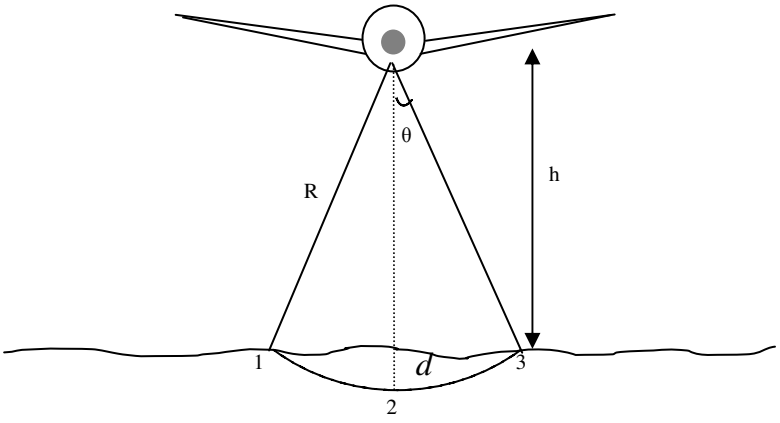

Figure 6.3: Illustration of Surface Clutter

After the array data matrix $X(L,M,N)$ (L,M,N are the numbers of range bins, along track snapshots and array elements) has gone through SAR processing with motion compensation and channel equalization, the procedures of the null steering algorithm are:

1) Starting from the a range bin i_0 which is either at the ice surface or at some depth below the surface, calculate the range R and DOA of ice surface clutter for each deeper range bins using equations (6.17) and (6.18)

$$R_i = h + \sqrt{\varepsilon_{ice}}\, d_i \tag{6.19}$$

$$\theta_{i\pm} = \pm\cos^{-1}(\frac{h}{R_i}) \tag{6.20}$$

where $i = i_0, i_0 + 1, ..., L$.

2) Calculate the optimal weights using equations (6.1), (6.6) and (6.10) ~ (6.12)

$$C_i = [\mathbf{S}(0), \mathbf{S}(\theta_{i-}), \mathbf{S}(\theta_{i+})], \tag{6.21}$$

$$\mathbf{w}_i^H = \mathbf{g}^T C_i^H (C_i C_i^H)^{-1} \tag{6.22}$$

3) Combine the array data with the optimal weights for each range bin

$$Y(i,:) = \sum_{i=i_0}^{L} \sum_{j=1}^{M} \mathbf{w}_i^H X(i,:,j) \tag{6.23}$$

where the colon denotes the inside summation applies to the same range bin for all snapshots.

6.3.2 Clutter-Power Estimation Algorithm

While both the MVDR and the above data-independent null-steering algorithms are element-spaced processing where signals from each element are weighted and summed to generate the array output, the clutter power estimate algorithm presented in this section is beam-spaced processing that includes two stages as shown in Figure 6.4. The first stage is to form two beams $y_1(t)$ and $y_2(t)$ in element space. The first beam $y_1(t)$ is the main beam that is formed by choosing the weights u_1^*, u_2^* ,…, u_N^* to point the beam to nadir and with clutter partly suppressed. The second beam $y_2(t)$ is the clutter beam that is formed by choosing the weights v_1^*,

v_2^*, … , v_N^* to put a null at nadir and to have maximum gains in the direction of clutter. The second stage is to subtract the weighted clutter beam from the main beam after properly compensating for the gain difference between the two beams based on power profiles estimation. According to Brookner [86] and Gabriel [87], in situations where clutter directions are known (which is the case for ice surface clutter), the beam-spaced processing may lead to more efficient clutter cancellation. In presence

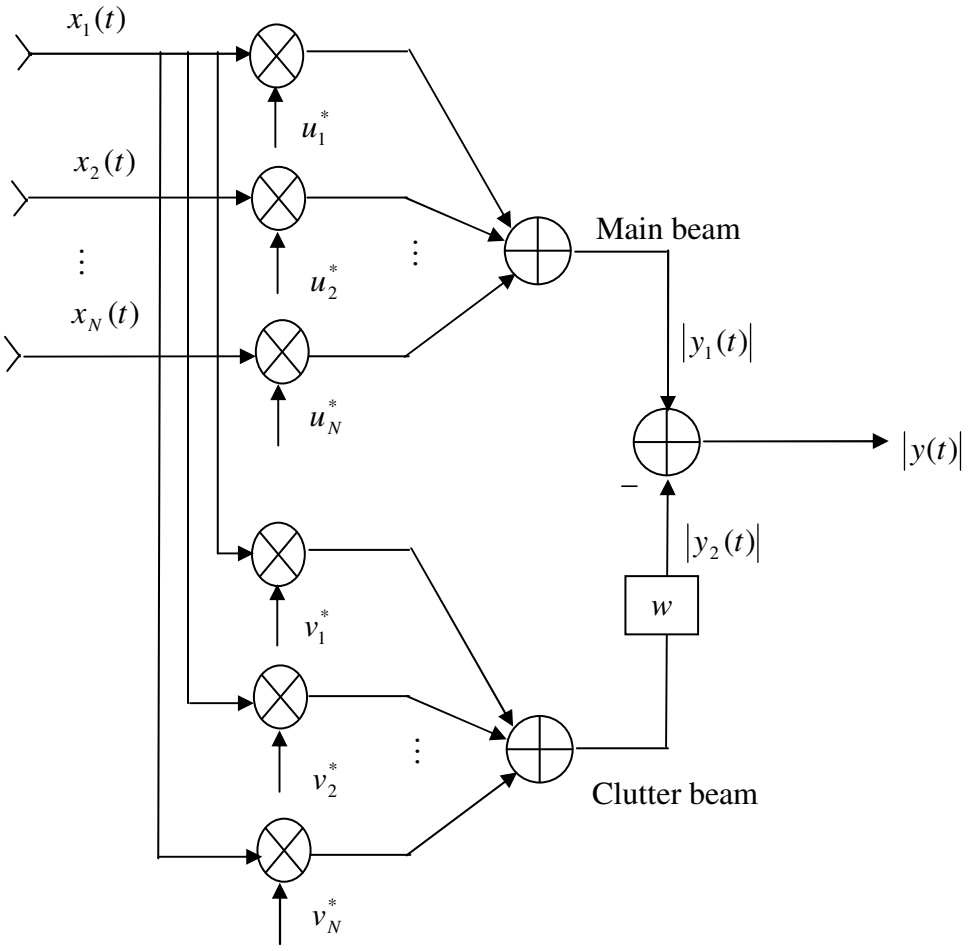

Figure 6.4: Beam-Spaced Processing

of beam pointing errors (this is the case for airborne radar arrays resulting from not completely-compensated aircraft motion, channel mismatch, mutual coupling and wing flexure, etc) beam-spaced processing is generally more robust and outperforms element-spaced processing [88].

Assuming the array data matrix $X(L,M,N)$ has gone through SAR processing with motion compensation and channel equalization, the detail implementation of the clutter power estimation algorithm are described below:

1) Form the main beam using weights determined by Hanning function

$$u_1 = h(1),\ u_2 = h(2),\ldots,\ u_n = h(N+1) \tag{6.24}$$

$$h(n) = 0.5[1-\cos(2\pi\frac{n}{N+2})],\ n = 0,1,...,N+2 \tag{6.25}$$

where the order of Hanning function is the number of array element plus 2. We discard the first and the last zero Hanning coefficients to avoid large power loss of signals since we only have a small number of array element.

2) Form the clutter beam using the null-steering beamformer described by equations (6.9) ~ (6.12). The look direction is the null direction and the nulls are placed around nadir.

3) Determine the weights applied to the clutter beam to compensate the gain difference of the main beam and clutter beam. The mean power-versus-depth profiles of the two beams are first estimated and the weights as function of depth are determined as the ratio of the two power profiles.

$$w = \sqrt{\frac{\sum_{i=1}^{M} \mathbf{u}^H X(L,i,N) X^H(L,i,N)\mathbf{u}}{\sum_{i=1}^{M} \mathbf{v}^H X(L,i,N) X^H(L,i,N)\mathbf{v}}} \tag{6.26}$$

where the summation is performed in the along-track direction.

4) Subtract the weighted clutter beam from the main beam to get the output of the beam-spaced array processing with clutter reduced.

$$|y(t)| = |y_1(t)| - w|y_2(t)| \tag{6.27}$$

6.4 Data Processing Results

6.4.1 Results of Applying FMV and Null-Steering Algorithms on Sea Ice Data

The sea ice data used in Chapter 5 to verify the SAR algorithm is also an ideal data set to test the ice-surface clutter reduction algorithms. The sea ice on both sides along the aircraft flight path can be taken as surface clutter. For FMV algorithm, the DOA of sea ice can be well estimated from the data because the reflected echoes from the sea ice are very strong. For the null steering algorithm, the DOA of clutter can be accurately computed through the known sea ice location. In addition, these targets can be used to calibrate the receiver channel mismatches.

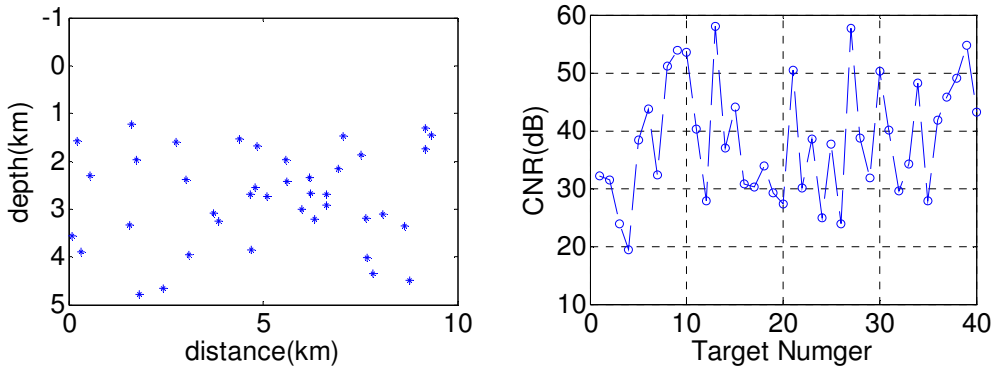

(a) (b)

Figure 6.5: Sea Ice Clutter (a) Locations; (b) Clutter-to-Noise Ratio

In the SAR image of Figure 5.23, forty pieces of high clutter-to-noise ratio (CNR) are selected as clutter targets. Figure 6.5(a) illustrates the targets locations. The horizontal axis is the along track distance and the vertical axis is the range from the sea ice to the radar receiver. Figure 6.5(b) shows the CNR of these sea ice clutter targets. The minimum CNR is 19.43dB and the maximum is 58dB. The mean CNR of the forty targets are 38.42dB.

Figure 6.6 and 6.7 are receiver channel amplitude and phase mismatches estimated from each piece of the selected sea ice, taking the first array element as the reference. According to Figure 6.6, the mean values of the amplitude mismatch are $[\, e_2 / e_1, e_3 / e_1, e_4 / e_1 \,]$ = [0.8960, 0.9842, 0.6785]. The standard deviations of the amplitude mismatch estimates are 0.047, 0.055 and 0.034 around the mean values. According to Figure 6.7, the mean values of the phase mismatch are

$[e_2 - e_1, e_3 - e_1, e_4 - e_1]$ = [-20.92, -34.74, -116.13] degrees. The standard deviations of the phase mismatch estimates are 2.26, 3.41 and 3.18 degrees around the mean values. The mean values of the amplitude and phase mismatch estimates are used in channel equalization prior to applying the clutter reduction algorithms to the sea ice data.

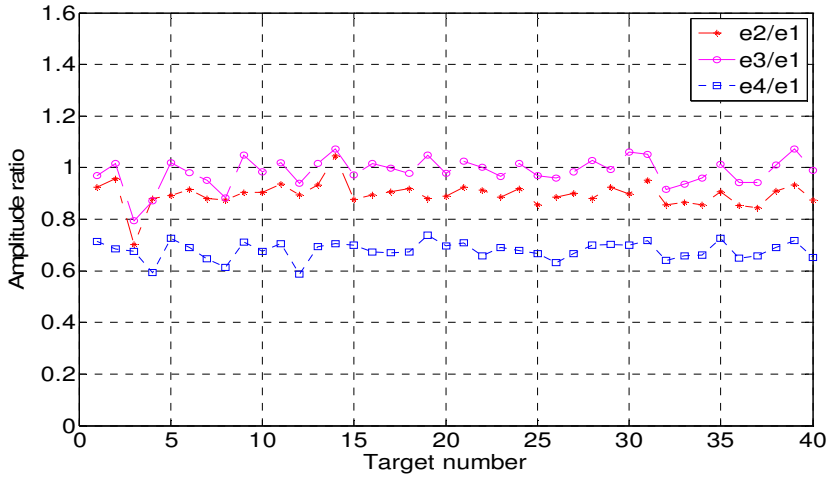

Figure 6.6: Channel Amplitude Mismatch Estimates from Sea Ice

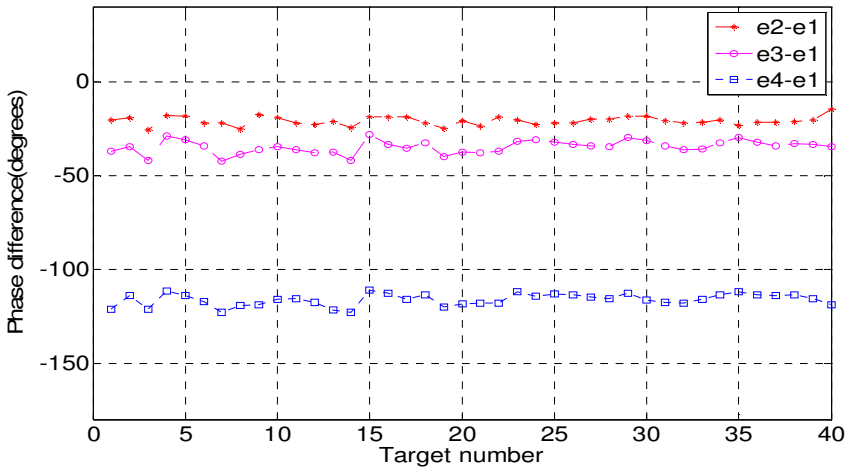

Figure 6.7: Channel Phase Mismatch Estimates from Sea Ice

Figure 6.8 shows the sea ice echogram after clutter reduction using the null steering algorithm, and Figure 6.9 is the clutter reduction result from FMV algorithm. Comparing to the echogram in Figure 5.22, the clutter reduction by both algorithms is obvious.

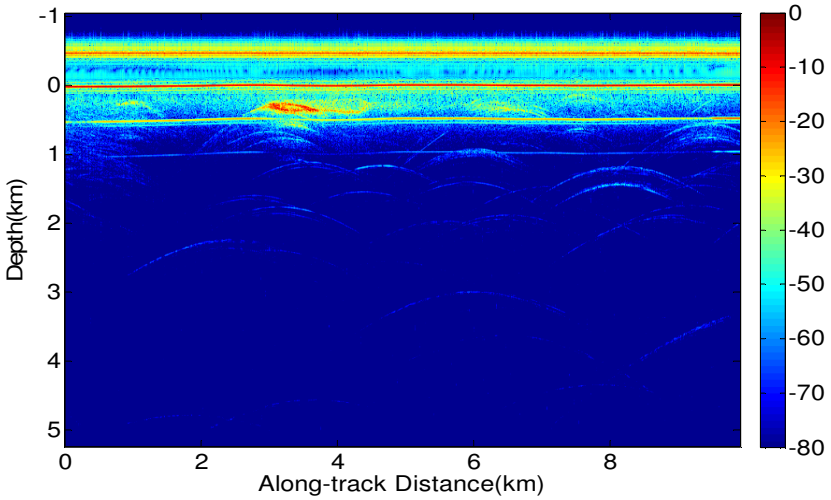

Figure 6.8: Sea Ice Echogram after Clutter Reduction by Null Steering Algorithm

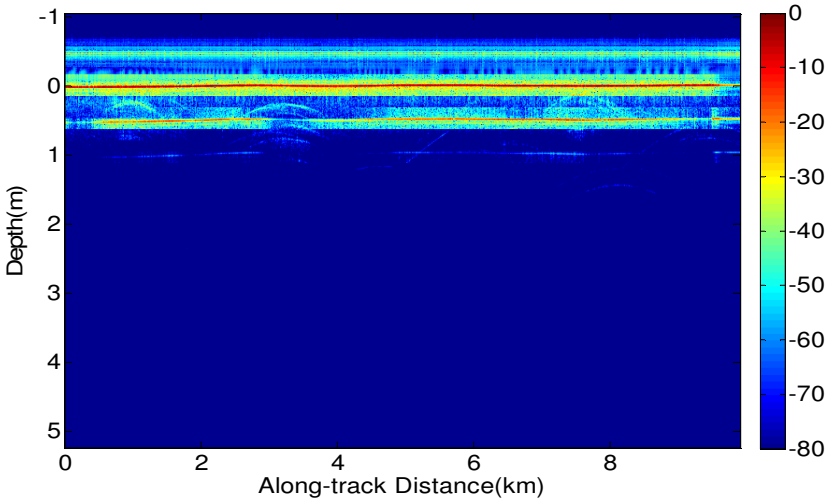

Figure 6.9: Sea Ice Echogram after Clutter Reduction by MVDR Algorithm

We evaluate the performance of a clutter reduction algorithm by comparing the clutter power of the algorithm output with that of combining the array data with uniform weights or Hanning weights. Figure 6.10 shows the receive beam patterns of MCRDS P-3 of uniform weights and Hanning weights when the four channels are identical without any mismatches. According to the beam patterns, the relative clutter power level will reduce about 12 dB and 40 dB, respectively, with uniform weights and Hanning weights when the DOA of the clutter is greater than 70 degrees.

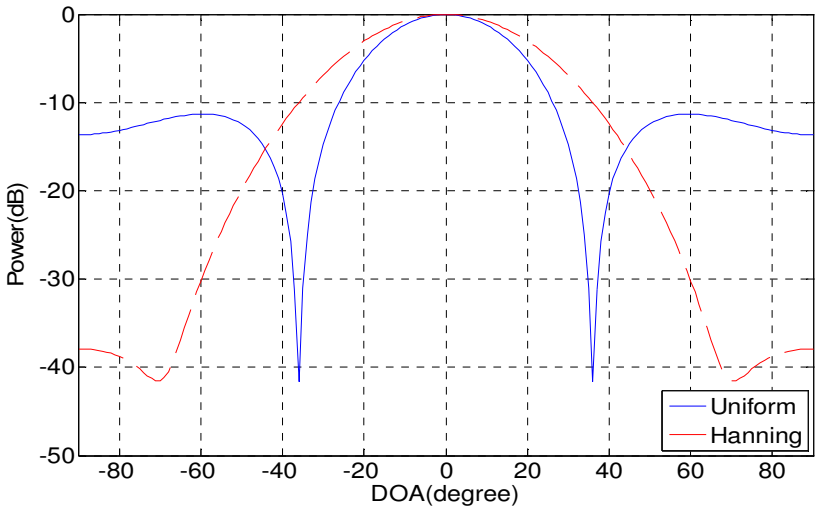

Figure 6.10: Receive Beam Patterns of MCRDS P-3 with Weighting Functions

Figure 6.11 shows the clutter reduction performance of Hanning weighting, the null steering algorithm and the FMV algorithm by plotting the power reduction for each sea ice target compared to the normalized power from uniform weighting. It turns out that the mean value of the clutter reduction is 20.58dB, 28.57dB and 34.30dB respectively by Hanning weighting, the null-steering algorithm and the FMV algorithm. The arrows pointing to the peaks in the A-scopes of Figure 6.12 indicate

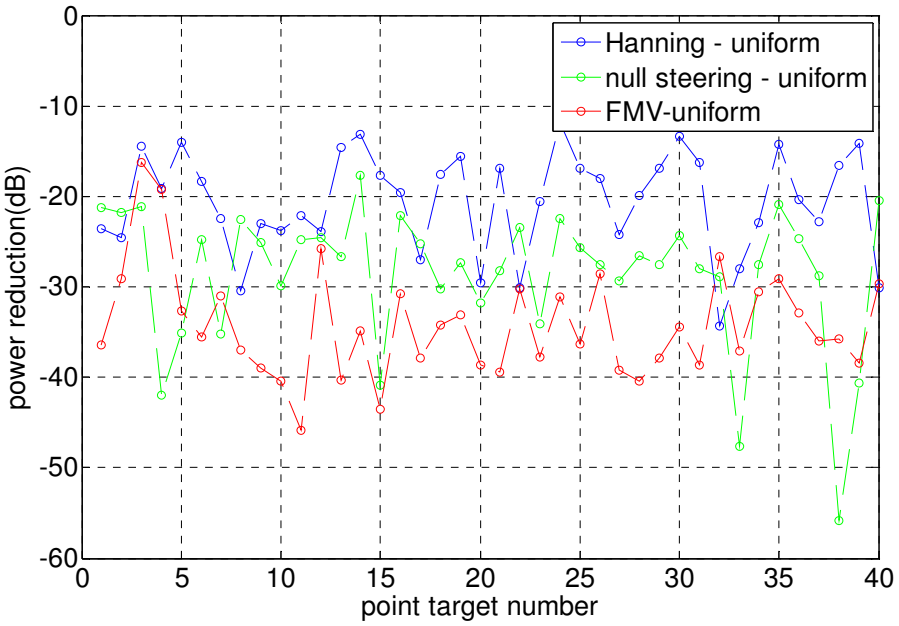

Figure 6.11: Clutter Reduction Performance of Null Steering Algorithm

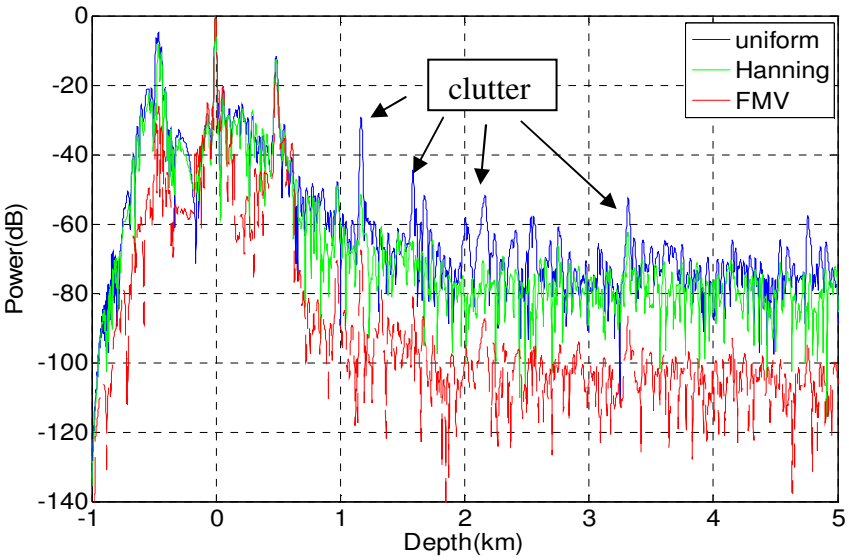

Figure 6.12: Clutter Reduction Performance of FMV Algorithm

the sea ice clutter from different DOA (different depth in the figure). This figure illustrates the power reduction of these peaks by the Hanning weighting and the FMV algorithm. The performance of Hanning weighting and the null-steering algorithm is more limited by the variations of the channel mismatches. The FMV algorithm is more effective in this case than the null-steering algorithm. The FMV algorithm uses the specular ocean surface reflection to calculate the nadir steering vector, and uses strong clutter signals to calculate the DOA. It is therefore more adaptive to the channel mismatches' variations, residual aircraft motion effects etc.

In most cases the ice clutter encountered in field survey is distributed as shown in Figure 6.16. Both the FMV and null steering algorithms are not very effective for distributed clutter. In the sea ice case, the clutter power dominates in specific directions as shown by the A-scope in blue in Figure 6.12, the FMV algorithm is able to place deep nulls in these directions according to the DOA estimation to reduce the clutter power effectively. On the other hand, for ice clutter with distributed power profile as shown by the red plot in Figure17, It is impossible for FMV to place deep nulls in all the clutter directions. In addition the weak ice bed echoes and non-specular reflection from rough ice surface prevent FVM from accurately estimating the steering vector. Without high-SNR ice surface or ice bed echoes, channel mismatches cannot be accurately estimated and the null-steering algorithm fails to form a deep null and accurately place the null at the clutter angles when channel mismatches cannot be well compensated.

6.4.2 Results of Applying Clutter-Power Estimation Algorithm on Ice Data

Figure 6.13 is a SAR image from a single element of MCRDS P-3. Most part of the ice bed in this image is masked by ice clutter. Only a short portion starting from 8km to the end is barely visible at depth of 2km. The data were collected in Greenland on Sept. 17, 2007. The file numbers are 890-894. The aircraft was flying south along a straight line from (–44˚38.5',65˚4.4') to (–44˚48.3',65˚3.9') at an average height of 1386 m. The DOA of the surface clutter at the depth of 2 km is about 73.7 degrees according to the equations (6.19) and (6.20).

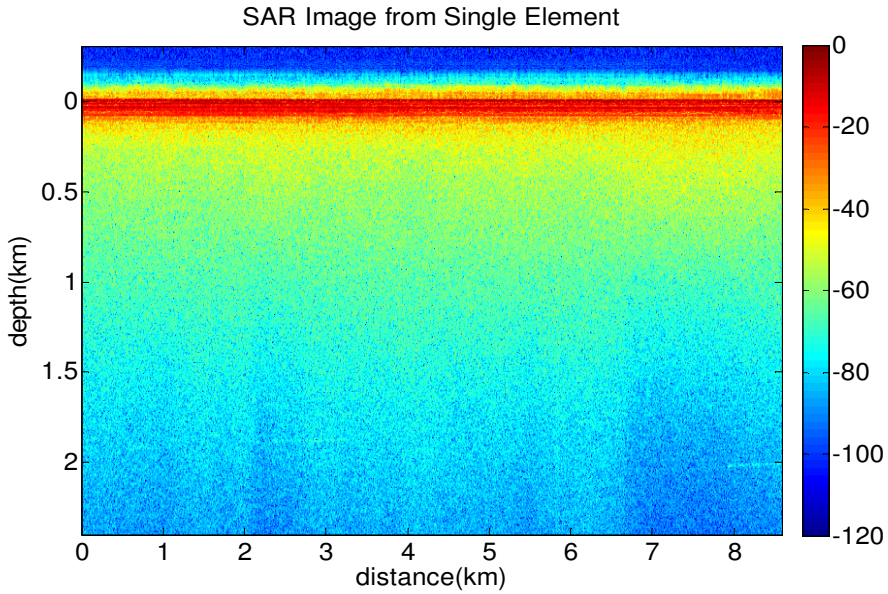

Figure 6.13: SAR Image with Ice Clutter

Figure 6.14 shows the receive beam patterns of MCRDS P-3 used in the clutter power estimation algorithm. These patterns are ideal assuming all channels are identical. The beam pattern of Hanning weighting is the same with the one in Figure

6.10, and is used to form the main beam that keeps signals from nadir and rejects clutter from both left and right sides. The beam pattern in red-dash line is obtained by setting the look direction at 60 degrees and putting two nulls at -2 and 2 degrees in equations (6.9)~(6.12). This beam pattern is used to form the clutter beam that rejects nadir signals and keeps clutter signals from angles greater than 60 degrees.

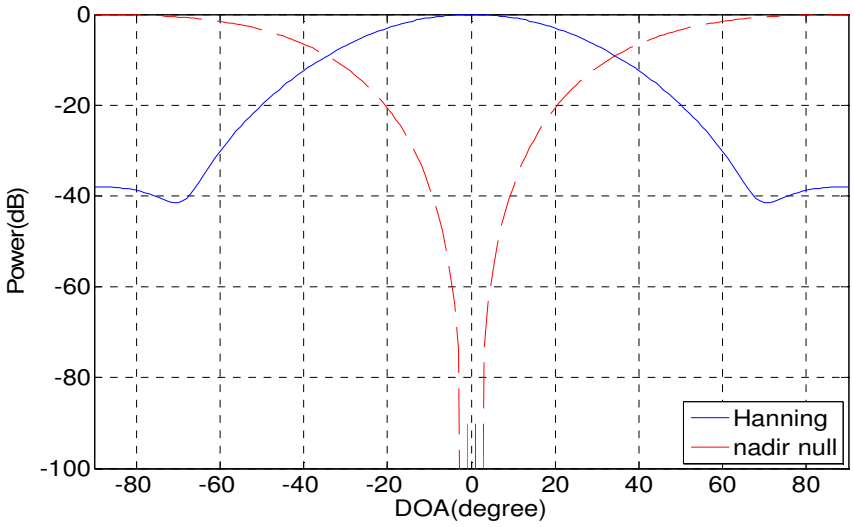

Figure 6.14: Receive Beam Patterns of MCRDS P-3

Used in Clutter Power Estimation Algorithm

Figure 6.15 shows the image of the main beam from combining the four channel data with the Hanning weighting. The clutter is reduced by about 20 dB, and some sub-surface layers and most part of the ice bed become visible. But the clutter around the ice bed is still visible. Figure 6.16 shows the image of the clutter beam after applying the beam pattern with nulls at $\pm 2^{\circ}$. It is observed that the short potion of the visible ice bed in Figure 6.13 is removed and the ice clutter is left. The

averaged power profiles are calculated for the main beam and clutter beam as show in Figure 6.17. The power profile in blue is from the main beam and the two small peaks around 2km depth are the result of ice bed echoes. The power profile in red is from the clutter beam and the ice bed signals are totally masked. The weights as a function of depth in equation (6.26) is determined as the ratio of the main power profile over the clutter power profile in Figure 6.17. The clutter beam of Figure 6.16 is then multiplied by the weights and is subtracted from the main beam of Figure 6.15 according to equation (6.27). Figure 6.18 shows the image after the beam subtraction. On average the subtraction reduces clutter by 10.3dB. The A-scopes of Figure 6.20 are from the 700th record around 2.8 km in Figure 6.15 and 6.18, and illustrate the clutter reduction compared to Hanning weighting. Finally adaptive Wiener filter is applied to reduce the additive white noise to further enhance the visibility of the ice bed as shown in Figure 6.19.

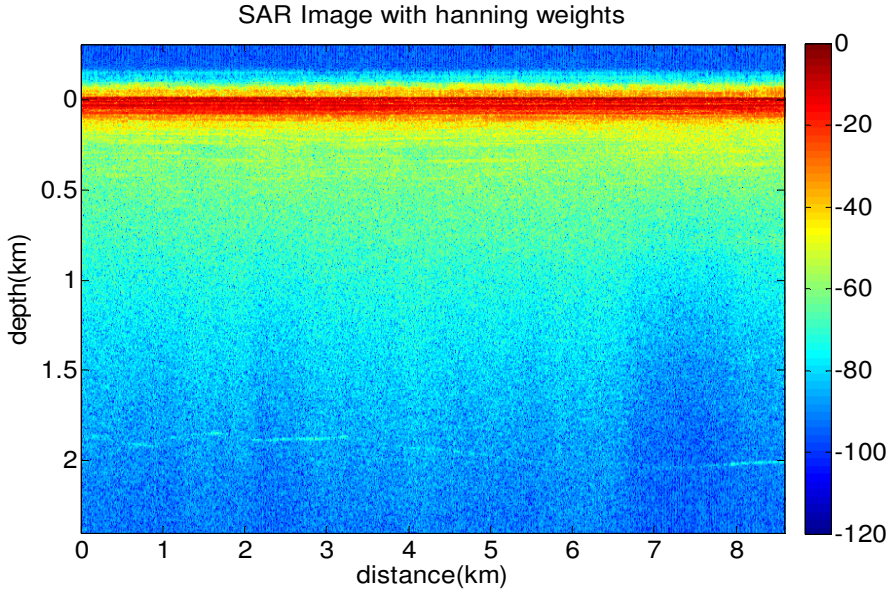

Figure 6.15: Image of Main Beam

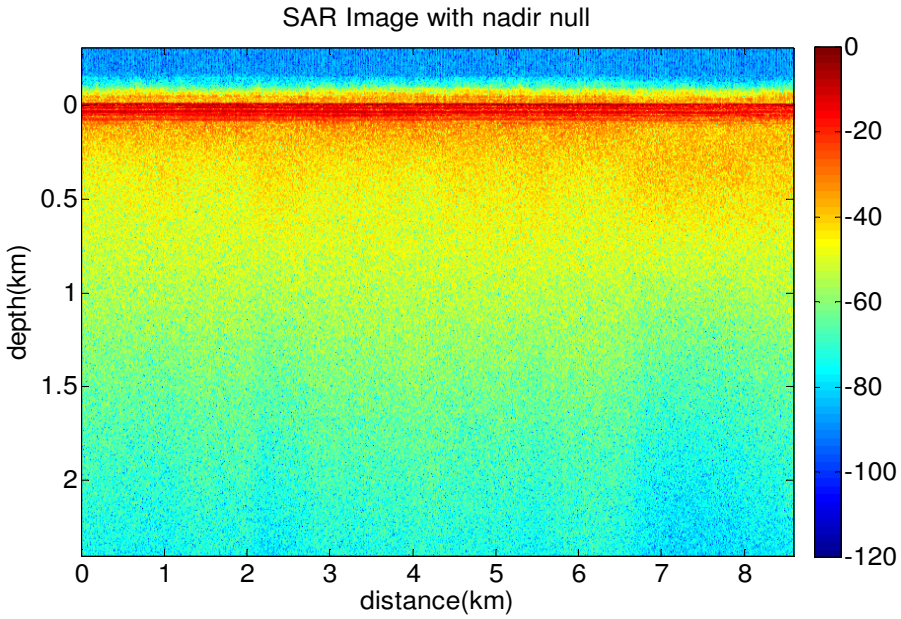

Figure 6.16: Image of Clutter Beam

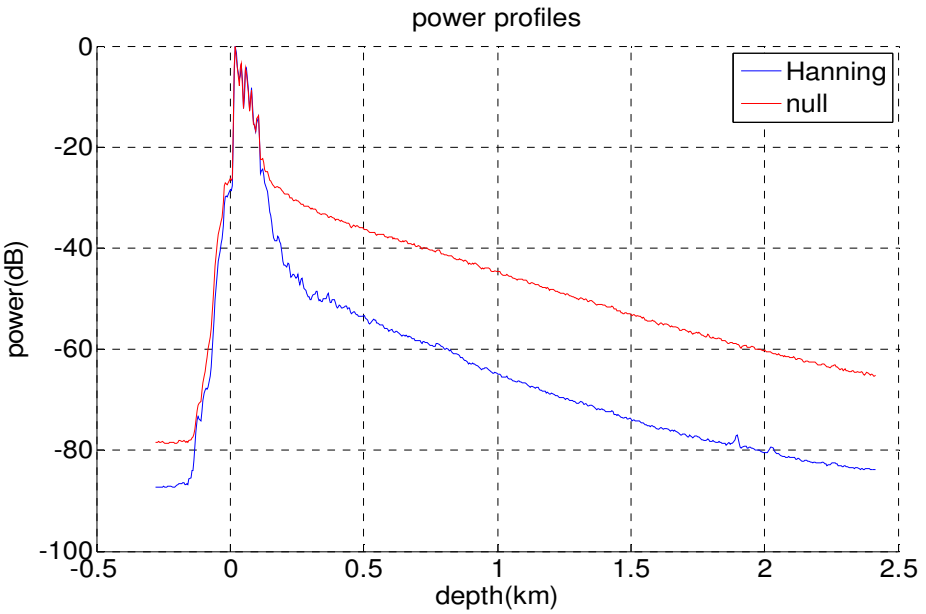

Figure 6.17: Averaged Power Profiles of Main and Clutter Beams

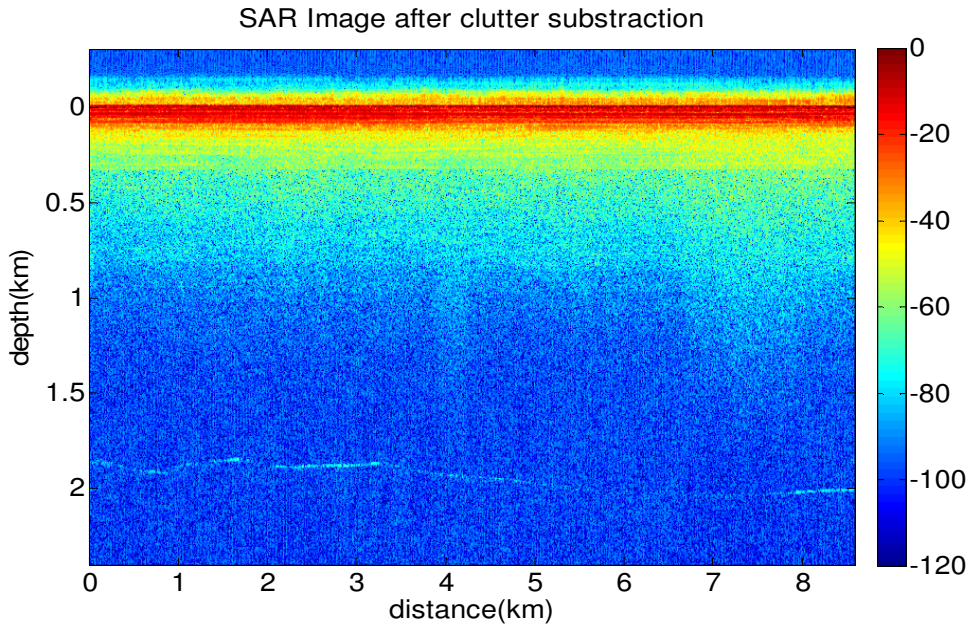

Figure 6.18: Clutter Reduction by Beam Subtraction

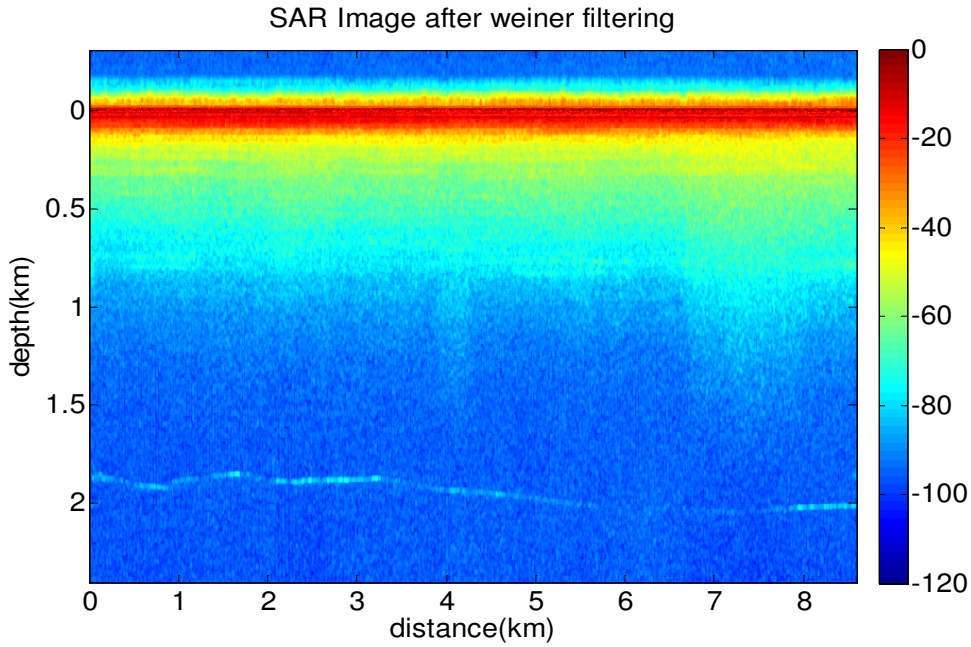

Figure 6.19: Bottom Enhancement by Wiener Filter

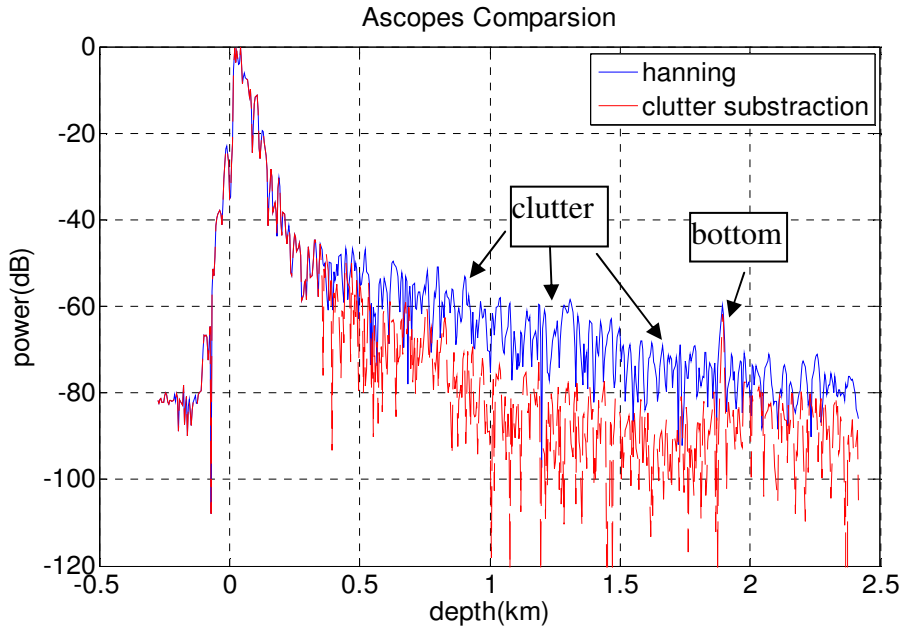

Figure 6.20: A-scope Illustration of Clutter Reduction by Beam Subtraction

Figure 6.21 shows another clutter case with the P-3 aircraft flying at a lower altitude around 550 m. The data were collected on September 23, 2007 over Greenland. The aircraft was flying south from (–38°51.3', 66°21.7') to (–39°3.1',66°21.3') . The distance is 3012 m. The file numbers are 118-119. The ice bed in this image is completely masked by ice clutter. Figure 6.22 is the result of combining the array data by the Hanning weights. The ice bed becomes barely visible at depth of around 800 m. In this case, the Hanning weighting only reduces clutter by 7.2 dB on average compared to uniform weighting. Figure 6.23 is the result of applying the clutter power estimation algorithm. The clutter is reduced further by 9.6 dB on average and the ice bed become very clear.

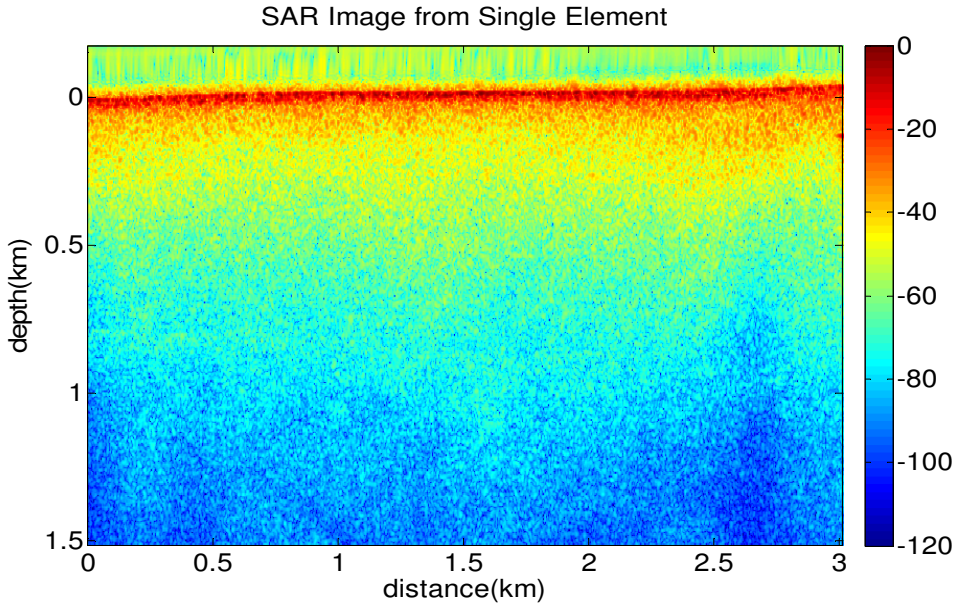

Figure 6.21: SAR Image with Ice Clutter

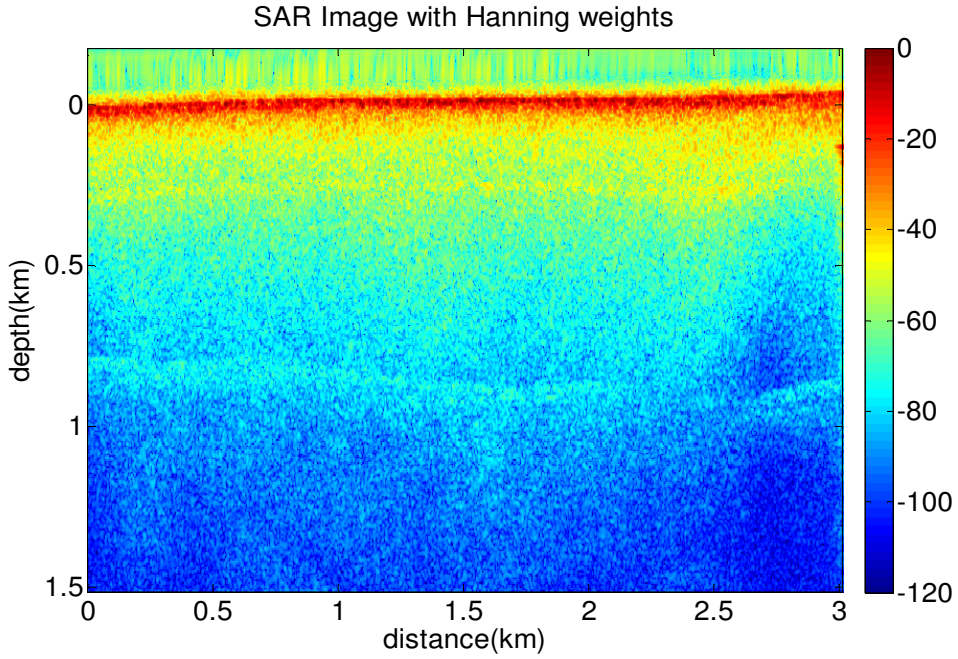

Figure 6.22: Clutter Reduction by Hanning Weighting

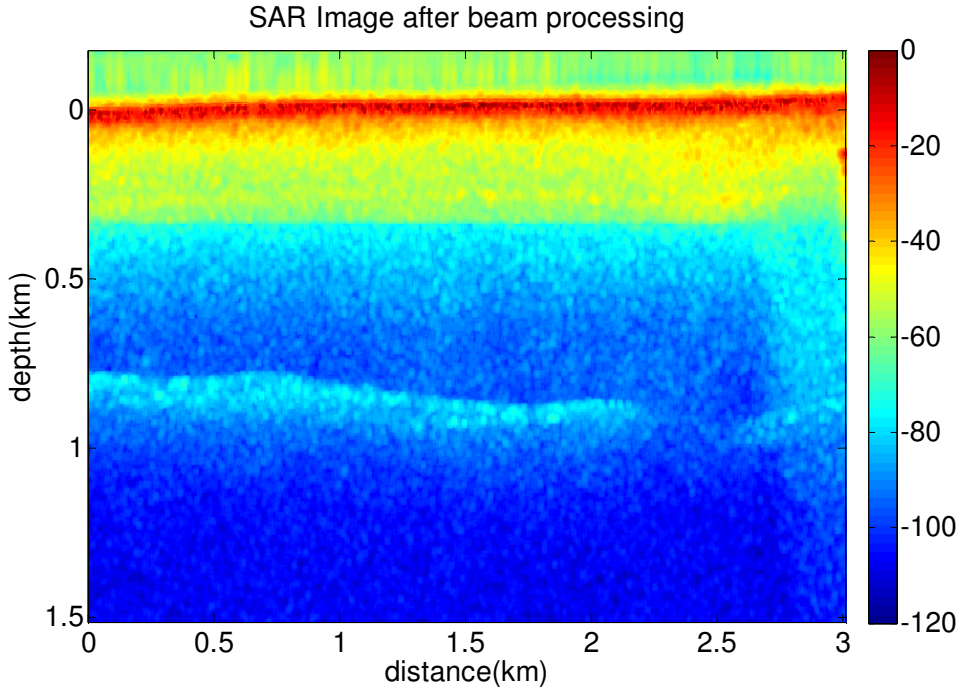

Figure 6.23: Clutter Reduction by Beam Subtraction

Figure 6.24 is a SAR image with ice clutter across Jakobshavn channel from a single element of MCRDS Twin Otter. The data were collected on May 27, 2006 when the aircraft was flying across the channel from south (−48°57.7',69°11.8') to north (−48°58.1',69°6.4') at an average height of 648 m. The file numbers are 170-174. A small part of the northern channel bank is barely visible at depth of about 700 m.

Figure 6.25 shows the receive beam patterns of MCRDS Twin Otter used in the clutter power estimation algorithm. Unlike in the MCRDS P-3 case, the beam pattern of Hanning weighting in green only reduces at most by 10 dB compared to

uniform weighting in blue for clutter at DOA larger than 60 degrees. Similar to the MCRDS P-3 case, the clutter beam pattern in red-dash line is obtained by setting the look direction at 60 degrees and putting two nulls at -2 and 2 degrees in equations (6.9)~(6.12).

Figure 6.26 shows the image of the main beam from combining the five channel data with the Hanning weighting. The channel's north bank becomes clear because the clutter around it is reduced by about 20 dB as shown by the A-scopes in Figure 6.28. The ice surface multiple masked by ice clutter becomes clear and the south bank at the depth of about 1.3 km on the left of the SAR image is also brought up as the result of clutter reduction. Figure 6.27 shows the image after applying the clutter-power estimation algorithm. On average the incoherent beam subtraction reduces clutter further by 7.2dB in this case. This improvement is visible by comparing the image portions deeper than 1.5 km in Figures 6.26 and 6.27 and is also shown by the A-scope differences between green and red ones the in Figure 6.28. However, the channel bed is still not visible because of the huge in-channel ice attenuation.

Figure 6.29 is a SAR image across Jakobshavn channel near Jakobshavn calving front from a single element of MCRDS P-3. The data were collected on September 21, 2007 when the aircraft was flying across the channel from north $(-49^{\circ}13.0', 69^{\circ}10.1')$ to south $(-49^{\circ}13.4', 69^{\circ}4.1')$ at an average height of 835m. The

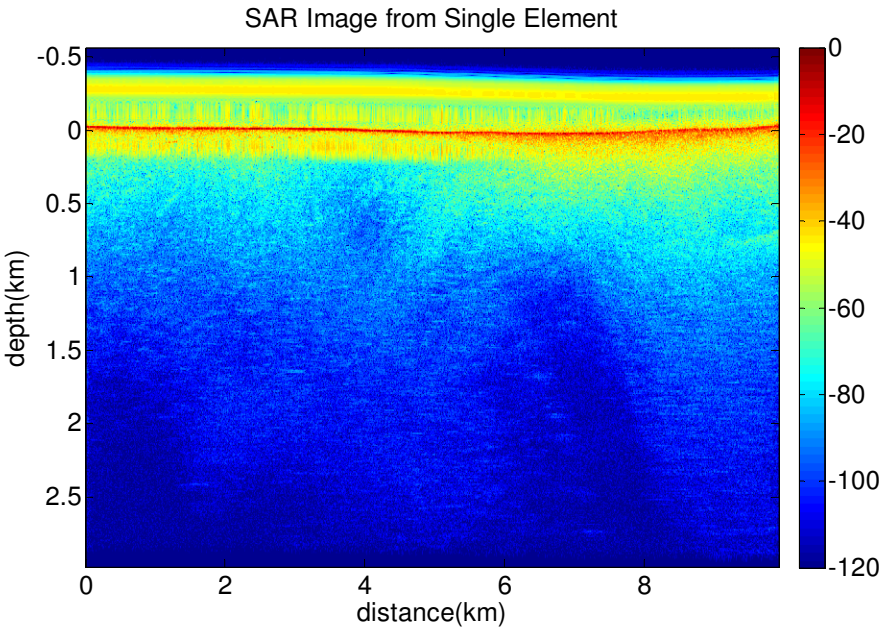

Figure 6.24: SAR Image across Jakobshavn Channel with Ice Clutter

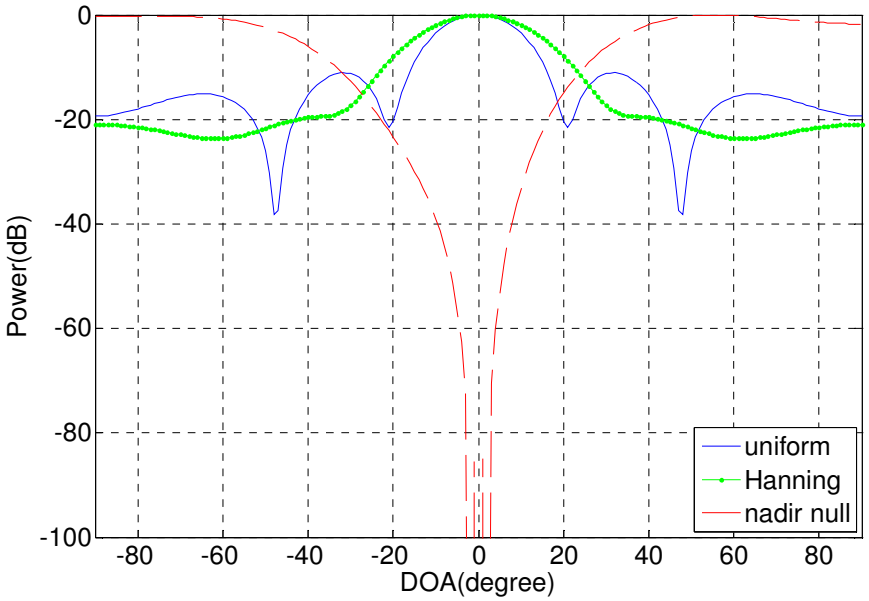

Figure 6.25: Receive Beam Patterns of MCRDS Twin Otter

Used in Clutter Power Estimation Algorithm

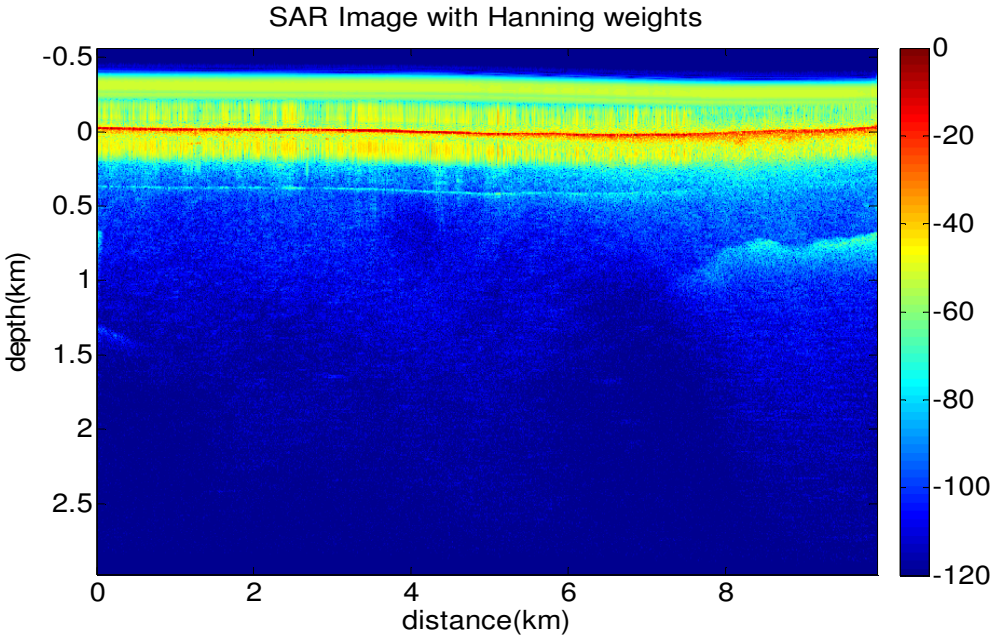

Figure 6.26: Image of Main Beam across Jakobshavn Channel

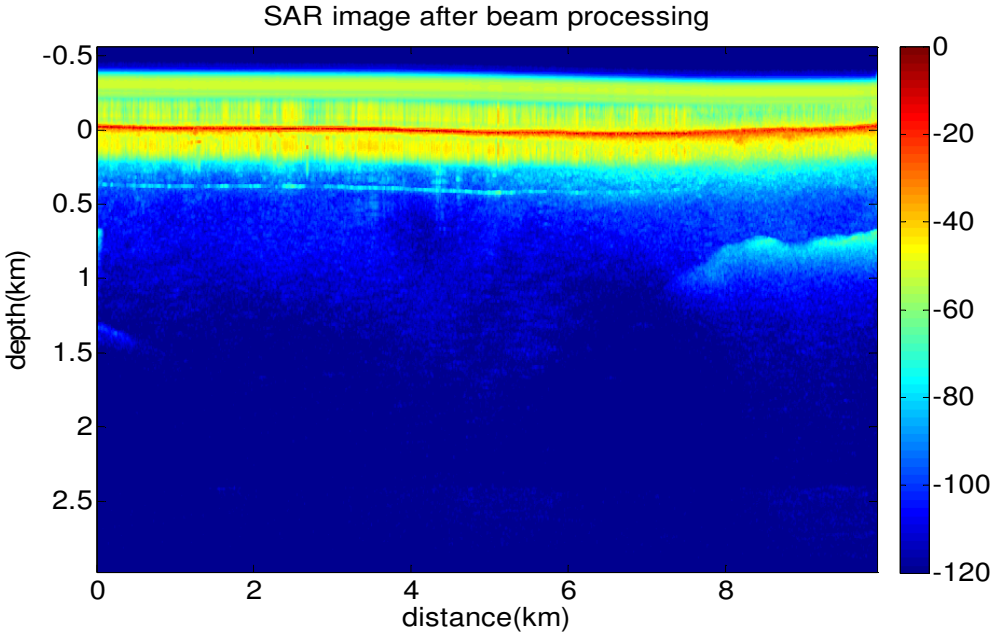

Figure 6.27: Clutter Reduction across Jakobshavn Channel by Beam Subtraction

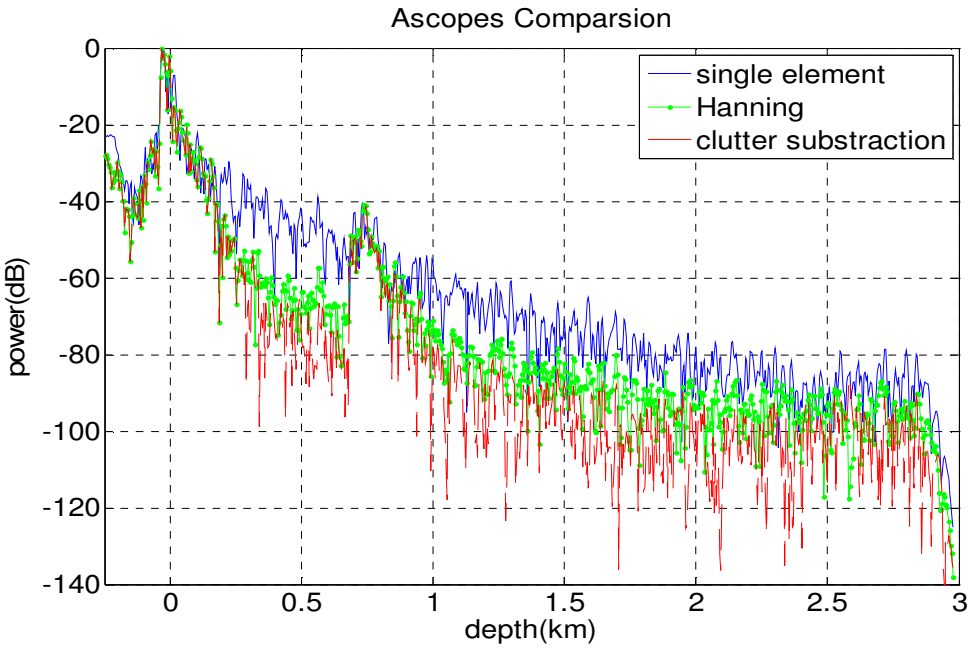

Figure 6.28: A-scope Illustration of Clutter Reduction by Beam Subtraction

file numbers are 125-129. The ice bed in the channel is totally invisible and seems masked by across-track ice surface of uniformly distribution that is the case the clutter-power estimation algorithm effectively applies to. Figure 6.30 Figure shows the image of the main beam from combining the data of four channels with Hanning weighting. Figure 6.31 is the SAR image with nulls placed around nadir direction. Figure 6.32 is the image after beam subtraction according to the clutter-estimation algorithm. Figure 6.33 shows the A-scope comparison at the distance of 2.865m among the data from single element, Hanning weighting and the beam subtraction. It is observed that the A-scope from Hanning weighting is almost the same as the one of the single element. Although the A-scope of beam subtraction reduces power about 8.3dB on average, the trend keeps the same without change.

For across-track ice surface clutter at large angles, we usually can observe obvious clutter reduction by just uniform or Hanning weighting as shown in previous examples. However, in this case and other cases near Jakobshavn calving front, we have not observed obvious clutter reduction from any array processing, including uniform weighting, Hanning weighting, null-steering and MVDR algorithms. This raises a question: are the dominant signals over calving front that mask the ice bed really the ice surface clutter from across-track direction at large angles as we assumed? There might be two possibilities that result in the failure of any array processing. The first possibility is that the dominant signals are from across-track volume backscattering within the main beam of the receive array because of the increased water content in ice close to calving front. Since the ice surface is heavily crevassed and the topography is not flat at calving front, the second possibility is that the dominant clutter-like signals are from surface slope and multipath scatterings that are not accounted in SAR processing. Figure 6.34 is pasted from the posted SAR images on CReSIS website, and seems to support the argument with the very apparent correlation between the vertical clutter steaks and the ice variable surface topography.

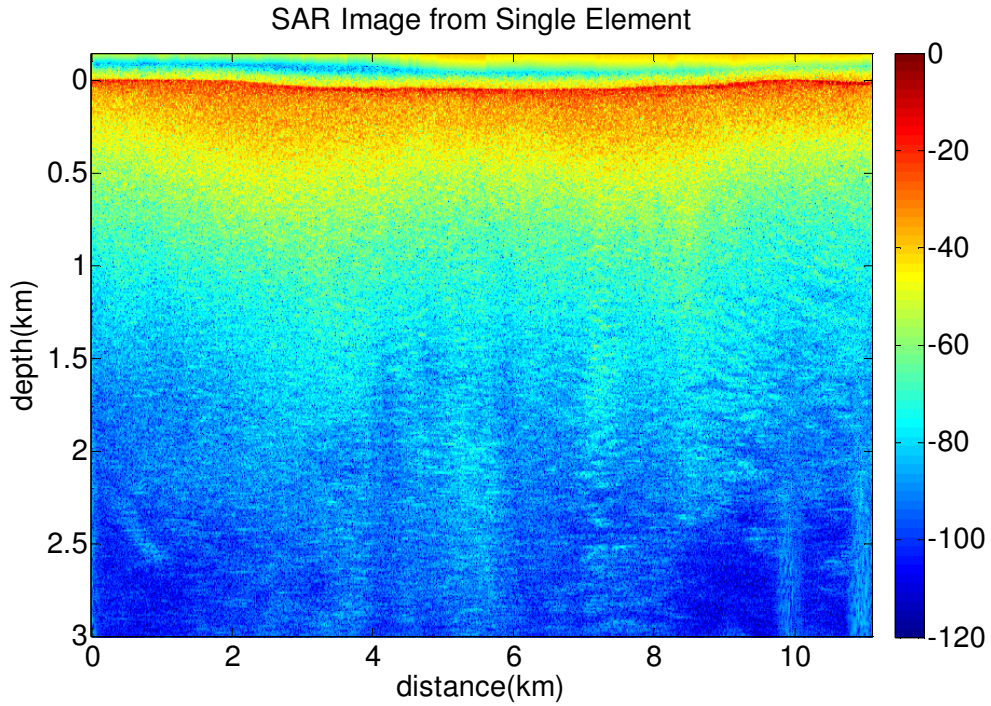

Figure 6.29: SAR Image near Jakobshavn Calving Front

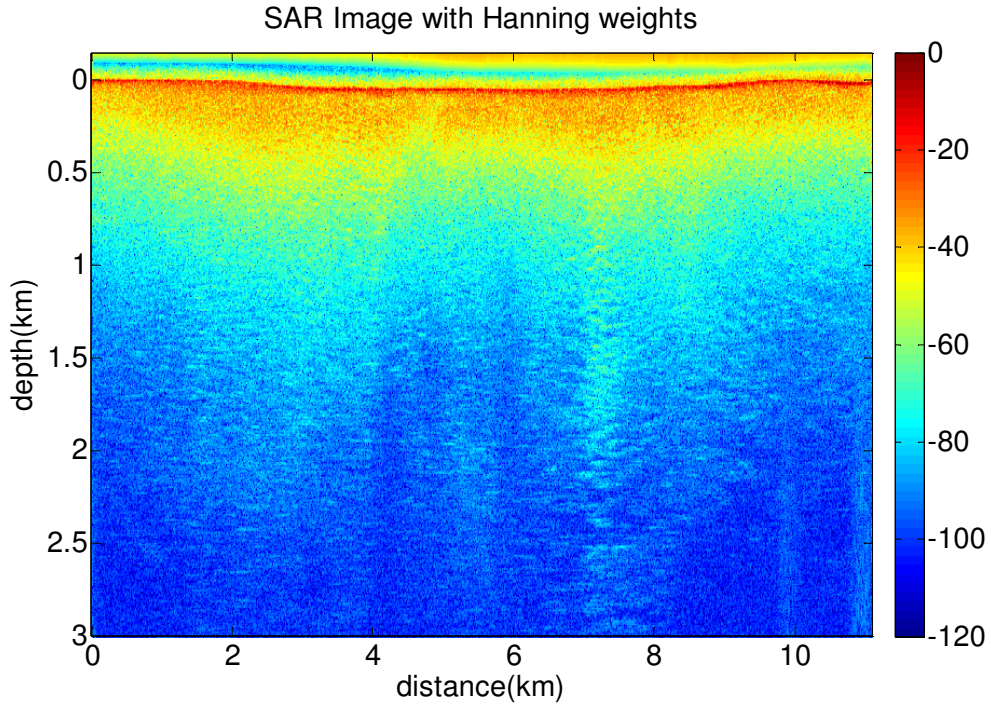

Figure 6.30: Image of Main Beam near Jakobshavn Calving Front

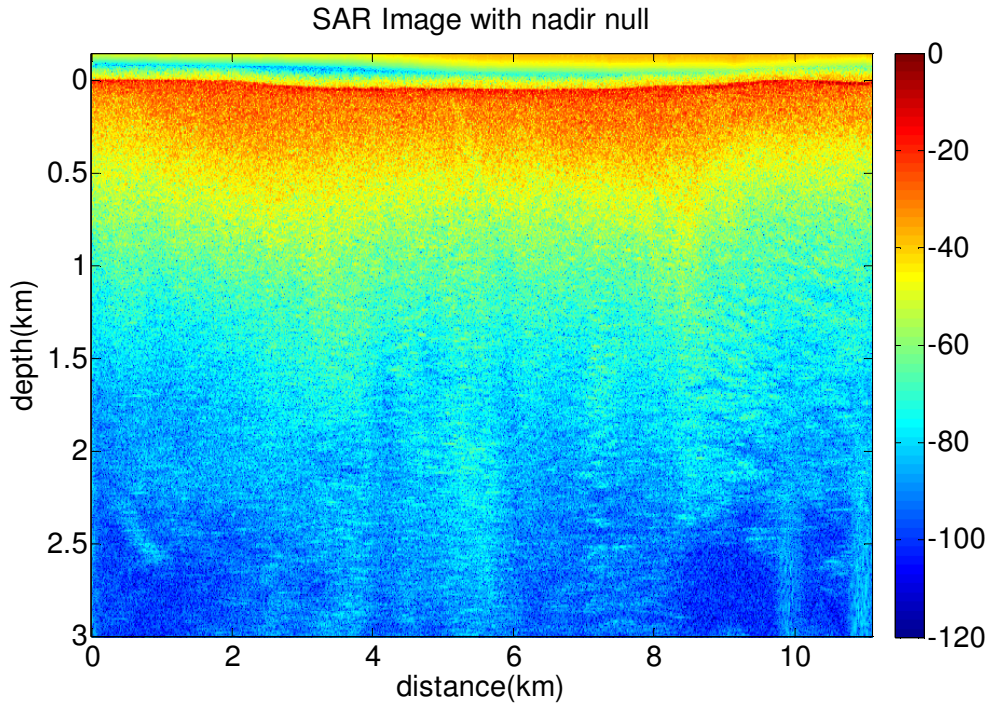

Figure 6.31: Image with Null at Nadir near Jakobshavn Calving Front

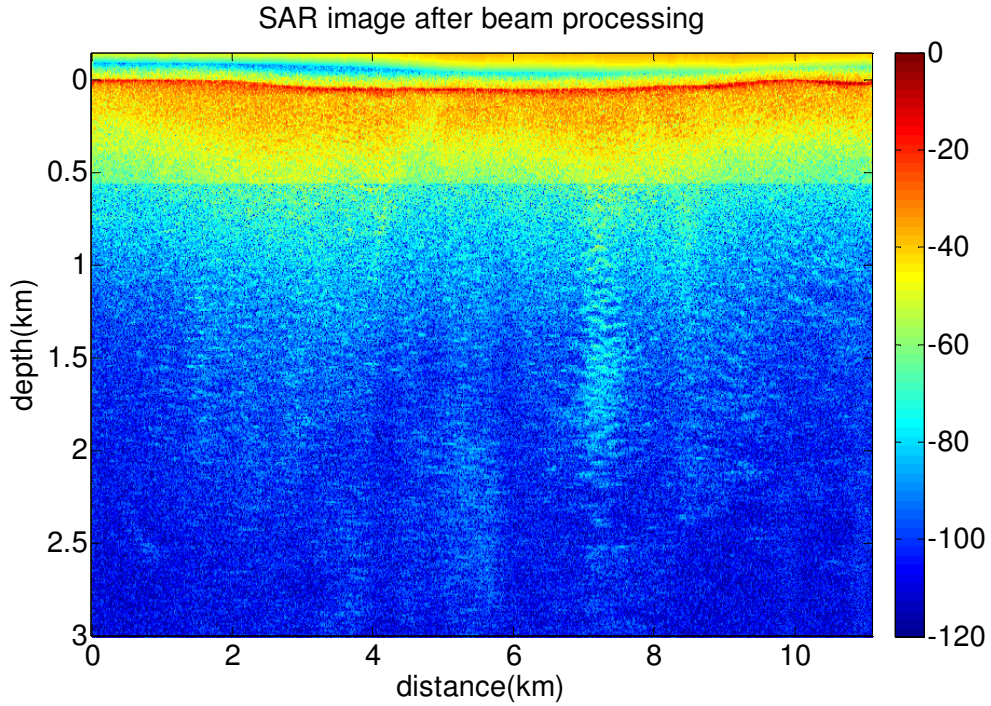

Figure 6.32: Image after Beam Subtraction near Jakobshavn Calving Front

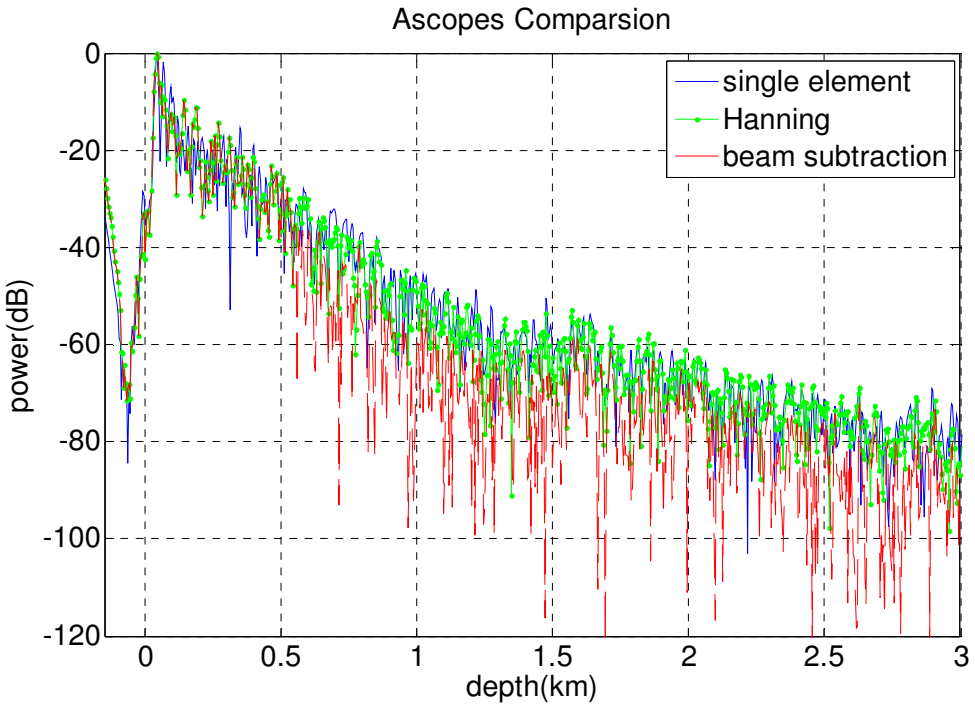

Figure 6.33: A-scope Comparison for Data near Jakobshavn Calving Front

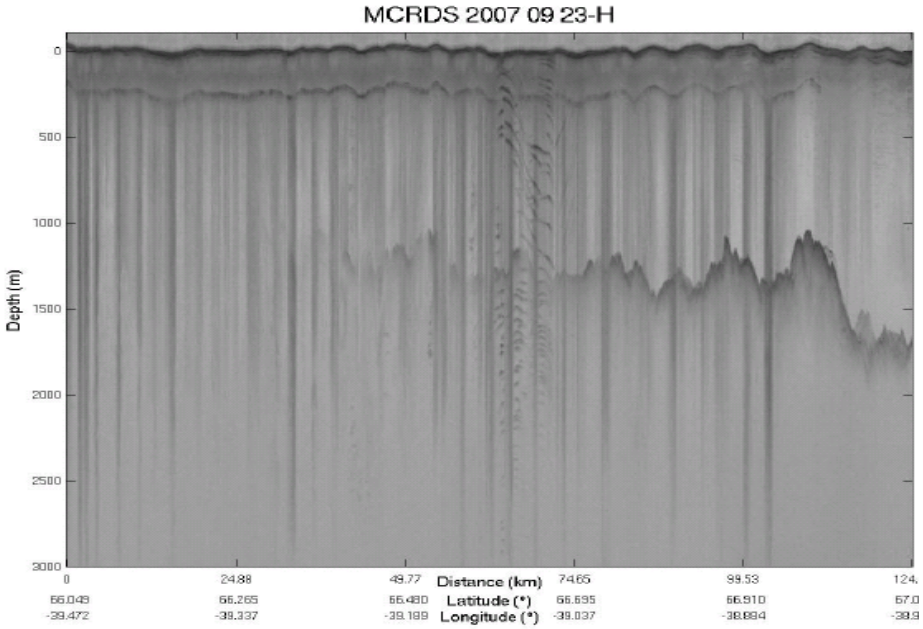

Figure 6.34: Correlation of Vertical Clutter Streaks with Surface Topography

Chapter 7: Summary and Recommendations

7.1 Summary

The MCRDS airborne radars are developed at CReSIS to map the ice-sheet bed, deep internal layers and sound fast-flowing outlet glaciers with its high sensitivity and array processing ability for clutter reduction. This dissertation covers the waveform design, the development and implementation of SAR and clutter reduction algorithms for MCRDS radars to achieve range low-sidelobes, improve SNR and reduce clutter.

The sidelobes of strong ice-bed echoes may mask or be misinterpreted as returns from deep layers. Based on a simulation with GRIP-ice model, a low sidelobe level of –60dB is required to reliably detect the weak echoes of deep layers that are close to the ice bed. Chapter 3 of this dissertation explores two kinds of low-sidelobe waveforms. The first waveform is tapered linear-chirp and the second one is complementary-coded waveforms. It is known for a linear-chirp signal that its rectangular-like spectrum results in high-level sidelobes in time or range domain. Mismatched filter with various window functions such as Hanning, Blackman and Dolph-Chebyshev is effective in reducing close sidelobes but cannot reduce the distant sidelobes to the required low level. The distant sidelobes are attributed to the Fresnel ripples in the linear chirp's spectrum. Since the sharp rise and fall of the chirp's envelope at the start and end result in the Fresnel ripples, properly tapering the

waveform edges will smooth the Fresnel ripples and reduce distant sidelobes. The achievable low level of sidelobe is also dependent on the chirp's time-bandwidth product. Dolph-Chebyshev window is chosen for mismatched filter as it has the minimum mainlobe width for a specified constant sidelobe level. The PSL and ISL as a function of different taper ratios are calculated for the 3-us (TB=60) and 10-us (TB=200) chirps used by MCRDS radars. The lowest PSL is -50 dB and -70 dB, respectively, for the tapered 3-us and 10-us chirp waveforms with optimal taper ratio. The sidelobe levels are first verified with laboratory measurements. The effects of the actual waveform amplitude and phase distortion on sidelobes are evaluated. The sidelobe levels are then verified with the real-survey data over Greenland in 2007 using high-SNR specular echoes from ocean surface, smooth ice surface and bottom. The lowest sidelobe level verified is about -64 dB. This is for the first time for ice-sounding radars to report such low sidelobes from real data. Theoretically complementary-coded waveforms cancel out all sidelobes. But unavoidable waveform amplitude and phase mismatches because of imperfectness of hardware will result in sidelobes. According to simulation the amplitude and phase mismatches between two complementary waveforms should not exceed 1% and 0.5° if -60-dB sidelobe level is needed. In laboratory measurements, sidelobe levels of -72.56 dB and -64.89 dB are achieved with two different high-precision waveform generators. 32-bit and 80-bit complementary-coded waveforms are designed respectively for the low-gain and high-gain modes of MCRDS radars. The sidelobe level is -50 dB according to laboratory measurements. The sidelobe level of the complementary

waveforms is verified to be -48 dB and -49dB with the real-survey data over Greenland in 2008 using high-SNR specular echoes from ocean surface, smooth ice surface and bottom. This is for the first time for ice-sounding radars using complementary waveforms.

Chapter 4 describes three data-preconditioning steps including reference function calibration, channel equalization and RFI reduction. Reference function calibration is employed to reduce waveform-distortion effects caused by the system for maximizing the gain from pulse compression. Well-calibrated reference function is needed and can be obtained from elaborate system loopback measurements in laboratory for each of transmit channels. The total SNR gain from previous reference function calibration for MCRDS Twin Otter is quantified using ice bed echoes at 1.5 km depth in Chapter 4, and turns out to be about 0.55dB and 1.10dB for its low and high gain modes. The gain may look trivial, but SNR improvement of even half dB is important in detecting very weak signals like the ones from the deepest ice bed in Jakobshavn glacier. Channel equalization is a necessary step for effective array processing and clutter reduction because most widely- used array theories assume identical channels. High-SNR echoes from ocean surface, smooth ice surface and bottom are used to estimate channel mismatches. Channel mismatches of MCRDS P-3 are found to be varying with a random component superimposed on constant values. Constant mismatches can relatively easily be compensated to obtain some SNR improvement of nadir signals in array processing. But the random mismatches make

it difficulty to perform accurate beamforming and null placement for clutter reduction. Monte Carlo simulation is carried out in Chapter 4 to evaluate the random amplitude and phase mismatch effects on null depth and location for MCRDS P-3's array configuration. It turns out 1% of random amplitude mismatch will result in 3° random variations in null locations around 70° and 9.5-dB random variations in null depth. Random phase mismatch of 1° will result in 6.2° random variations in null locations around 70° and 9.5-dB random variations in null depth. Part of the data collected by MCRDS P-3 in 2007 are severely degraded by RFI from laser altimeter and an Ethernet cable used to download data while the radar was in operation. Anechoic chamber measurements show the radar sensitivity is reduced by 15 dB by the RFI of the Ethernet cable. In Chapter 4, various methods for RFI suppression are reviewed and an implementation of MVDR algorithm in frequency domain originally used in acoustic application is employed and modified to reduce the RFI effects in the contaminated data collected by MCRDS P-3. This implementation first estimates the steering vector using strong echoes of ice surface or bottom. The optimal weights are then calculated with the steering vector and the array correlation matrix to combine array data to reduce the RFI by spatial filtering. Details of the implementation are described in Chapter 4. The RFI is suppressed by 12 dB in applying the algorithm to ice data. As a result, deep ice layers that are weak or invisible because of RFI are either enhanced or brought up.

MCRDS radars employ SAR processing to improve the SNR of ice layers and bottom, to refine the azimuth resolution and reduce the along-track ice surface clutter. In Chapter 3, a SAR algorithm based on wavefront reconstruction theory is implemented in frequency and wave-number domains. This algorithm takes advantages of FFT and is thus much faster than time domain methods. The refraction at the air-ice interface and any internal-ice layer interface is handled by using different wave propagation velocities across the interface. The synthetic aperture length is controlled by the beamwidth of K-filter that is actually an idealized antenna radiation pattern filter implemented in wave number domain. The aircraft motion causes defocusing and topographic deformations of ice surface, layer and bed. In Chapter 5, a narrow beamwidth motion compensation algorithm is derived and implemented in which the height variations of each antenna element from the aircraft's translational and rotational motion are computed using GPS and INS data. The motion compensation algorithm is verified with ice data in terms of the correction of topographic deformation and SNR improvement. The SAR algorithm is carefully verified with both simulation data and sea ice data in terms of SNR and azimuth resolution improvements as a function of aperture length. The data collected by MCRDS Twin Otter over Jakobshavn glacier in 2006 are processed with the SAR algorithm. Very weak echoes from the deepest parts of the channel are detected for the first time using large synthetic aperture length in radar soundings and the depths match with seismic measurements.

In addition to the big attenuation encountered in sounding fast-flowing outlet glaciers, across-track ice clutter is another challenge that is being addressed with great efforts at CReSIS. Chapter 6 first reviews basic beamforming theories of linear array and then explore three clutter reduction algorithms: 1) data-dependent MVDR algorithm, 2) data-independent null-steering algorithm and 3) clutter power estimation algorithm. Similar to RFI, ice clutter is actually another kind of interference. Therefore the FMV algorithm, the frequency-domain version of MVDR in Chapter 4 for RFI reduction is also used to reduce ice clutter. The data-independent null-steering algorithm first calculates the angle of ice surface clutter for each depth bin according to the geometry that the clutter signals take the same time as the ones from depth to arrive at the receivers. Optimal weights with nulls on both left and right at the calculated angle are then used to sum the array data to reduce clutter. When the first two algorithms apply to sea ice data, they reduce clutter signals from sea ice by 34.30 dB and 28.57 dB. The FMV outperforms the null-steering algorithm as it is optimal and adaptive using data statistics. In the case of sea ice, each piece of sea ice is close to a point target with high clutter-to-noise ratio and is used to calculate accurate DOA estimates of clutter signal and channel mismatches. For the FMV algorithm, the high-SNR specular echoes from ocean surface also provide a very good means to calculate the steering vector. Most important, since the clutter power concentrates in few specific directions, the FMV algorithm is able to place deep nulls accordingly to reduce the clutter effectively. For the null-steering algorithm, the accurate DOA and channel equalization assure the nulls' placement precision and

depth in the sea ice clutter case. But both the FMV and null-steering algorithm are not very effective when applied on survey data with distributed ice clutter. In the distributed ice clutter scenario, the FMV algorithm is not effective because it cannot place deep nulls in many directions simultaneously to reduce the distributed power. And the null-steering algorithm is limited in the distributed ice clutter scenario because no good source is available to estimate the channel mismatches that degrade the null's placement precision and depth greatly. If the clutter is from volume scattering, no improvement is possible with both algorithms. Unlike the first two algorithms that are element-spaced, the clutter-power estimation algorithm is a beam-spaced method. It is more robust to channel mismatches and errors in the estimate of clutter angle and also applies to volume clutter. There are two stages of the beam-spaced method. The first stage is in element space to form a main beam and a clutter beam. The main beam is formed by choosing weights to enhance the nadir signals and with clutter signals partly reduced. The clutter beam is formed by choosing weights to put a null at nadir and to have maximum gains in the direction of clutter. The second stage is to subtract the weighted clutter beam from the main beam to properly compensate the gain difference between the two beams based on power profiles estimation. Two clutter scenarios are used to illustrate the effectiveness of the beam-spaced algorithm. In the first scenario, the aircraft's altitude is high at 1386 m and the clutter-masked depth is deep around 2 km, while in the second case the aircraft's altitude is low at 550 m and the clutter-masked depth is shallow around 800m. In both scenarios the beam-spaced algorithm reduces clutter further beyond the reduction by

Hanning weighting. The further clutter reduction is around 10.3 dB in the first case and 9.6 dB in the second one. Two examples are given for reducing the ice clutter over Jakobshavn channel with the beam-spaced method. In the first example, the algorithm is able to reduce the ice clutter across the channel by 7.2 dB over the clutter reduction by Hanning weights. But the channel bed is still not visible after the clutter reduction because of the huge ice attenuation in the channel. The second example is the ice clutter near Jakobshavn calving front. The beam-spaced method seems not working. Actually any array processing methods we have tried all fail in this case. Therefore we should put in more efforts to understand what these clutter-like dominating signals are and where they come from.

7.2 Recommendations

Based on the work of this dissertation, stated below are some conclusions and recommendations:

(1) The linear-tapered chirp waveforms prove to have achieved very low sidelobe levels and make it possible to detect the weak echoes from deep ice layers close to the bed. The sidelobe performance of complementary-coded waveforms is more sensitive to and limited by system distortions. Because of the $0-\pi$ phase shifting, complementary coded waveforms have much wider spectrum and tend to interfere with other systems. It was reported that other systems on board were interfered when MCRDS-P3 was using complementary-coded waveforms to collect

data. The SAR images of complementary-coded waveforms are not as clear as the ones of the linear chirp waveforms because of the RFI interference from other systems. Therefore, complementary-coded waveforms are not a good option for MCRDS radars.

(2) The implemented SAR algorithm in f-k domain with narrow-beam motion compensation performs very well in most data collection scenarios. In the case of outlet glacial like Jakobshavn channel, a very long synthetic aperture is desired to enhance the much-attenuated nadir echoes while the aircraft has to follow the wandering and up-and-down topography. A time domain SAR algorithm like back projection algorithm needs to be implemented with three-dimensional widebeam motion compensation and slope compensation. Time-domain methods are more flexible to incorporate these compensations.

(3) Ice basal SAR images with bed scattering characteristics can be generated from the data collected by MCRDS radars with SAR processing and beamforming. Figure 7.1 is an example of such images of the ice bed near the south of Thule in Greenland. The data were collected by MCRDS-P3 on September 17, 2007. The images are generated by combining the four nadir-looking SAR images of its four channels with two sets of optimal weights. One set of weights forms a beam looking at 30 degrees to the left and suppressing the right signals. The other one forms a beam looking at 30 degrees to the right and suppressing the left signals. The top and bottom

images in Figure 7.1 respectively cover a left and right area of about 11.5 km (along track) by 0.6 km (across track). Some basal areas with strong back scatterings are identified in both the left and right images.

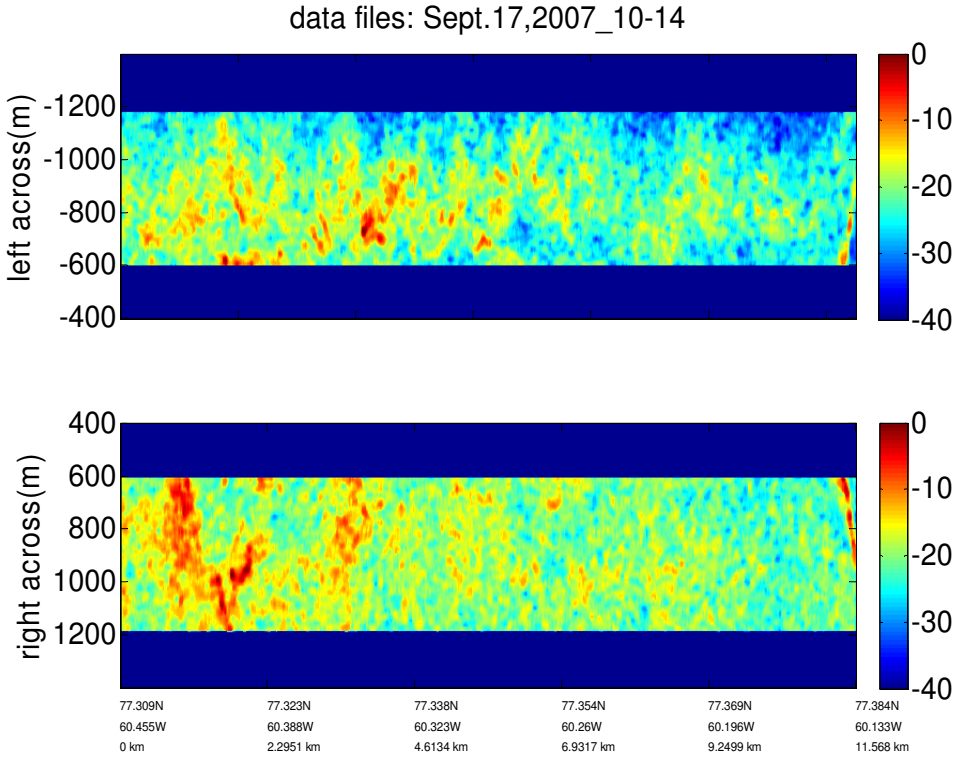

Figure 7.1: Ice Basal SAR Images by Beamforming

(4) The random variations in magnitude and phase of channel mismatch are the main limiting factor for various clutter-reduction algorithms. The mutual coupling, scattering effects of aircraft wing and fuselage and wing flexure combine to result in the variations. The mutual coupling and the aircraft wing and fuselage scattering effects can be modeled by 3D full-wave electromagnetic field simulation using design tools like HFSS. For this purpose, the existing array models of MCRDS radars used

in HFSS simulation needs to include the realistic geometry of the wing and fuselage. Optimal weights taking into these effects can be calculated for beamforming based on the results from reliable HFSS simulations. To resolve the problem of wing flexure, acceleration sensors need to be installed on each element of the antenna array to measure their movements. The knowledge of position variations of each array elements is necessary in both SAR and beamforming processing to obtain the best gain.

(5) The beam-based clutter power estimation algorithm works best for the clutter scenario when the clutter power profile as a function of depth does not change much along track because the algorithm estimate the profile by averaging the ones of multiple snapshots of the clutter beam. A moving averaging window may be included in the algorithm to make it adaptive to the profile changes along track. On the other hand, the algorithm does not make use of the phase information of the main beam and clutter beam. Adaptive and optimal beam-based algorithms with phase information that exist in literature worth further exploration for ice clutter reduction. For example, if we replace $|y_1|$, $|y_2|$ and $|y|$ in Figure 6.4 with y_1, y_2 and y, the structure is called post-beam former interference canceller (PIC) in [85], and the optimal weights to minimize the mean output power for PIC are calculated by

$$w = \frac{\mathbf{v}^H R\mathbf{u}}{\mathbf{u}^H R\mathbf{u}} \tag{7.1}$$

The mean output power is

$$P(w) = \mathbf{v}^H R\mathbf{v} - \mathbf{u}^H R\mathbf{v}\mathbf{v}^H R\mathbf{u} / \mathbf{u}^H R\mathbf{u} \tag{7.2}$$

And the performance of PIC is well studied with conventional main beamformer and different interference beamformer in the literature.

References

[1] Alley, R.B. and Bernstsen, T., etc., 2007. Summary for Policymakers, Contribution of Working Group I to the Fourth Assessment Report of the Intergovernmental Panel on Climate Change.

[2] Rignot, E. and Kanagaratnam, P., Changes in the Velocity and Structure of the Greenland Ice Sheet, Science, 17 February 2006, Vol. 311, No. 5763, pp. 986-990.

[3] Massom, R. ad Lubin, D., Polar Remote Sensing, Volume II, Ice Sheets, Praxis Publishing Ltd, 2006, pp. 16-21.

[4] Paterson, W. S. B., The Physics of Glaciers, 3rd Edition, Butterworth-Heinemann, pp. 318-321.

[5] Dahl-Jensen, D., Dating of the NEEM Site Based on the Ariborne Cresis Radio Echo Sounding Data from 17 Sept. 2007, Niels Bohr Institute, University of Copenhagen, Denmark.

[6] Chuah, T.S., Design and Development of a Coherent Radar Depth Sounder for Measurement of Greenland Ice Sheet Thickness, RSL Technical Report 10470-5, January 1997.

[7] Chiing, A.W.Y., Design and Development of an Airborne Stretch Radar for Depth Sounding the Jakobshavn Outlet Glacier, M.S. Thesis, Electrical Engineering and Computer Science, The University of Kansas, 1998.

[8] Wong, K. W., Development of a Prototype of a 2-8GHz FMCW Radar for Snow Thickness Measurement on Sea Ice, M.S. Thesis, Electrical Engineering and

Computer Science, The University of Kansas, 1999.

[9] Kanagaratnam, P., Airborne Radar for High Resolution Mapping of Internal Layers in Glacial Ice to Estimate Accumulation Rate, Ph.D. Dissertation, Electrical Engineering and Computer Science, The University of Kansas, 2002.

[10] Paden, J., Bistatic/Monostatic Synthetic Aperture Radar for Ice Sheet Measurements, M.S. Thesis, Electrical Engineering and Computer Science, The University of Kansas, 2003.

[11] Dunson, D. R., A Wideband Synthetic Aperture Radar for Ice Sheet Basal Measurements, M.S. Thesis, Electrical Engineering and Computer Science, The University of Kansas, 2005.

[12] Paden, J., Synthetic Aperture Radar for Imaging the Basal Conditions of the Polar Ice Sheets, Dissertation, Electrical Engineering and Computer Science, The University of Kansas, 2006.

[13] Lohoefener, A., Design and Development of a Multi-Channel Radar Depth Sounder, M.S. Thesis, Electrical Engineering and Computer Science, The University of Kansas, 2006.

[14] Rodrigues-Morales, F. etc, Dual-Frequency and Multi-Receiver Radars for Sounding and Imaging Ice Sheets, paper submitted to EuSAR, Center for Remote Sensing of Ice Sheets, University of Kansas, 2007.

[15] Marathe, K. C., Dual-Band Multi-Channel Airborne Radar for Mapping the Internal and Basal Layers of Polar Ice Sheets, M.S. Thesis, Electrical Engineering and Computer Science, The University of Kansas, 2008.

[16] Tammana, D., Design of Waveform Generator for Coherent Radar Depth Sounder, M.S. Thesis, Electrical Engineering and Computer Science, The University of Kansas, 2001.

[17] Paden, J. D., MCRDS Radar Configuration for GISMO, Dec.5, 2006

[18] Atkins, T., Design and Development of an Improved Data Acquisition System for the Coherent Depth Sounder, M.S. Thesis, Electrical Engineering and Computer Science, The University of Kansas, 1999.

[19] Jara, V. A., Antenna Report: Glaciers and Ice Sheets Mapping Orbiter(GISMO), CReSIS, The University of Kansas, Aug. 10,2006

[20] Cook, C.E., Siebert, W.M., The Early History of Pulse Compression Radar, IEEE, Transactions on Aerospace and Electronic Systems, Vol. AES-24, No. 6, Nov. 1988, pp825-833.

[21] Skolnik, M. I., Introduction to Radar Systems, Tata McGraw-Hill, 3rd Edition, pp339-369, 2001

[22] Schmidt, G., Rüdiger, R., Czechowsky, P., Complementary Code and Digital Filtering for Detection of Weak VHF Radar Signals from the Mesosphere, IEEE Transactions on Geoscience Electronics, Vol. GE-17, No. 4, October 1979

[23] Nowicki, A., Secomski, W., Litiewski, J. and Trots, I., On the Application of Signal Compression Using Golay's Codes Sequences in Ultrasounding Diagnostic, Archives of Acoustics, Vol. 28, No. 4, 2003, pp. 313-324

[24] Misaridis, T. and Jensen, J., Use of Modulated Excitaton Signals in Ultrasound, Part I: Basic Concepts and Expected Benefits, IEEE Trans. On Ultrasonics, Ferroelectrics, and Frequency Control,Vol. XX, No.Y, Month 2002.

[25] Collins, T. and Atkins, P., Nonlinear Frequency Modulation Chirps for Active Sonar, Radar, Sonar and Navigation, IEE Proceedings, Vol. 146, No. 6, 1999, pp.312-316.

[26] Nathanson, F. E., Radar Design Principles, McGraw-Hill, Inc., 1990.

[27] Costas, J. P., A Study of a Class of Detection Waveforms Having Nearly Ideal Range-Doppler Ambiguity Properties, Proc. IEEE 72, Aug. 1984, pp. 996-1009

[28] Frank, F. L., Polyphase Codes with Good Nonperiodic Correlation Properties, IEEE Trans., IT-9, Jan. 1963, pp. 43-45.

[29] Welti, G. R., Quaternary Codes for Pulse Radar, IRE Trans. IT-7, June 1960, pp. 400-408.

[30] Siraswamy, R., Multiphase Complementary Codes, IEEE Trans. Inform. Thry., IT-24(5), 1978, pp.546-548.

[31] Levanon, N. and Mozeson, Eli, Radar Signals, Jonn Wiley & Sons, Inc., 2004

[32] Misaridis, T. and Jensen, J., Use of Modulated Excitation signals in Medical Ultrasound, Part II: Design and Performance for Medical Imaging Applications, IEEE Trans. On Ultrasonics, Ferroelectrics, and Frequency Control, Vol. 52, No. 2, Feb. 2005

[33] Cook, C. E. and Bernfeld, M., Radar Signals, Artech House,1993

[34] Rodriguez-Morales, F., GISMO Calibration, CReSIS Technical Report, University of Kansas, August 07, 2007

[35] Golay, M. J. E., Complementary Series, I.R.E. Transactions on Information Theory, 1961, pp. 82-87.

[36] Popovic, B.M., Efficient Golay Correlator, Electronics Letters, 19th August 1999, Vol.35 No.17

[37] Bonato, M. J., A Comparison of Two Computational Technologies for Digital Pulse Compression, High Performance Embedded Computing Conference, 2002, MIT Lincoln Laboratory, Sept. 24, 2002

[38] Li, J., Simulation and Experimentation of Complementary-coded Pulse Radar for Ice Measurement, M.S. Thesis, Electrical Engineering and Computer Science, The University of Kansas, 2006.

[39] Analogic Data Precision, "Users Manual Model 2045 Polynomial Waveform Synthesizer", Analogic Corporation, "Users Manual DBS 2050 VXI Waveform Generator"

[40] Analogic Corporation, "Users Manual DBS 2050 VXI Waveform Generator".

[41] Skolnik, M. I., Introduction to Radar Systems, Tata McGraw-Hill, 3rd Edition, pp276-284, 2001

[42] Guerci, J. R., Space-time Adaptive Processing for Radar, Artech House, 2003

[43] Theodore Koutsoudis, Louis Lovas, RF Interfrence Suppression in Ultra Wideband Radar Receivers, SPIE Vol. 2487, pp107-118.

[44] Miller, T., Potter L., and McCorkle, J. W., RFI suppression for ultra wideband radar, IEEE Transactions on Aerospace and Electronic Systems, 33(4):1142--1156, 1997.

[45] Lord, R. T., Aspects of Stepped-Frequency Processing for Low-Frequency SAR Systems, PhD thesis, University of Cape Town, Rondebosch, South Africa, 2000.

[46] Le, C. TC, Hensley, S., and Chapin, E., Adaptive Filtering of RFI in Wideband SAR Signals, JPL.
http://trs-new.jpl.nasa.gov/dspace/bitstream/2014/18952/1/98-0083.pdf

[47] Luo, X., Ulander, L. M. H., Askne, J., Smith, G., and Frölind, P., RFI Suppression in Ultra-Wideband SAR Systems Using LMS Filters in Frequency Domain, Electronics Letters, 37(4):241-243, February 2001.

[48] Reigber, P. A., and Papathanassiou, K. P., A Phase Preserving Method for RF Interference Suppression in P-band, Geoscience and Remote Sensing Symposium, *1999.*

[49] Goris, M., Joseph, A., Hampson G. and Smits F., Adaptive Beamforming System for Radio-Frequency Interference Rejection, IEE Proc.-Radar, SonarNavig., Vol.146, No.2, April 1999.

[50] Lord, R. T., and Inggs, M. R., Approaches to RF interference suppression for VHF/UHF synthetic aperture radar, Proceedings of the 1998 South African Symposium on Communication and Signal Processing, pp 95--100, 1998.

[51] Braunstein, M., Ralston, J. M, and Sparrow, D. A., Signal processing approaches to radio frequency interference (RFI) suppression, SPIE vol. 2230, pages 190-208, 1994.

[52] Buckreuss, S., Filtering Interferences from P-band SAR Data, Proc. European Conference on Synthetic Aperture Radar,EUSAR'98, Friedrichshafen, Germany, pp. 279-282, May 1998

[53] Abend, K. and McCorkle, J. W., Radio and TV interference extraction for ultrawideband radar, SPIE, Vol. 2487, pp. 119--129, 1995.

[54] Glover, J.R., Jr., Adaptive Noise Cancelling Applied to Sinusoidal Interferences, IEEE Transactions on Acoustics, Speech, and Signal Processing, vol. ASSP-25, No. 6, pp 484-491, December 1977.

[55] Li, J. and Stoica, P., Adaptive Filtering Approach to Spectral Estimation and SAR Imaging, SPIE, vol. 2487 , pp 153-164, 1995.

[56] Manolakis, D.G., Ingle, V. K., and Kogon, S. M., Statistical and Adaptive Signal Processing, Artech House, 2005

[57] Lockwood, M. E., Jones, D. L., Bilger, R. C., Lansing, C. R., O'Brien, W. D., Jr., Wheeler B. C., and Feng, A. S., Performance of Time and Frequency-domain Binaural Beamformers Based on Recorded Signals from Real Rooms, Journal of Acoustical Society of America, 115(1), January 2004.

[58] Lasswell, S. W., History of SAR at Lockheed Martin, Proceedings of the SPIE, Vol. 5788, 2005, pp. 1-12.

[59] Fahnestock, M., Bindschadler, R., Kwok, R. and Jezek, K., Greenland Ice Sheet Surface Properties and Ice Dynamics from ERS-1 SAR Imagery, Science, Vol. 262, No. 5139, pp. 1530-1534, Dec. 3, 1993

[60] Joughin, I. R., Fahnestock, M. A., Bamber, J. L., Annals of Glaciology, Vol. 31, No. 1, Jan. 2000, pp. 141-146(6)

[61] Legarsky, J. J., Gogineni, S. P. and Akins, T. L., Focused Synthetic Aperture Radar Processing of Ice-Sounder Data Collected Over the Greenland Ice Sheet, IEEE Transactions on Geoscience and Remote Sensing, Vol. 39, No. 10, Oct. 2001

[62] Leuschen C., Gogineni S. P. and Tammana D., SAR Processing of Radar Echo Sounder Data, Geoscience and Remote Sensing Symposim, 2000. Proceedings IGARSS 2000. IEEE 2000 International.

[63] Paden J. D., Allen C. T., Gogineni S. P. and Jezek. K.C., Dahl_Jensen D. and Larsen L. B., Wideband Measurements of Ice Sheet Attenuation and Basal Scattering, IEEE Geoscience and Remote Sensing Letters, Vol. 2, No. 2, April 2005

[64] van der Veen C. J., Leftwich T., von Frese R., Csatho B. M. and Li. J (2007), Subglacial topography and geothermal heat flux: Potential interactions with drainage of the Greenland ice sheet, Geophys. Res. Lett., 34, L12501, doi:10.1029/2007GL030046

[65] Joughin, I. R., Fahnestock, M. A., MackAyeal, D., Bamber, J. L. and Gogineni, S. P., Observation and Analysis of Ice Flow in the Largest Greenland Ice Stream, Journal of Geophysical Research, Vol. 106, No. D24, pp. 33021-34034, Dec. 27, 2001

[66] Cumming I.G., and Wong F. H., Digital Processing of Synthetic Apeture Radar Data, Algorithms and Implementation, Artech House, 2005

[67] Soumekh M., Synthetic Aperture Radar signal Processing with MATLAB Algorithms, John Wiley & Sons, Inc.

[68] Yilmaz, Ö., Seismic Data Processing, Investigations in Geophysics, Society of Exploration Geophysicists, vol. 2, pp.507-518, 1987

[69] Etkin, B., Dynamics of Atmospheric Flight, John Wiley & Sons Inc., 1972

[70] Li, J., SAR Simulation of Ice-depth Sounding Radar, EECS 825 final project report, Department of Computer Science and Electrical Engineering, University of Kansas, Dec. 16, 2006

[71] Li, J., SAR Algorithm Verification, Technical Document, CReSIS, University of Kansas, January, 2008

[72] Legarsky J. J., Synthetic-Aperture Radar (SAR) Processing of Glacier-ice-depth-Sounding Data, Ka-Band Backscattering Measurements and Applications, Dissertation, Department of Computer Science and Electrical Engineering, University of Kansas, 1999.

[73] Clarke K. and Echelmeyer T., Journal of Glaciology, Vol. 43, 1996,

pp. 219-232.

[74] Paden J. et al., Transactions in Geoscience and Remote Sensing Letters, Vol. 2, No. 2, 2005, pp.164-168.

[75] Iken A., Echelmeyer K., Harrison W. and Funk M., Journal of Glaciology, Vol. 39, No. 131,1993, pp.15-25.

[76] Funk M., Echelmeyer K. and Iken A., Journal of Glaciology, Vol. 40, No. 136, 1994, pp. 569-585.

[77] Lüthi M., Funk M., Iken A., Gogineni S., and Truffer M., Jouranl of Glaciology, Vol 48, No.162, 2002, pp. 369-385.

[78] Holt J.W., Blankenship D.D., Morse D.L., Peters M.E. and Kempf S.D., Surface Clutter Removal in Airborne Radar Sounding Data from the Dry Valleys, Antarctica, Workshop on Radar Investigations, 2005.

[79] Scheiber R. and Prats P., Surface Clutter Suppression for Ice Sounding Radars by Coherent Combination of Repeat-pass Data, Geoscience and Remote Sensing Symposium, 2007, IGARSS 2007. IEEE International Volume, Issue, 23-28 July 2007, pp. 3559-3562.

[80] Rodriguez E., Freeeman E., Jezek A., K. and Wu X., A New Technique for Interferometric Sounding of Ice Sheets, EUSAR Proceedings, Dresden, Germany, 2006

[81] http://www.faqs.org/patents/app/20080284640

[82] Veeramachaneni C., Development of a Clutter Cancellation Algorithm for Data Collected Over Fast Flowing Outlet Glaciers, Thesis, Department of Electrical Engineering and Computer Science, University of Kansas, April, 2007

[83] Balanis C. A., Antenna Theory: Analysis and Design, Third Edition, John Wiley & Sons, Inc., 2005, pp283-296

[84] Manolakis D. G., Ingle V.K. and Kogon S. M., Statistical and Adaptive Signal Processing: Spectral Estimation, Signal Modeling, Adaptive Filtering and Array Processing, Artech House, Inc., 2005, pp. 630

[85] Godara L. C., Smart Antennas, CRC Press 2004, pp.18-33

[86] Brookner E., Howell J. M., Adaptive-adaptive Array Processing, IEEE Proc., Vol.74, 1986, pp. 602-604

[87] Gabriel W. F., Using Spectral Estimation Techniques in Adaptive Processing Antenna Systems, IEEE Trans. Antennas Propagation, Vol. 34, 1986, pp. 291-300.

[88] Godara L. C., A Robust Adaptive Array Processor, IEEE Trans., Circuits Syst., Vol. 34, 1987, pp. 721-730.